DEMOCRITUS UNIVERSITY OF THRACE

FACULTY OF ENGINEERING

DEPARTMENT OF ELECTRICAL AND COMPUTER ENGINEERING

Diploma thesis

Fabrication and characterization of ultra-high level radiation sensors with thin-film nanolayers

Viktoria Meskova

Supervisors   Federico Ravotti & Ourania Sidiropoulou
EP-DT Department
CERN

Supervisor   Dr. Jean-Michel Sallese
Department of Microsystems and Microelectronics
EPFL

Supervisor   Dr. Filippos Farmakis
Department of Electrical and Computer Engineering
Democritus University of Thrace

March 2021

Abstract

In high energy physics experiments it is a common practice to expose detectors, electronic components and systems to particle beams, in order to assess their level of radiation tolerance and reliability. One of the facilities used for such tests is the Proton Irradiation Facility (IRRAD) which is located at the CERN accelerator complex.

In order to properly control the 24 GeV/c proton beam and guarantee reliable results during the irradiation tests in IRRAD, Beam Profile Monitor (BPM) devices are used. The current BPMs are manufactured according to standard PCB technology featuring a matrix of copper sensing pads. When exposed to the beam, secondary electrons are emitted from each pad generating a charge proportional to the particle flux. The charge is measured individually for each pad using a dedicated readout system, and thus the shape, the position and the intensity of the beam are obtained.

This thesis presents the study carried out for the improvement of BPM devices and the development of a new fabrication technique, based on microfabrication. The new prototypes that were manufactured have more efficient structure with better sensing material, substrate and design. More specifically, they are one order of magnitude thinner (less invasive), they present higher sensitivity due to the usage of aluminum as sensing material which has, intrinsically, higher secondary electron yield than copper and they have enhanced radiation tolerance.

The performance of the new BPMs was tested with 200 MeV electron beam in the CLEAR facility at CERN, to validate their functionality and to investigate their usability in lower energy electron beams (MeV) for general-purpose applications (e.g, industry, medicine).

Key words: Beam-line instrumentation, secondary electron emission (SEE), radiation-hard detectors, secondary electron yield (SEY), micro-fabrication, thin-films

Acknowledgement

The present research work was completed throughout my fascinating journey as a technical student at CERN. At this point, I would like to acknowledge the contribution of all the people that were part of it.

Firstly, I would like to express my sincere gratitude to my CERN supervisor Federico Ravotti for giving me the opportunity to work in the research field, for his constant guidance, the continuous encouragement and all of our enlightening discussions and shared enthusiasm. I would also like to thank my professors Filippos Farmakis and Jean-Michel Sallese for their shared knowledge and their interest during this research. I would like to offer my special thanks to my cleanroom advisor Didier Bouvet for helping me to overcome the obstacles in the fabrication process and sharing his expertise.

Many thanks to IRRAD-team (Ina, Giuseppe, Isidre) for their warm welcoming, personal and professional assistance and the pleasant working atmosphere. A big thanks goes to my cleanroom-buddy, Rania, whose contribution in the BPM upgrade was more than essential. I am gratefully indebted for her very valuable comments on this thesis. Finally, I must express my very profound gratitude to my family, my dearest friends in Greece and my new friends at CERN for their constant support.

Contents

Thesis overview

The aim of the research work undertaken in the context of this thesis was to optimize the Beam Profile Monitors (BPMs) that are used in the proton irradiation facility (IRRAD) at CERN, by investigating alternative fabrication techniques and materials.

Chapter 1 introduces CERN and its accelerators. The proton irradiation facility (IRRAD) and the CERN CLEAR electron facility are presented. CLEAR is the place where the BPMs were tested.

Chapter 2 gives a description of the existing beam diagnostic instruments used for measuring the intensity and the transverse profile of the particle beams. The focus is laid on the instruments that are used in the IRRAD. A detail description of the old PCB-based BPMs used in the IRRAD, is also given.

Chapter 3 gives the theoretical background of the BPM devices. Secondary electron emission (SEE), which is the operating principle of the detectors, is examined in detail.

Chapter 4 refers to the first BPMs based on microfabrication technology. These prototypes were fabricated on Si-SiO$_2$ substrate for the proof of concept. The chosen layout, fabrication steps and experimental runs are presented.

Chapter 5 presents new BPM prototypes with substrate grounding and extra oxide layer on the top of the device, that were fabricated and tested.

Chapter 6 describes a new approach of the BPM devices on Kapton® substrate. The characterization and performance of these devices are also discussed.

Chapter 7 brings together the main results obtained in this thesis, summarizing the principal conclusions and reveals potential opportunities for improvement and future work. A series of appendices contain complementary information related to the detectors.

Introduction

In this chapter, after a short introduction to the CERN accelerating complex, the proton IRRADiation facility, where the Beam Profile Monitors (BPMs) are installed, is described in detail. Subsequently, the CLEAR electron facility, where the characterization of the new BPMs was performed, is presented.

1.1 About CERN

The European Organization for Nuclear Research (CERN) was founded in 1954 and is located at the French-Swiss borders close to Geneva. It operates the largest high energy physics (HEP) laboratory in the world and it's main function is to provide the particle accelerators and other infrastructure needed for particle physics research. Fig. 1.1 shows the CERN accelerator complex. It is a succession of linear and circular accelerators that increase the energy of the particles gradually before being injected into the next accelerator in the chain.
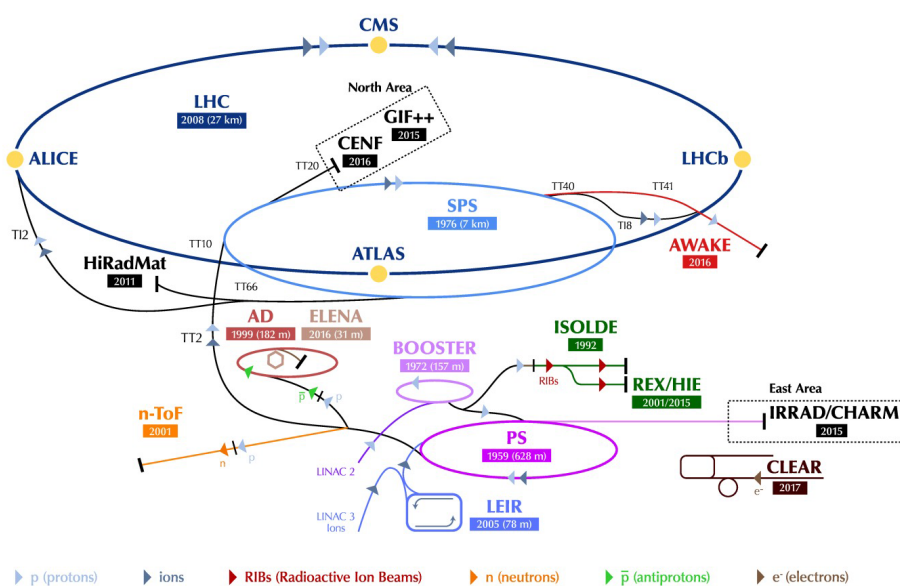
Fig. 1.1.: The CERN accelerator complex with the four LHC experiments (ALICE, ATLAS, CMS and LHCb) and other small and medium experiments and facilities.

The last ring in this chain is the largest and most powerful accelerator in the world, the Large Hadron Collider (LHC) [1]. It is located underground in a tunnel that has a circumference of 27 km and a maximum depth of 175 m. The LHC machine accelerates and collides protons as well as heavy ions. After acceleration to their peak

energy, the particles are brought into collisions in the four intersection points where the particle detectors (ALICE [2], ATLAS [3], CMS [4], LHCb[5]) are located.

The proton source is a bottle of hydrogen gas and an electric field is used to strip hydrogen atoms to yield protons. Linac 2, the first accelerator in the chain, accelerates the protons up to the energy of 50 MeV. The beam is then injected into the Proton Synchrotron Booster (PSB), which accelerates the particles up to 1.4 GeV, followed by the Proton Synchrotron (PS), which pushes the beam up to 25 GeV. Protons are then sent to the Super Proton Synchrotron (SPS) and accelerated up to 450 GeV. Finally, they are transferred to the two beam pipes of the LHC. In one beam pipe the particles are circulated clockwise while in the other one anticlockwise. After acceleration they reach the maximum energy of 7 TeV [6].

Heavy ions start from a source of vaporized lead. The acceleration process starts in Linac 3 and continues in the Low Energy Ion Ring (LEIR). After LEIR they are injected into the PS and follow the same path as the protons. Heavy ions are accelerated up to their maximum energy of 5 TeV. Linear accelerator 4 (Linac 4) is designed to boost negative hydrogen ions to high energies. It is scheduled to become the source of proton beams for the LHC after the LS2.

1.2 IRRAD proton facility

The Proton Synchrotron (PS) other than serving as a pre-accelerator for the Large Hadron Collider (LHC), it hosts also a dedicated experimental area, the so-called East Area. In this area, four beam lines are shared among target experiments, radiation facilities and test beam lines. Only in one of these lines (T8), the primary beam from the PS is delivered into the irradiation facilities. The other three beam lines (T9, T10, T11) are called secondary as the primary proton beam from PS hits a target and generates secondary particles with a much lower energy.

The proton IRRADiation facility is located in the East Area, on the T8 beam-line, as shown in Fig. 1.2. Its operation aims to provide a place for studying the effects of radiation on detectors, structural materials[1] and readout electronics. The beam arrives into the IRRAD in bunches[2] of protons (spills) with a maximum intensity of 5×10^{11} protons/spill every 10 sec in average and with a duration of about 400 ms. Different focusing options are possible on the T8 beam-line in order to provide variable Gaussian beam dimensions ranging from about 5×5 mm^2 to 20×20 mm^2, according to the user's requirements [7].

There are three irradiation zones along the path of the beam, as shown in Fig. 1.3, each one with a determinate usage. In the **first zone**, low atomic number materials

---

[1]Metals, polymers, organic materials, composites

[2]Each proton beam in the accelerator complex is not a continuous string of particles but, in LHC for example, it consists of bunches of about a hundred billion of protons.
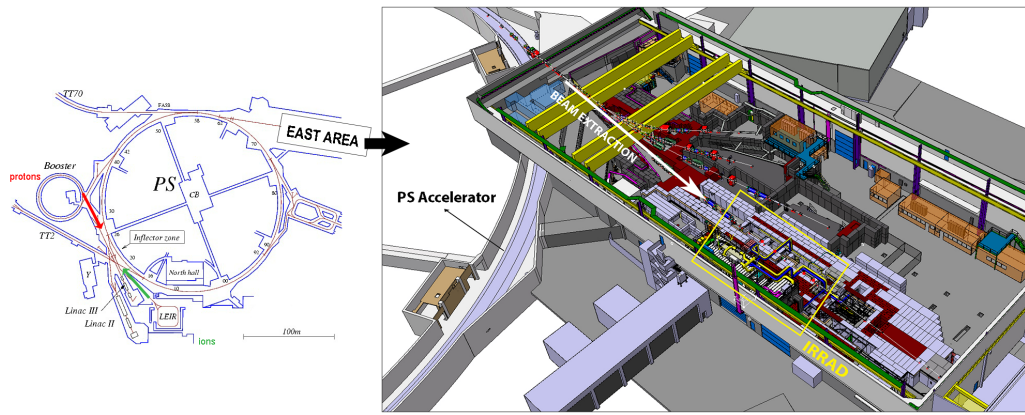
Fig. 1.2.: The PS complex where the location of the East Area is indicated (left). Overview of the East Area (right). The white arrow indicates the direction of the beam and the yellow rectangular the location of the IRRAD facility.

such as thin silicon devices are tested. The **second zone** is dedicated for the irradiation of electronic devices under power and the **last zone** is used for samples with a higher atomic number such as dense calorimetry materials and it is the location where big objects are irradiated since the beam can cover a 20×20 mm^2 surface. The whole irradiation area has been designed with a reinforced shielding, 4.5k tons of cast iron and 11.5k tons of concrete, in order to protect the operators and the users from the radiation induced by the beam.
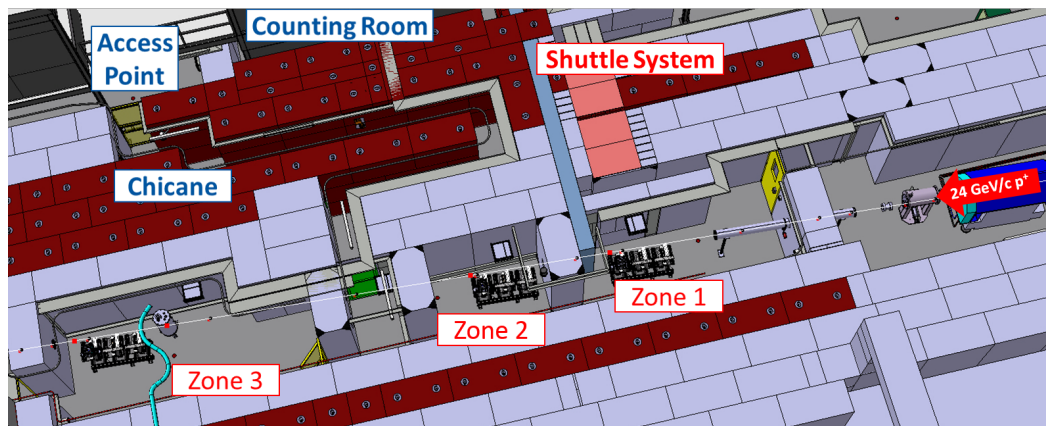
Fig. 1.3.: The three irradiation zones of IRRAD proton facility.

During operation, the access in the IRRAD facility is forbidden because of the ionizing radiation risks. For this reason, in each zone there are tables, where the samples under test are placed, that can be remotely controlled (Fig. 1.4). The tables can move upwards or downwards with respect to the beam transverse plane, with a precision of ±0.1 mm. The rotation angle has an accuracy of $\pm0.025°$. They can automatically move the samples during irradiation in order to provide a uniform beam spot over layer surfaces up to more than 10×10 mm^2. A maximum of three

tables per zone (nine in the whole facility) can be operated in parallel, which allows the irradiation of several materials at the same time.
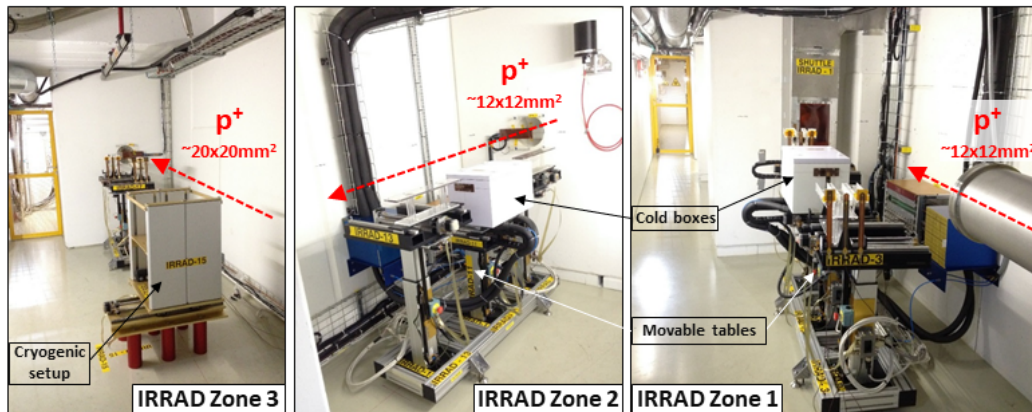
Fig. 1.4.: Irradiation tables installed in the IRRAD proton facility.

In addition to that, in the IRRAD there is also a remote controlled conveyor (IRRAD1 Shuttle) travelling on a rail system that facilitates the radiation of small and passive samples with maximum dimensions of 5×5 mm^2, without the need of human access into the area and thus of stopping the beam (Fig. 1.5). Furthermore, irradiation experiments at low temperature (-25°C) or in cryogenic conditions (1.9 K) can be performed at the IRRAD. For this reason, the area is equipped with cold boxes and a cryogenic system, as shown in Fig. 1.4 [7].

Fig. 1.5.: IRRAD1 Shuttle. Samples holder (left) and loading station (right).

1.3 CLEAR electron facility

CLEAR[1] is an experimental electron facility at CERN which focuses on R&D and component studies, for existing and future accelerator applications [8]. This facility was used for the characterization of BPMs because the IRRAD was not operational in 2019 - 2020 due to the Long Shutdown 2 (LS2[2]). More in particular, the VESPER and the THz test-stands were used. An overview of the CLEAR facility in shown in Fig. 1.6.
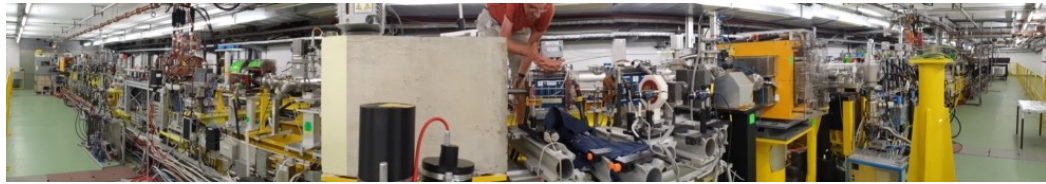
Fig. 1.6.: Overview of the CLEAR electron facility.

VESPER[3] provides a broad electron beam of 10×10 mm^2 and charge that vary from about 1 pC to 1.5 nC. The beam energy is depending on how many accelerating structures are used in the beam-line, varied from 60 MeV to 220 MeV. It is monitored at the test position with a fluorescent YAG-screen[4]. The beam consists of pulses delivered at a frequency ranging from 0.8 Hz to 6 Hz and of bunches which are delivered at a frequency of 3 GHz. The pulse duration is a free parameter and can be chosen from 0 to 5 us, therefore the longest pulse of 5 us consists of 15000 pulses, which would contain about 4170 electrons.

(a) (b)
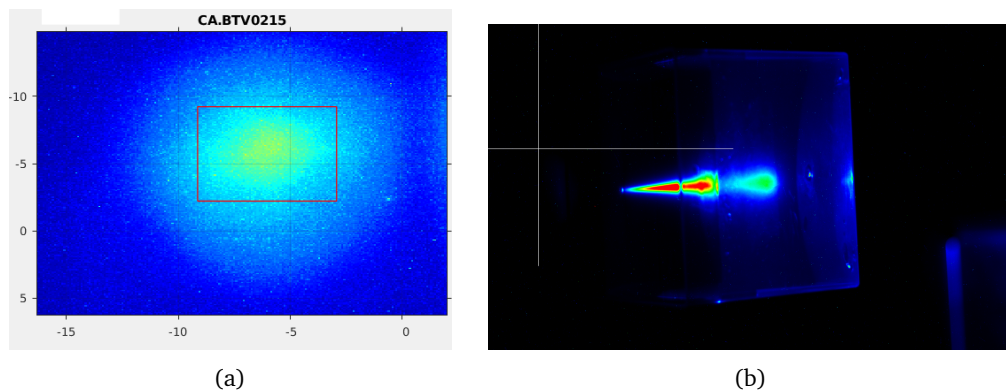
Fig. 1.7.: (a) Beam image on the YAG-screen in the THz. (b) Water tank for beam stabilization.

---

[1]Derives from CERN Linear Electron Accelerator for Research

[2]The period when the CERN accelerator complex shuts downs for planned maintenance and consolidation (2019- Sept. 2021).

[3]The name VESPER derives from the acronym Very energetic Electron facility for Space Planetary Exploration missions in harsh Radioactive environments for radiation testing.

[4]Fluorescent Screen (Cerium activated Yttrium Aluminum Garnet)

The THz[1] test-stand operates under the same parameters as the VESPER but with a focused electron beam of 1×1 mm^2 [9]. This setup provides strong focusing on the sample-under-radiation and minimize the dose on the nearby structures. Fig. 1.7(a) shows a beam image on the YAG-screen in the THz. To decrease beam scattering, a water tank is placed before the irradiating samples, as shown is Fig. 1.7(b). Table 1.1 summarize the main parameters of the IRRAD and the CLEAR (VESPER & THz) facilities.

Table 1.1.: Main parameters of the beam in the IRRAD and the CLEAR (VESPER & THz) facilities.

Facility	Particle Type	Energy	Intensity/ Activity	Beam Spot	Beam Details
IRRAD	p^+	23 GeV	10^{11} p/spill	20x20 mm^2	2-6 spills/min
VESPER	e^-	200 MeV	10^8 e$^-$/spill	10x10 mm^2	0.8 - 6 Hz
THz	e^-	200 MeV	10^8 e$^-$/spill	1x1 mm^2	0.8 - 10 Hz

---

[1]Tera Hertz source

Beam Monitoring Systems 2

Due to the variety of the existing beam transfer lines and accelerator machines, such as linacs, cyclotrons, synchrotrons and storage rings, the demands for beam monitoring systems can differ. Taking into account the broad spectrum of particles, such as electrons, protons and heavy ions, the development of versatile measurement techniques becomes essential. There is a large variety of parameters to be measured for characterizing particle beams such as intensity, transverse position, size and shape, emittance[1], polarization etc., with the precision required to tune, operate, and optimize the accelerators.

In this chapter, a general overview of beam instrumentation for intensity and transverse profile measurements is presented. The focus is laid on the working principles of the detectors that are used in the IRRAD facility, which are measuring these parameters. The operation concept and fabrication technology of the old IRRAD BPMs are also explained in detail in the last section.

2.1 Instrumentation for intensity and transverse profile measurements

Measuring the intensity and monitoring of the beam profile during the operation of any complex accelerator is of the paramount importance for its precise operation and the optimal exploitation of the beam when conducting experiments or irradiating electronic systems. Beam intensity is the number of charges that passes through a surface in a specific time unit in each bunch while the profile of the beam is determined by the density distribution of the particles in the two transverse coordinates [10]. Most of the diagnostic instruments which measure beam intensity and profile, are based on one of the following physics processes: emission of particles (electrons, photons, x-rays etc.) from matter, gas ionization, electrodynamics.

Table 2.1 summarizes the most common beam diagnostic instruments and their main characteristics that are used to measure the beam intensity and the profile of a particle beam. The first four devices are installed in the T8 beam-line, where the IRRAD facility is located. From these devices the Secondary Emission Chamber (SEC), the Beam Profile Monitor (BPM) and the Multi-Wire Proportional Chamber (MWPC) match the specific dynamic range of the IRRAD (10^9 to 10^{11} p/s) while

---

[1]Total beam flux emitted per unit area.

Table 2.1.: Beam diagnostic devices for intensity and profile.

Device	SEC[11]	Ionization Chamber (XION) [12]	IRRAD BPM[13]	MWPC[12]	SEM-grid[12]	OTR[10]	Synchrotron radiation[10]	Residual Fluorence Monitor[14]	Wire Scanner[10]	Scintilator screens [15]
principle	SEE	gas ionization	SEE	gas ionization	SEE	electro-dynamic process	electro-dynamic process	gas ionization	SEE	photoelectric effect
measurement	intensity	intensity	profile	profile	profile	profile	profile	profile	profile	profile
active material	Al	Ar/CO_2	Cu	Ar/CO_2	W-Re alloy	Al/Mylar	-	N_2	C	Al_2O_3
Min active material/	100 um	1 L	100 um	1 L	50-500 mm	0.25 um	-	1 L	10 um	50-1000 um
Resolution	-	-	4500 um	1500 um	500-5000 um	1 um	300 um	280 um/pixel [a]	1 um	250 um/pixel [a]
Dynamic range	10^{11}-10^{14}	10^4-10^9	10^9-10^{11}	10^4-10^9	10^5-10^{11}	10^9-10^{11}	10^5-10^6 [16]	10^{11}	10^5-10^6 [16]	10^6 [12]
Typical Operation [b]	T.L.	T.L.	T.L.	T.L.	T.L.	T.L.	C.A.	C.A.	C.A.	T.L.

[a] Depends on the CCD camera resolution
[b] Transfer Line (T.L.), Circular Accelerator (C.A.)

the Ionization Chamber (XION) was installed to enable the measurements of low intensity beams and thus cover a broader dynamic range, and to cross-calibrate these beam instruments with each other. Currently XION serves mostly for the lower intensity beams used downstream of IRRAD where CHARM facility[17] is located. The working principle of these four devices will be discussed in some more detail in the next section. A detailed description of the rest of the devices can be found in Appendix A.

Synchrotron radiation monitors, wire scanners and scintillation screens are not chosen for the T8 beam-line because of their limited dynamic range in operation. Detectors based on luminescent screens, such as Optical Transition Radiation (OTR) and Residual Fluorescence Monitors, were used in the IRRAD facility in the past, but have been replaced by the BPMs. This is because in a transfer beam-line like T8 the particles are not continuous thus, a profile measured by a luminescent screen is not persistent for more than few seconds every spill (a spill last ∼400 ms). Moreover, the screen cannot stay in the beam permanently because it greatly disturbs the particle beam and it degrades over time at the location where the beam hits. A SEM-grid can be, in principle, used in the IRRAD facility. However, this kind of detector is more complex to be produced and, in addition to that, the signal should be reconstructed in order to have a beam profile. Since a DAQ system for the current IRRAD BPM devices already exists, this kind of device is not considered as a replacement of the BPMs in the current study.

2.2 Beam instrumentation in the IRRAD facility

As discussed in the previous chapter, the IRRAD proton facility is located in the T8 extraction beam-line of the PS. The beam quality is the most important parameter for the operation of this facility. Fig. 2.1 shows the location of the beam instrumentation devices that are installed in the T8 beam-line with respect to the location of the IRRAD and the CHARM facilities.

There are four basic BPM detectors along the beam-line inside the IRRAD facility, two secondary emission chambers (SEC) one upstream and one downstream of the IRRAD, one ionisation chamber (XION) also downstream of IRRAD and a multi-wire proportional chamber (MWPC) downstream of the CHARM facility. The BPM devices are developed to meet the requirements of IRRAD by the team operating the facility (within the Experimental Physics department) while the operation of the rest of the devices are under the responsibility of the CERN Beam Instrumentation group (BE-BI).

The XION and SEC devices are used to measure the intensity of the beam while the BPMs and the MWPC are used to monitor the beam profile. The XION and the MWPC are both gaseous detectors based on the same working principle. When
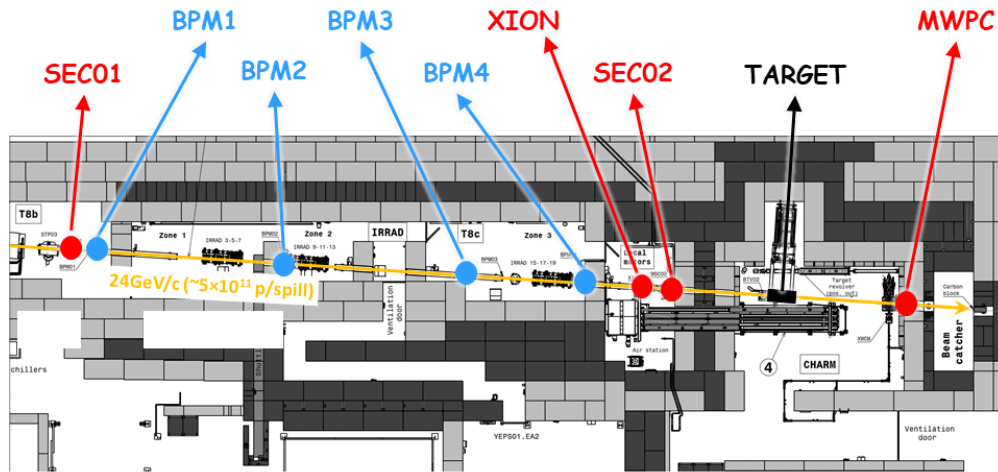
Fig. 2.1.: Beam diagnostics devices used in the T8 beam-line. The location of the IRRAD and CHARM facilities is also indicated. In blue are the devices that are developed and are operated by the IRRAD group while in red are the devices under the responsibility of the CERN Beam Instrumentation group.

charged particles pass through a few mm thick active gas volume, they ionize the gas creating electron-ion pairs. The separation of the electrons and ions is achieved by applying a potential difference in between the electrodes that surrounds the gas volume (Fig. 2.2(a)).

(a)	(b)
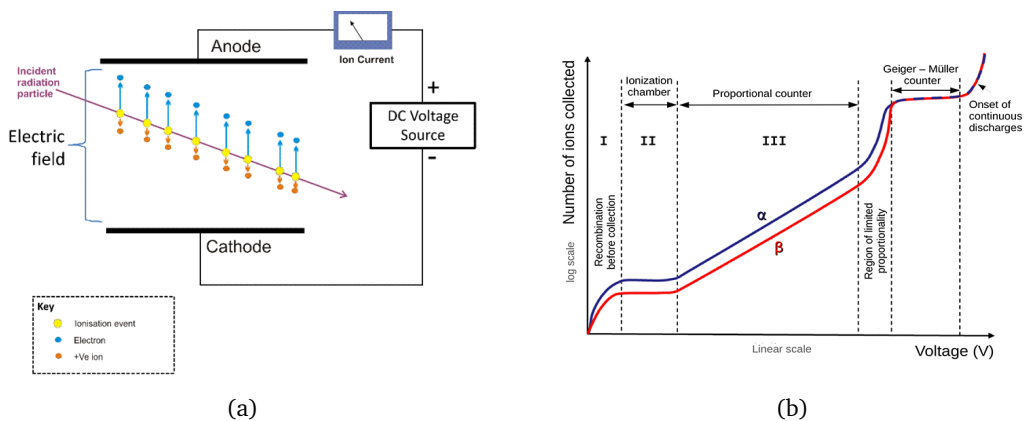
Fig. 2.2.: (a) Schematics of a parallel plate gaseous detector. The purple arrow indicates the charged particle that traverses the gas volume. The electrons (in blue) and the ions (in purple) that are created from the ionization process move towards the electrodes of opposite polarity when a potential difference is applied in between them. (b) Number of ions collected versus applied voltage in a single wire gas chamber.

Depending on the voltage that is applied, there are different amplification modes in the gaseous detectors. Fig. 2.2(b) shows an example of the number of ions (and electrons) collected as a function of the applied voltage in a single wire gas chamber. At zero voltage or very low electric field (region I), no charge is collected as the ion-electron pairs recombine under their own electrical attraction. As the current is increasing more and more ion-electron pairs are collected before recombination.

When all created ion-electron pairs are collected (region II) a further increase of the voltage does not show any effect. If the voltage is increased beyond region II then the electric field is strong enough to accelerate free electrons so that they will have enough energy to further ionize the gas molecules and multiply. This will result in an ionization avalanche or cascade. The detected charge is proportional to the originally deposited charge thus the name proportional counter. An increase in voltage beyond the region III will result in a large amount of ionization which creates space charges that distort the electric field close to the anode. This region is known as region of limited proportionality (region IV). Increasing the voltage above this region a chain reaction of avalanches (discharges) start to occur (regions V and VI) [18].

(a)   (b)
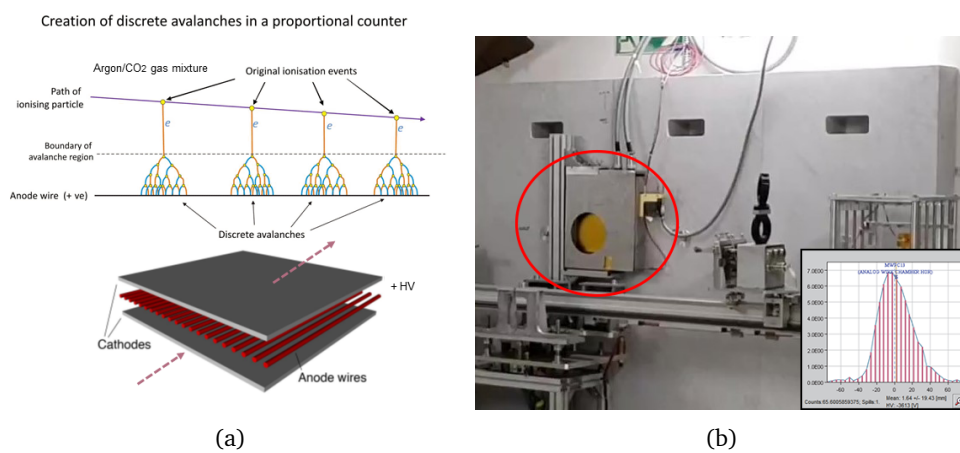
Fig. 2.3.: Multi-Wire Proportional Chamber (MWPC). a) Schematics and b) the device in its operation position the T8 beam-line. The insert shows an example of the measured transverse profile.

The XION detector is operated in the ionization mode while the MWPC in the proportional mode. Both devices are filled in with an inert gas, in most of the cases Ar is used, mixed sometimes with a few percentage of a molecular gas, like CH_4 or CO_2, that act as a quencher by absorbing the photons created by excitation of the Ar atoms.

The MWPC is a parallel plate gaseous detector consisting of two cathodes separated by a few mm and one anode in between them as shown in Fig. 2.3(a). The anode is a grid of wires with a couple of mm distance in between them operated at positive HV potential. The electrons liberated in the ionization process drift towards the positively charged wires following the electric field lines while the ions towards the cathodes. When the electrons approach the wires owing to the much stronger electric field they experience a strong acceleration. Having enough energy they further ionize the gas molecules and multiply. The distribution of the height of the signal over the wires represents the beam profile [19]. Fig. 2.3(b) shows the device

located in the beam line and the insert shows an example of the transverse profile measurement.
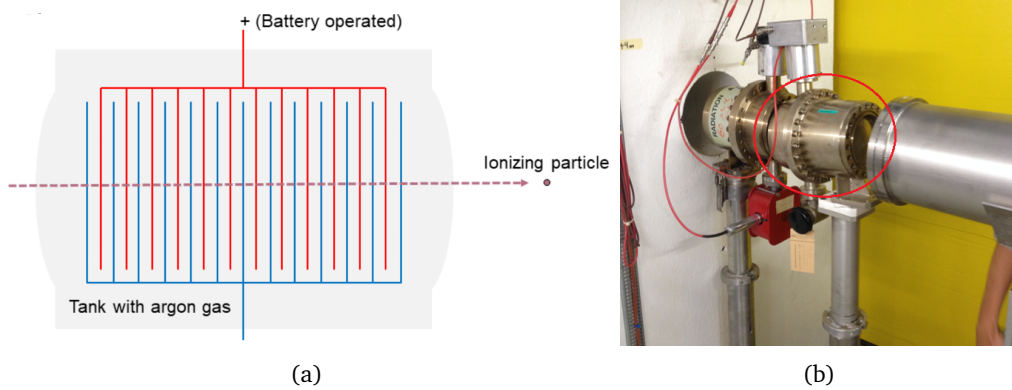
Fig. 2.4.: Ionization chamber (XION): (a) Schematics and (b) photo of the device XION of Fig. 2.1, in its operation position in the T8 beam-line.

The XION consists of two segmented electrodes as shown in Fig. 2.4(a). One of these electrodes is biased with a high voltage ($\sim$1 kV). The electrons liberated by the ionization process are collected by this electrode while the ions contribute to the charge measured on the other electrode by a sensitive current amplifier (not shown in this Fig. 2.4(a)). Like that, the intensity of the bunches can be measured which is in the range of 10^4 to 10^9 p/s. Fig. 2.4(b) shows the XION device as it is installed in the T8 beam-line.
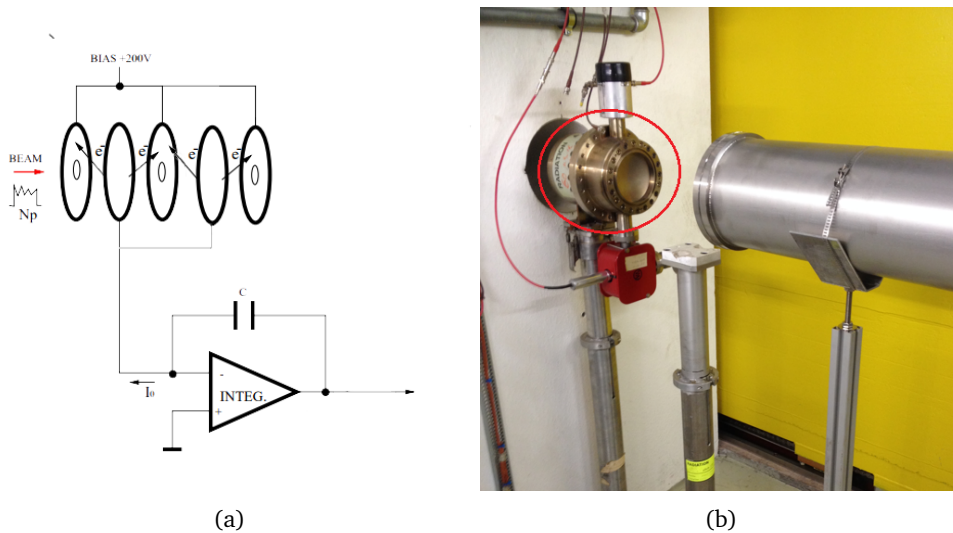
Fig. 2.5.: Secondary Emission Chamber (SEC): (a) Schematics and (b) photo of the device SEC02 of Fig. 2.1, in its operational position in the T8 beam-line.

The SEC and the BPM are devices based on the Secondary Electron Emission (SEE). The SEC consists of several thin aluminum foils with a few um thickness each, placed parallel to each other with some mm distance in between them (Fig. 2.5(a)) and is operated under high vacuum [11]. Alternating foils are biased with $\sim$200 V to

sweep out the free electrons and they are called collectors, while the other foils are connected to a sensitive current amplifier and they are called emitters. When the beam passes through the emitters, secondary electrons are produced and extracted. The signal that is generated in this case is proportional to the amount of extracted electrons. Like that, the intensity of the bunches can be measured which is in the range of 10^{11} to 10^{14} p/s. Fig. 2.5(b) shows the SEC device as it is installed in the T8 beam-line. The BPM device is described in details in the following section.

2.3 Beam Profile Monitor devices based on the PCB technology

One of the devices used in the IRRAD proton facility is the Beam Profile Monitor (BPM) [13]. As the SEC, its operation is based on the particle-induced Secondary Electron Emission (SEE) from metallic surface (see Chapter 3). The BPM consists of a rectangular-shaped, flexible printed circuit board (PCB), patterned with a matrix of metallic sensing pads on one end and a multi-pin connector on the opposite one. PCB traces connect electrically the sensing pads to the connecting pads. There are three different kinds of BPM consisting of diverse patterns and dimensions. Each one serves the alignment of the primary proton beam, which is ranging from $5{\times}5$ mm^2 to $20{\times}20$ mm^2, in particular way.

The basic BPM detector, the so-called fixed-BPM, consists of a matrix of 39 sensing pads (copper pads of $4{\times}4$ mm^2 and a pitch of 0.5 mm) covering a total area of $36{\times}27$ mm^2 on the beam transverse plane. It is used by the CERN Control Center (CCC) [20] to tune and steer the beam shape along the T8 beam-line. Fig. 2.7(a) shows a sample of the fabricated devices and how it looks like when it is installed in the facility during operation. There are four in total fixed-BPM detectors along the IRRAD facility, are shown in Fig. 2.6 (see Fig. 2.1 to locate them in the IRRAD facility). The BPMs are adjusted on the supporting plastic frame with Kapton® tape.
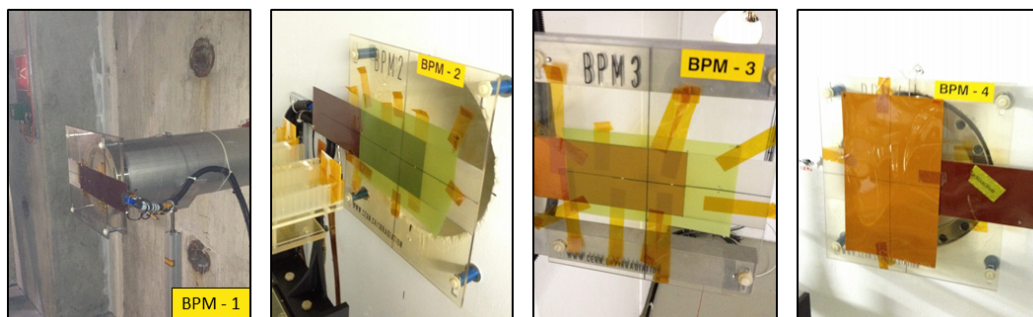

Fig. 2.6.: Fixed-BPMs in the four different positions in the T8 beam-line of the IRRAD facility, with respect to Fig. 2.1.
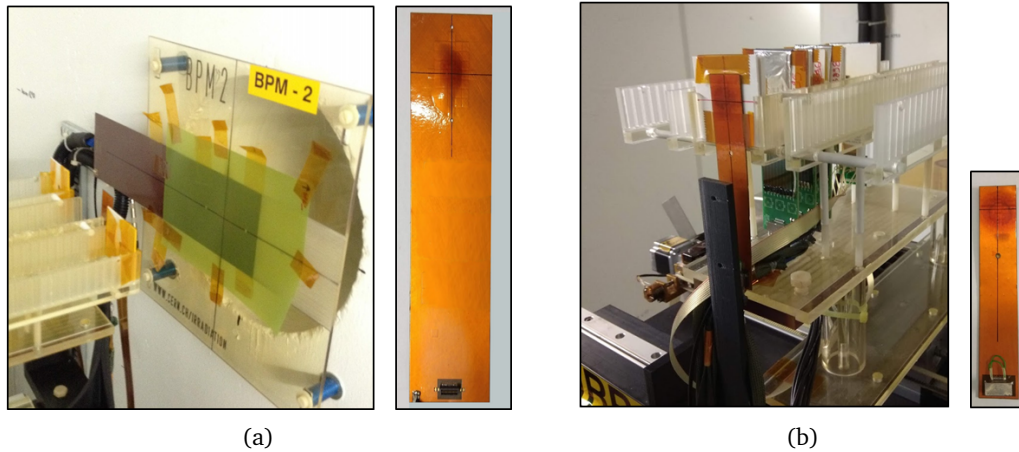
Fig. 2.7.: Different BPMs in operation setup installed in IRRAD facility, (a) with 39-pads (fixed-BPM) and (b) with 9-pads (miniBPM).

In addition to the fixed-BPM, there is the miniBPM, which consists of 9 pads distributed in a cross shape (copper pads of 4×4 mm^2 and a pitch of 0.5 mm), to measure the beam profile in two directions (vertical and horizontal). Fig. 2.8(a) shows an indicative layout and an image of a miniBPM, while Fig. 2.8(b) depicts the cross-section of the staggered sensing pads, built on a stack of six copper layers (15 um-thick) separated by six polyimide layers (80 um-thick) as an insulating substrate, with epoxy resin in between. On the top of the device, there is a ∼25 um Coverlay film as protection layer. This structure was chosen by the initial believe that multiple number of layers would multiply the output signal. The miniBPM is used to align the remote controlled tables of IRRAD with respect to the beam and thus, precisely position samples across the beam-line. In the standard configuration of IRRAD, there are three rows of samples for irradiation in each motorized table. On each table there are two BPMs installed on the central row, thus eighteen in total. Fig. 2.7(b) shows a sample of a produced device and how it looks like once it is installed in the beam-line.

The less complex device, the so-called single-pad beam monitor consists of a single Cu pad with a size of 5×5 mm^2 or 7×7 mm^2 or 10×10 mm^2 (Fig. 2.9(a)). The single-pad monitors are installed on the outer sample holder of each irradiation table, as shown in Figure 2.9(b). The beam spot can be moved by the fixed distance of $\pm$ 72 mm with respect the central position. In this way, single-pad beam monitors provide a binary signal indicating whether the samples loaded on a given sample holder are inside or outside the beam line. With this configuration, there is no need of the usage of miniBPMs which demand a nine-channel readout setup to operate. Eighteen single-pad beam monitors in total are used in the facility.

During operation, the sensing pads are placed directly in the beam and because of Secondary Electron Emission (SEE), a charge proportional to the beam intensity, is
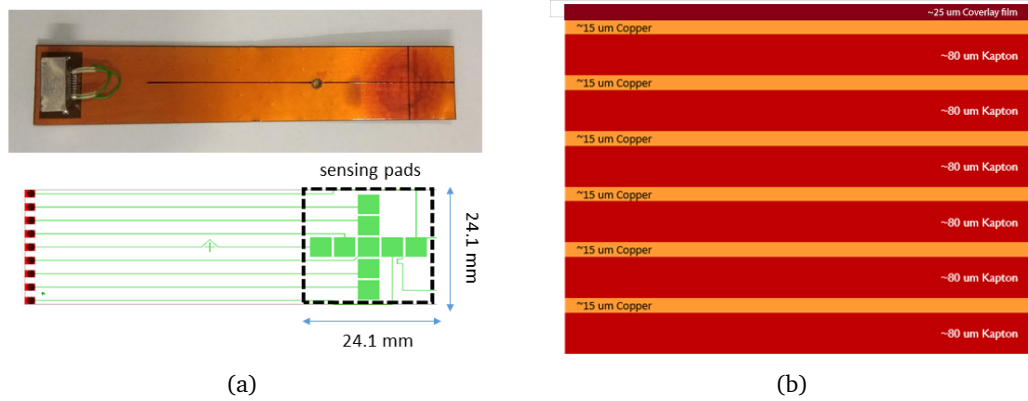
Fig. 2.8.: (a) MiniBPM layout and image of a fabricated device. (b)Cross-section of a 6-layer staggered miniBPM. The thickness of each polyimide and copper layers are indicated and there epoxy glue in between of each layer.
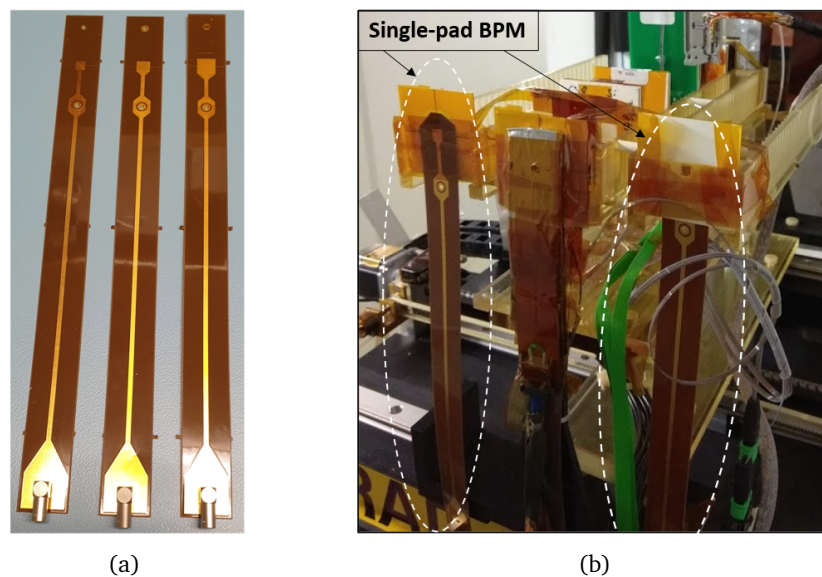
Fig. 2.9.: (a) The three sizes of single-pad monitors. (b) Single-pad beam monitor in operation setup installed in IRRAD facility.

generated on each pad. Via the multi-pin connector, the monitor is connected to dedicated readout electronics, which measures the amount of charge generated on each pad for each spill, thus resulting in a single beam measurement per spill.

The Data Acquisition (DAQ) system (more details in Appendix B) is connected to an ORACLE database where the beam information is stored and then displayed online on a web-based system. Fig. 2.10(a) shows one of the user-interface pages of the web-application developed to retrieve the fixed-BPM data. This application performs a first level data correction (e.g. noise compensation) and analysis [13]. The bottom left icon of the Fig. 2.10(a) shows the intensity distribution over each of the 39-pads of the fixed-BPM which is then converted into the horizontal (x) and vertical (y) Gaussian beam profiles. The bottom right icon provides information about the

longitudinal beam profile, by displaying the integrated beam-induced charge over time [13]. Fig. 2.10(b) shows the beam profile obtained by the miniBPM for table alignment while Fig. 2.10(c) depicts the position display table of the single-pad monitor that indicates where the beam is passing.
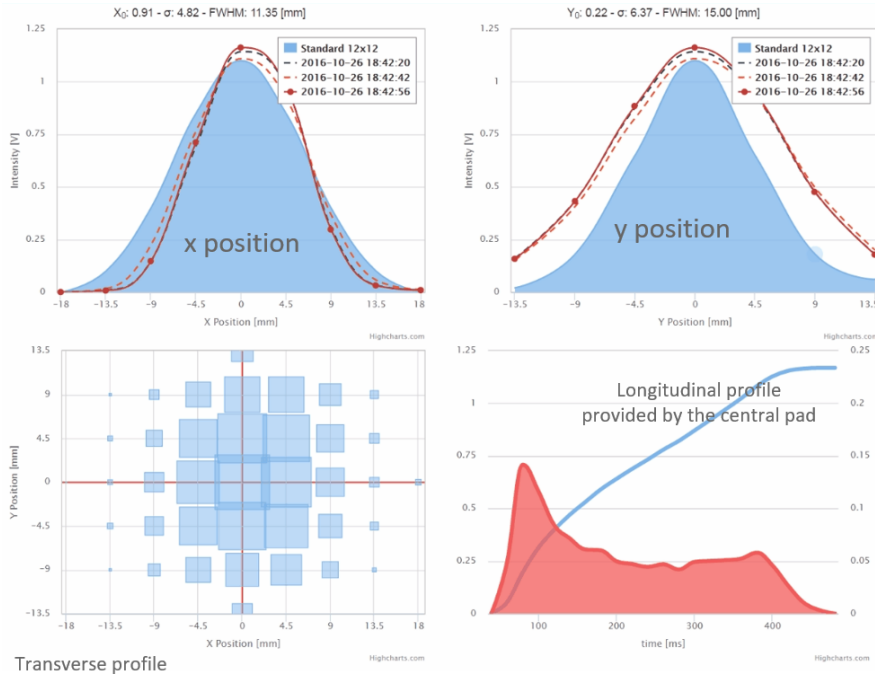
(a)
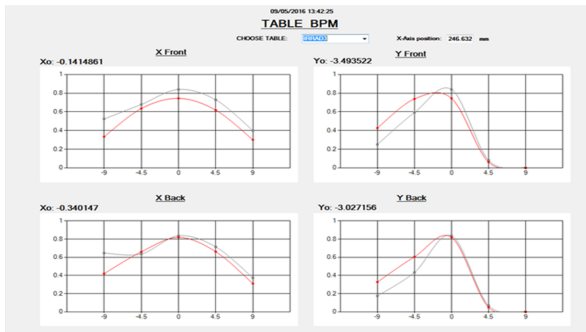
(b)
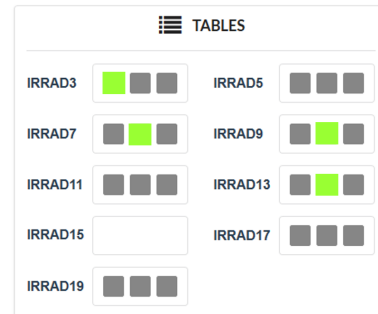
(c)

Fig. 2.10.: (a) Real-time beam profile display of standard BPM detector and (b) miniBPM device (9-pad device) for table alignment. (c) Position display table of single-pad monitor that indicates where the beam is passing.

The visualization of the beam distribution has two basic advantages. First and foremost, the full control of the beam trajectory over the ~30 m long IRRAD facility and secondly, the optimization of the irradiation of materials and samples by choosing the appropriate beam size and thus exploiting the natural proton beam divergence.

Physics of the BPM detectors

<div style="text-align: right">

3

</div>

The operational principle of the BPM detectors is based on the emission of electrons from a solid material which is induced from the bombardment of charged particles that have sufficient kinetic energy to liberate electrons from its lattice. As discussed in Section 2.3, the BPM detectors are used in the IRRAD facility with a proton beam of 24 GeV/c. However, to make possible their upgrade discussed in this, the BPMs were prior characterized in the CLEAR facility at CERN (see Section 1.3) with an electron beam of 200 MeV.

This chapter describes the relevant physics processes of charged particles when interacting with matter, the theory and applications of SEE on which the operation of the BPM detectors is based and the parameters that influence the Secondary Electrons Yield (SEY). The relevant theory is mostly taken from Ref. [21, 22].

3.1 Interaction of charged particles with matter

When a charged particles (electrons, protons, ions) traverse a medium, several different effects are produced such as x-rays, secondary electrons, backscattered electrons, auger electrons etc [23]. In the same time, the projectile particle transfers a part of its energy to the electrons of the medium; these electrons can be excited to higher energy levels, or gain enough energy to escape the potential energy level of the atom and therefore ionize it. Most frequently though, the energy that the projectile particle looses is small (for 90% of all collisions the energy losses are less than 100 eV). The energy loss[1] due to Coulomb interactions with atomic electrons is generally called electronic energy loss and leads to the heating of a material.

Heavy particles at moderately relativistic energy are subject to Coulomb interactions with the atomic electrons and the nuclei. In this case, the Coulomb interaction with the nuclei of the medium leads to the deflection (scattering) of the projectile particle from its initial direction. If the energy of the projectile particle is large the deflection is small. The energy loss due to Coulomb interactions with the nuclei is called nuclear energy loss and it is much smaller than the electronic energy loss especially at higher energies (see Fig. 3.1).

At higher energies, charged particles loose energy mainly by emission of radiation. For electrons, this effect is dominant above a few tens of MeV while for the other

---

[1]The energy loss refers to the mean rate of energy loss per unit length or mass stopping power. These connotations are used interchangeable throughout this text.

charged particles it is dominant at much higher energies because of their larger mass.
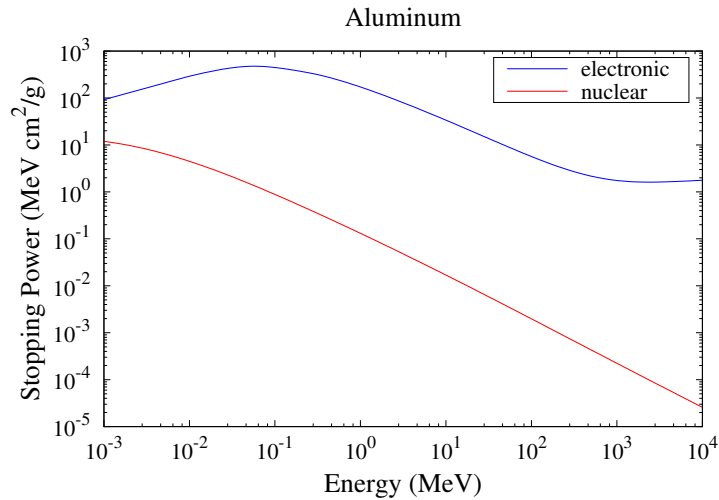
Fig. 3.1.: Stopping power of protons in aluminum as a function of their kinetic energy [24].

3.2 Electron emission from solids

The electron emission mechanism can be induced by a diversity of physical processes, depending on the source of kinetic energy supplied to the electrons. When the emission of electrons from a sample surface into the vacuum is made under the action of a high electrostatic field, the process is called field emission, also known as the Fowler-Nordheim tunnelling effect. If the surface is irradiated with light in the visible or ultraviolet (UV) region, the phenomenon is defined as photoelectric emission. If the emission is promoted by heat applied to the solid, is a thermionic emission process. When the electron emission is induced by accelerated particles as ions, electrons or protons, the process is called ion-induced electron emission (IIEE), electron-induced electron emission (EIEE) or proton-induced emission.

Within a solid material which acts as a "potential well" the electrons are prevented from escaping. This is because, in the absence of an electric field, they do not possess enough energy to overcome the potential barrier between the solid surface and the vacuum. The surface barrier is different for metals, semiconductors and insulators and the electrical conductivity of the material depends on the distribution of electrons in the allowed energy bands. Fig. 3.2 shows a schematics of the energy-band structures for these materials. The horizontal dashed line shows the Fermi level (E_f)[1] up to which the valence electrons are filled up. The blue color represents the valence band (E_v)[2] and the yellow color represents the conduction band (E_c)[2],

---

[1]The highest energy level that an electron can occupy at the absolute zero temperature

[2] The valence band is the band of electron orbitals that electrons can jump out of, moving into the conduction band when excited. The valence band is the outermost electron orbital of an atom.

while W[1] is the work function and E_g[2] the energy gap between the valence and the conduction band.
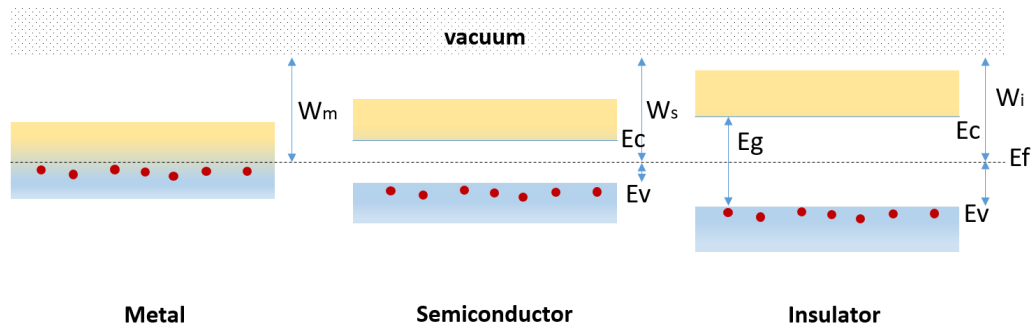

Fig. 3.2.: Schematics of the energy-band diagrams for metals, semiconductors and insulators. The horizontal dashed line shows the Fermi level up to which the valence electrons are filled up. The blue color represents the valence band and the yellow color represents the conduction band.

In metals, electrons can move freely in between the valence band and the conduction band forming a cloud of electrons responsible for the conduction of electricity in the presence of an electric field. In insulators, all the electrons are contained in filled bands thus there are no free electrons for conduction. The energy difference in between the valence band (E_v) and the conduction band (E_c) in the insulators can be as large as 12 eV. Semiconductors have a smaller band-gap (usually E_g = 1 eV) and a number of valence electrons can jump across this gap due to thermal activation. The conduction occurs because electron-hole pairs are created.

3.3 The Secondary Electron Emission process

The emission of electrons from a solid was first observed by Austin and Starke in 1902 [25] in a study of the reflection of electrons by metals; they observed that under certain circumstances more electrons were emitted than were incident, indicating that the bombarding primary electrons liberate electrons from the solid. These emitted electrons are called secondary electrons. Since then, this phenomenon has attracted the attention of scientists for more than a century but it is still not quantitatively well understood as various aspects make the quantitative interpretation of secondary electron spectra rather complex.

There are different mechanisms by which incident electrons with initial energy E_0, can lose their energy when interacting with a solid. The term "secondary electrons" is referred to all electrons emitted by the surface and collected by a positively biased collector. Although, a distinction into three groups can be made according

---

[1]The minimum energy needed to remove an electron from a solid to the vacuum
[2]Energy range in a solid where no electronic states can exist

to the different interactions and the loss of energy they suffer during the scattering process:

- True secondary electrons
- Elastically scattered SE
- Inelastically scattered SE

The true secondary electrons are defined as the electrons emitted by the sample having energy below 50 eV and are the result of a cascade process of electrons in the solid. In this case the electrons are created at (or very near) surface, reflect topography of the surface with good resolution and bear no information about inner structure of specimen [26].

Elastically and inelastically reflected electrons are defined as backscattered electrons (BSE), which have energy higher than 50 eV. Elastic interaction means that no energy is transferred from the scattered electron to the atom. In this case, an electron can be transmitted in the vicinity of the nucleus without interacting at all. An electron penetrating into the electron cloud of an atom is attracted by the positive potential of the nucleus by the Coulomb interaction and its path is deflected towards the core. In rare cases, even complete backscattering can occur (BSE).

Inelastic interaction means collision between the incident electron and the atomic electron leading to an energy transfer from the incident electron to the atomic. Subsequently the atomic electron having sufficient kinetic energy maybe be knocked out by emitting a characteristic photon (γ). The ejected electron in that case is a secondary electron. This process leads to the excitation of the atom. Fig. 3.3 shows a schematics with the different interaction processes of an incident electron with a nucleus N.
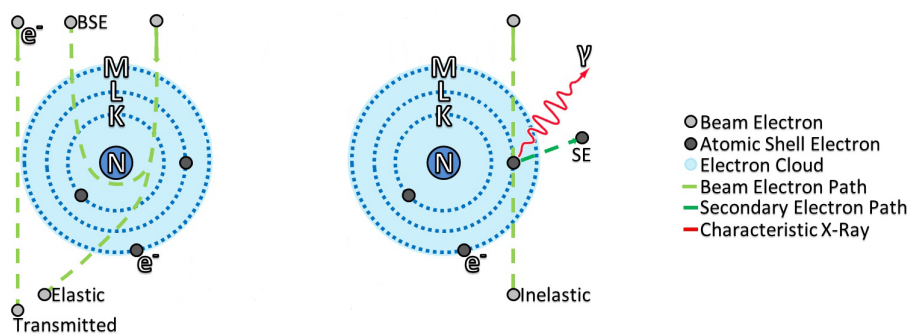
Fig. 3.3.: Schematics showing the interaction of an incident electron with a nucleus N and an electron cloud on the K, L and M shells.

Fig. 3.4 shows the energy spectrum of emitted electrons from a surface generated by a primary electron beam. The first peak corresponds to the position of the true secondary electrons at lower energies, the second peak corresponds to the

inelastically backscattered electrons, while the third peak corresponds to the fraction of primaries that are elastically scattered. The flat region in the chart consists of a mixture of the contribution of true secondaries and inelastically backscattered electrons.
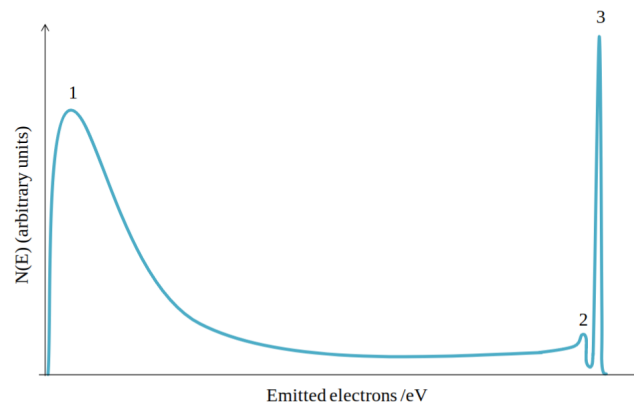
Fig. 3.4.: Schematics of the spectrum of emitted electrons from a surface generated by a primary electron beam.

The process of secondary electron emission is generally interpreted as a three-step process and is defined below (see Fig. 3.5) [27]:

a) The target absorbs the incident particles and the inner electrons excite. Some of these electrons receive enough energy to be knocked out from the atoms. The highest energetic ones, or delta rays, can themselves produce secondary ionisation.

b) The secondary electrons diffusion toward the target surface with energy loss through inelastic collisions. The probability of reaching the surface decreases with the depth at which the secondary electrons are created.

c) Some of the secondary electrons can go over the surface potential barrier.
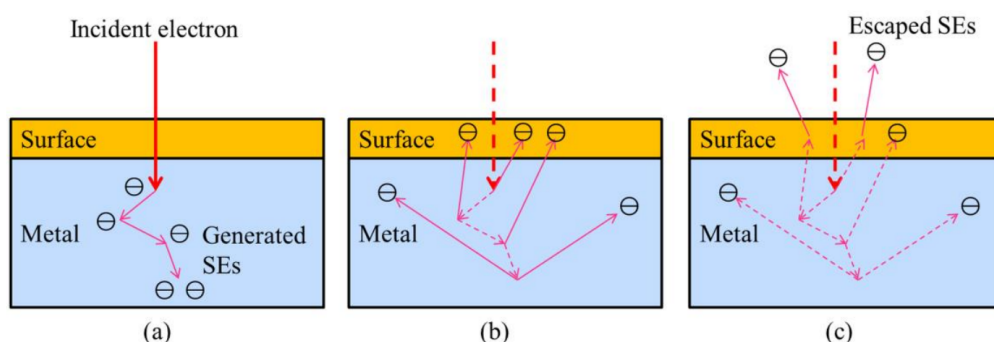
Fig. 3.5.: Schematics showing the three SEE steps from a sample.

The average number of internal electrons produced by the primary electrons (step 1) is proportional to the impact energy of the primary electrons divided by the energy

required to make an electron-hole pair. The probability of the transport toward the surface (step 2) is related to the penetration depth of the primary electron and the mean free path of the secondary electrons, while the probability that an electron which reaches the surface escapes from the solid (step 3) is a function of the energy of the electron divided by the electron affinity of the emissive material [28].

3.4 Existing applications of SEE

Secondary Electron Emission fundamental concept has a wide range of applications in diverse scientific and industrial fields. Such fields are particle-detector technology, surface analysis, displays, space satellites, medicine and radiation biotechnology [29]. Most of the applications have high-vacuum requirements.

Photomultipliers are detectors that amplify the electron current to measurable levels when a high sensitivity in the region of visible light or UV is necessary. When a photon strikes the photocathode this emits a photoelectron which is accelerated towards the first dynode where it collides and as a result of the collision secondary electrons are generated and emitted. Image intensifier tubes are based on the same principle [23, 21].

Beam diagnostic devices such as SEC, SEM-grids and Wire Scanners (WS) (see also Table 2.1) are all associated with interactions of energetic particles with solid surfaces and secondary emission. Scanning electron microscopes [26] are based on the same phenomenon, and used for surface analysis and material characterization. Other applications of SEE include plasma TV displays, advanced tools for hadron therapy, beam calibration devices and means for sterilization processes.

3.5 The Secondary Electron Emission Yield

The secondary electron emission yield (SEY) is generally defined as the ratio of the number of emitted electrons or total emitted secondary electron current (I_t) as described in Section 3.3, to the number of incident electrons or primary electron current (I_0):

$$\delta = \frac{I_t}{I_0} \tag{3.1}$$

Fig. 3.6 shows a schematics of the SEY as a function of the primary electron energy E_0. This relation has a typical bell-shaped curve with three characteristic parameters: two cross-over energies E_I and E_{II} at which $\delta = 1$, and a maximum yield δ_m at an energy E_m.
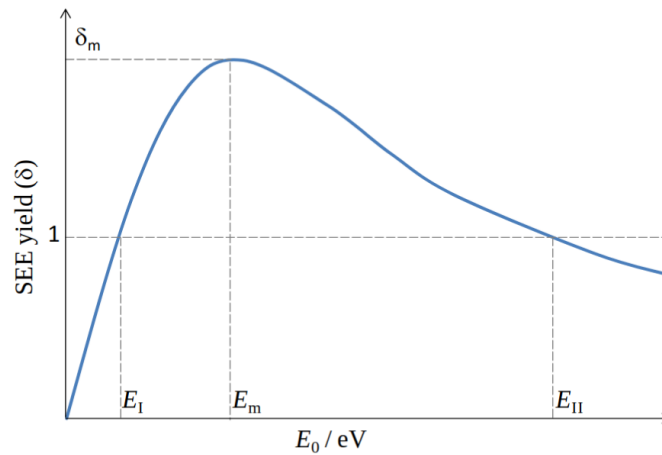
Fig. 3.6.: Schematics showing the variation of secondary electron yield as a function of the primary electron energy E_0.

The shape of the curve reflects the relation between the penetration depth of the primary electrons and the escape depth of the secondary electrons. The net current of a solid being bombarded by energetic electrons can be zero if the number of incident electrons and the electrons being emitted is the same; in this case $\delta = 1$ (at E_I and E_{II}). The location of E_I and E_{II} depends on the material, the angle of the incidence primary beam and the roughness of the surface.

○ For $E < E_I$ the primaries are not energetic enough to penetrate the surface and simply reflect back. As the primary energy increases, the number of secondary electrons emitted is increasing.

○ For $E_I < E < E_m$ the increase of δ is justified by the fact that the penetration depth of the primary electrons is shorter than the escape depth of the secondaries. The penetration depth of the primary electrons and therefore the depth at which the secondary electrons are generated increases proportionally to the primary energy. At $E = E_m$ the penetration depth becomes equivalent to the escape depth.

○ When $E > E_m$ the secondaries are generated so deep in the material that many of them lose their energy by absorption before reaching the surface and just a few of them arrive in the surface with enough energy to overcome the surface barrier.

3.5.1 Theoretical models

When primary electrons enter an emitter, they excite and produce secondary electrons and primary energy decreases. Suppose that $N(x, E)$ is the number of secondary electrons produced at a distance x from surface per primary electron of energy E and $f(x)$ symbolizes the escape probability of the secondaries. Thus, Lye

and Dekker [30] calculated the SEY (δ), proportional to the number of secondaries generated as a function of the generation depth:

$$\delta = \int_0^\infty N(x, E)f(x)dx \tag{3.2}$$

In their diffusion through the solid, electrons are assumed to follow straight paths, transferring energy and therefore slowing down by a process of collisions with internal electrons and ions. This process of energy loss is then described by the power law (stopping power) represented by:

$$-\frac{dE}{dx} = \frac{A}{E^n(x)} \tag{3.3}$$

A is an arbitrary constant proportional to the density of the material (material independent and equal to 0.35 in primary energies between 300 eV and 7 keV) and n is a fitting parameter determined through the reduced yield curves.

The number of secondaries $N(x, E)$ created at distance dx from the surface, is proportional to average energy loss dE per unit path length, divided by the average excitation energy ϵ required to produce a secondary electron:

$$N(x)dx = -\frac{dE}{\epsilon} \tag{3.4}$$

The term $f(x)$ is the escape probability of the secondaries and is an exponential function of x, according to the following expression:

$$f(x) = Be^{-x/\lambda} \tag{3.5}$$

where B is a constant <1 and takes into account the fact that only a fraction of excited electrons migrates toward surface (B = 0.5 when SE are scattered symmetrically in specimen), λ is the absorption coefficient and $1/\lambda$ the mean SE escape depth.

The maximum penetration depth of the primary electrons is proportional to the initial energy of the primary electrons E_0:

$$R = \frac{E_0^{n+1}}{(n+1)A} \tag{3.6}$$

Jenkins and Trodden calculated the number of secondary electrons with respect to the penetration depth of PE:

$$N(x) = (\frac{A}{2})^{\frac{1}{n+1}} \frac{1}{\epsilon(R-x)^{\frac{n}{n+1}}}$$ (3.7)

At high primary energies, electrons have a short interaction time with the lattice electrons and $N(x)$ is small. As the primaries lose their energy, the interaction time increases and so does $N(x)$, but the internal secondaries are generated deeper into the solid.

The escape depth of the internal secondaries generated is independent of E_0 and is associated only with the sample properties. The SE are scattered and a fraction is absorbed within the material before they reach the surface. Lin and Joy presented an analytical expression ("The universal curve") which describes the phenomenon of SEE through the following relation:

$$\frac{\delta}{\delta_m} = 1.28(\frac{E_0}{E_m})^{-0.67}[1 - e^{-1.614(\frac{E_0}{E_m})^{1.67}}]$$ (3.8)

In the literature one can find significant variation of reports for the yields measured at a given primary energy. These variations come from differences in the sample preparation methods, experimental setups or other factors. The above equation can fit all those different values and extract the best estimated results.

3.5.2 SEE from metals and insulators

The secondary electrons created inside a metal loose energy mainly by collisions with the electrons in the conduction band, by lattice vibrations and by defects. This leads to smaller escape depths of ~ 1 nm. In addition, the minimum escape energy of ~ 10 eV needed to overcome the energy barrier prevents the electrons from being emitted from the surface. Thus, metallic materials have usually small SEY close to unity, although the values of E_m and δ_m depend on the metal.

When an insulator material is bombarded with an electron beam there is a dynamic competition between two effects: an induced negative charge due to the trapping of a fraction of the incident electrons, and conversely, an induced positive charge caused by the emission of secondary electrons. These competitive effects produces a surface potential and the insulating material charges up. Insulators generally exhibit high secondary electron yields. This can be linked to their characteristic large band-gap, which prevents the secondary electrons from losing energy through electron-electron collisions, resulting in a large escape depth for the low-energy secondary electrons.

3.6 SEE dependence

The secondary electron emission is a surface dependent phenomenon [11]. It is influenced by many factors as studies have revealed [31, 32]. In this section, some of these factors are discussed.

3.6.1 Primary energy

SEE phenomenon is independent of the nature of the incident particles (positive or negative) [11]. The penetration depth of the secondary electrons (the maximum depth they are created) increases proportionally to the primary energy and thus, the number of the SE is proportional to the primary energy [23].

The high-velocity electrons of high primary energies have a relatively short time to interact with the lattice electrons, and the internal yield per unit length is low. As the incident electrons lose energy, the interaction time and thus the yield decrease. So, this effect indicates that as the primary-electron energy rises, the internal SEs are originated deeper beneath the surface [23].

3.6.2 Sensing material

In general, SE emitters are required to be made of a low cost and relatively short activity lifetime material. Materials consisting of atoms with a large diameter have small δ_{max} [26]. Foils made of Ni, Rd, Ag, W, Au give stable operation but in certain experiments they cannot be used because of the high γ-background from the bremsstrahlung and the multiple scattering of the electrons [33]. Commonly used secondary emissive materials include Al, Au, Cu, stainless steel, CuBe, Ag and Ti. For better performance, they are normally coated with oxides [23].

3.6.3 Surface conditions

Insulating layers (e.g. oxides, adsorbed water) play a dominant role in secondary emission enhancement [31] because of low potential barrier and Malter effect (charging effect). The surface potential barrier of an metal with oxide is lower than the one without oxide, which means that there is a higher probability of electrons to escape from oxide surface. Monte Carlo simulations have shown (Fig. 3.7) that the surface potential barrier of the RuO_2 is lower than that of the Ru, thus, the generated SEs escape faster from the sample coated by native oxide [34].

According to the Malter effect, if the oxide material is an insulator and the surface is positively charged, the charge produces a high electric field in the insulator and this will pull more electrons from further beneath the surface. Thus, the electron emission is caused by field emission at the bulk material through the insulating layer [35].
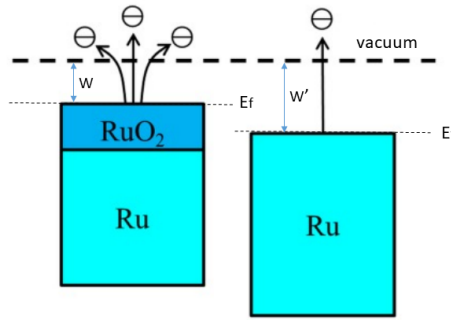
Fig. 3.7.: Schematic illustration of SEE from the surfaces of Ru with native oxide and without, where Ef is the Fermi energy, and W and W' are potential barriers such as work function of RuO_2 and Ru, respectively.

3.6.4 Angle of incidence

The angular distribution of the SE is nearly independent of the angle of the incidence electrons and is approximately a cosine distribution. BSE orient according to the direction of the incident particles radius. An example of angular distribution from a single-crystal sample surface is shown in Figure 3.8.
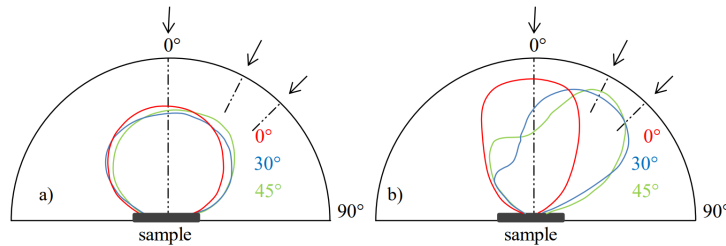
Fig. 3.8.: Angular distribution of (a) SE and (b) BSE emitted from polycrystalline.

When the angle of incident beam is θ, with respect to the surface, then the total yield can be calculated from the equation:

$$\delta(\theta) = \delta(0)cos^{-1}\theta \tag{3.9}$$

where $\delta(0)$ is the total perpendicular yield. Thus, when incident beam is positioned at an angle, the maximum penetration depth is reduced by a factor $cos(\theta)$ and higher yields are obtained.

3.6.5 Surface roughness

When SE are emitted from a rough surface there is a possibility for them to be intercepted by neighbouring irregularities, which may send them back to the surface. On a smooth surface, on the other hand, the electrons face no further obstacles

in their trajectory and can escape easily. An example is microcrystalline films of different thicknesses. The rough targets show no dependence upon the angle of incidence [36].

3.6.6 Vacuum

The phenomenon of SEE from thin metal foils is entirely a surface one. One of the influential factors on SEE is the condition of the foil surface. Large SEY is observed when the process takes place inside high vacuum chambers, as it is easier to collect the electrons generated by the beam as they are flowing in larger amount from the emitting material [11].

3.6.7 Parameters explored in the context of this thesis

Because of time constraints and the variety of the effects playing a role in the SEE (besides the stop of the activities due to Covid-19 pandemic in the first half of 2020), we managed to explore only a few of the parameters mentioned above. The choice of the parameters was made according to their relevance for the fabrication of an upgraded beam monitor for IRRAD namely, possibility to achieve low mass, short radioactivity, higher SEY, increased radiation endurance, low cost and easy manipulation. Thus, permanent and real time beam monitoring. More specifically, the metals that attracted our interest the most was Cu, Cr and Al, because of high SEY and availability in the micro-fabrication clean-room facility. Coating of the metallic surface with Al_2O_3 was also performed and evaluated. Roughness of the metal was examined and tested, as well. The yield of aluminum was measured in a vacuum chamber and in air for comparison.

First microfabricated devices on Si-SiO$_2$ substrate

<div style="text-align: right">4</div>

The BPM devices were successfully operated in the IRRAD facility from 2014 until 2018. However, the impact of radiation exposure created the need of their improvement and replacement. Thus, a new fabrication method started being developed, based on nano-layer metal deposition.

In this chapter, the new fabrication method is described in detail and the first prototypes of the new BPM devices are presented. A deeper insight is given into the chosen layout, the fabrication steps, the experimental runs, the electrical connectivity and the readout system used for the new prototypes. Most of the information given below is based on the AIDA-2020 [37] scientific/technical Note, cited in Ref. [38].

4.1 Issues of BPM detectors based on the PCB technology

The long term radiation exposure of the BPMs had critical impact on their performance. Firstly, several of the them showed damages. As it can be seen in Fig. 4.1, in the region were the beam was passing, the top Coverlay film got damaged and it was detached from the layer below. The color of this layer reveals burning and "bubbles" structure appeared in the same area. A possible reason can be the usage of epoxy glue in between the copper and the PCB layers. Also, the top layer was not well pressed with the glue and air filled in the region in between.
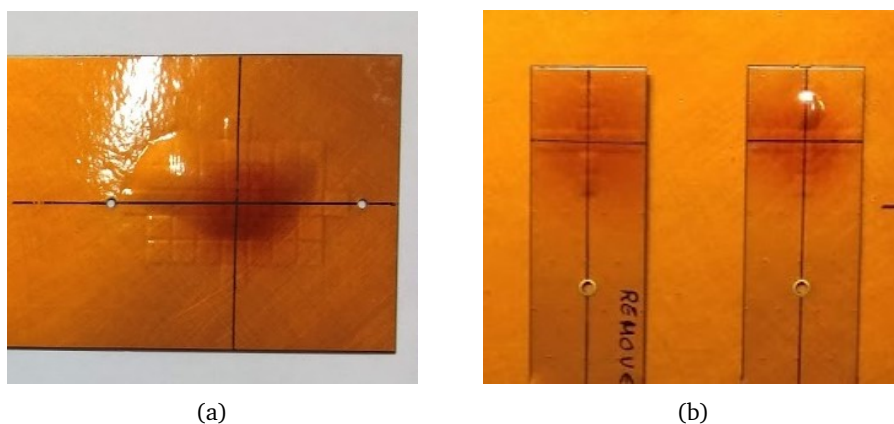

<div style="text-align: center">(a)   (b)</div>

Fig. 4.1.: Damages on (a) fixed-BPM and (b) miniBPMs after 4 years of operation in the IRRAD facility.

Other than the damages, the devices became highly radioactive after long time exposure, something of special concern when the facility staff needs to replace a broken device. Lastly, when all the irradiation tables are inserted in beam, the sum of all BPMs can add almost 2 mm of copper and 8 mm of polyimide to the total material budget in the beam line. This contributes to the scattering of the primary protons and the beam becomes rich of secondary particles in the last table in the line. Taking into consideration these issues, a research for an alternative way to produce the BPMs has been initiated and will be described in the following, addressing first their requirements.

4.2 Requirements of the BPM

In the IRRAD, the BPM need to satisfy certain requirements. First and foremost, they should withstand high-radiation levels and particle fluence levels equivalent at least, to one year of operation in the facility (10^{17}-10^{18} Protons On Target (POT)). The beam monitoring must be permanent and real-time, because the BPMs' measurements are used by the control center to tune the extraction parameters (e.g. shape, position, charge). In addition, the BPMs should be made of materials that have short radioactivity, in order to minimize the exposure of the operators and relatively low cost. Last but not least, they have to be, on the one hand, thin to avoid the proton scattering and the interference with the projectile beam and on the other hand, thick enough to allow easy handling.

4.3 New BPMs based on microfabrication

The new devices are based on microfabrication. This technique allows the deposition of very thin metal layers ($<$1 um) on a passive substrate without the need of gluing materials. In this way, an increased transparency to the incident beam and a higher radiation resistance can be achieved. Five different prototypes were manufactured in order to investigate the new fabrication method and were tested in the IRRAD facility. From all these prototypes, only one was working properly constituted the proof of concept for carry-on future developments.

4.3.1 Design and fabrication

The new BPM devices, the so-called microBPMs, were designed with the same layout as miniBPM to avoid the complex structure of the fixed-BPM with the 39 pads in the experimental stage. The active area consists of nine sensing pads covering a region of 24.1×24.1 mm^2 in order to be compatible with the size of the standard proton beam in the IRRAD (5×5 mm^2 to 20×20 mm^2). The sensing pads have a size of 4×4 mm^2 and a pitch of 0.5 mm, in the shape of a cross. In this way, the device

provides the beam profile in the two Cartesian coordinates. The sensing pads are routed towards the multi-pin connector with traces of 100 um in width. The total size of the device is 24.1×80.5 mm, as shown in Fig. 4.2.
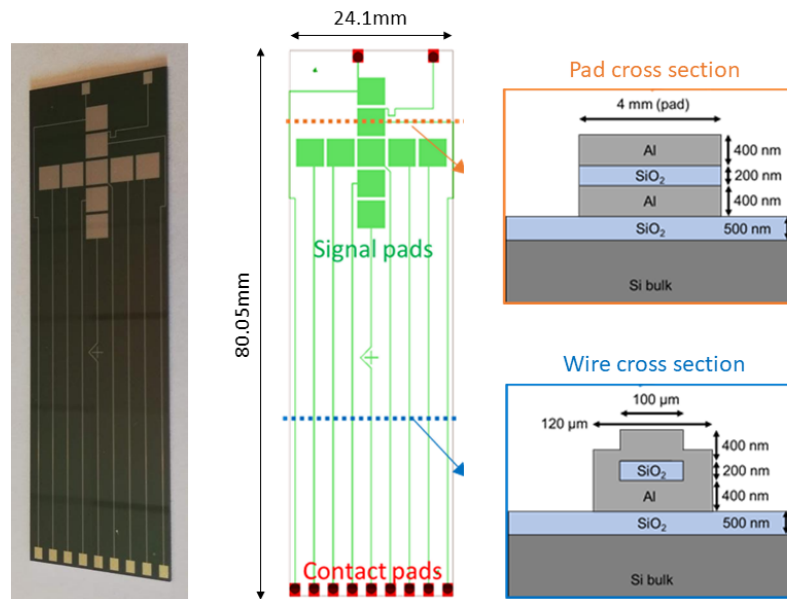

Fig. 4.2.: On the left, image of the working microfabricated prototype with 400nm Al. On the right, cross section of a trace taken along the blue line in (bottom), and cross section of a pad along the orange line (up), of the Si-2x-400 nm microBPM.

The fabrication of the new devices was carried out at the Center of Micronanotechnology (CMi), the state-of-the-art class-100 cleanroom at the Ecole Polytechnique Federale de Lausanne (EPFL) in Switzerland. For all the devices, a silicon wafer with a thickness of 525 um and a diameter of 100 mm was used as a mechanical support (CMi test wafer). The top of the wafer was covered by a 500 nm SiO$_2$ layer (obtained with wet oxidation) in order to insulate the metal from the silicon substrate. This support was chosen due to the availability in the cleanroom and the compatibility with the processing tools. One of the devices was featuring a polyimide (PI) layer between the support wafer and the metal, as part of the substrate investigation process.

The metal that was chosen as active layer was aluminum (Al) because of its relatively low atomic number and thus, low density and radioactivity. In addition, aluminum was easy available as sputtering target at CMi. The process flow adopted for the fabrication of each device is described in the following:

- Si-1x-8 um was fabricated by sputtering 8 um of Al on the Si-SiO$_2$ substrate. A photolithography step after the deposition was carried out to produce the desired layout of the pads (detailed process flow in Appendix C).

- Si-1x-400 nm was fabricated by the same process, changing only the thickness of the Al layer.

- Si-1x-50 nm fabrication followed similar steps to the previous ones. In addition, for this production, a final SiO_2 passivation layer was added on top, to protect the Al traces between the pads and the contact pads. This SiO_2 layer was first sputtered (400 nm thick) and then patterned by photolithography and subsequent etched, to open vias for the contacts.

- Si-2x-400 nm was fabricated by 400 nm Al sputtering on the substrate, then deposition of 200 nm SiO_2 and finally another 400 nm Al layer. The intermediate SiO_2 layer was patterned with trenches along the signal traces so as the second metal sputtering step would result in the connection of the two metal layers (Cross section shown in Fig. 4.2).

- PI-1x-400 nm was fabricated by spin coating of 10 um thick polyimide layer on the substrate and then following the same process performed for Si-1x-400 nm.

The five different prototypes that were produced with microfabrication and their characteristics are summarized in Tab. 4.1.

Table 4.1.: List of the first microfabricated devices.

N^o	Test name	Substrate	N^o of layers	Al thickness	Connection type
1	Si-1x-8um	Si-SiO_2	1	8 um	DB9
2	Si-1x-400nm	Si-SiO_2	1	400 nm	DB9
3	Si-1x-50nm	Si-SiO_2	1	50 nm	SAMTEC
4	Si-2x-400nm	Si-SiO_2	2	400 nm	SAMTEC+DB9
5	PI-1x-400nm	Si-SiO_2 coated with 10 um PI	1	400 nm	SAMTEC

4.3.2 Electrical connection

In order to electrically connect the microBPM to the DAQ system, an supporting readout PCB compatible with the commonly-used sample-holder was manufactured. Each contact pad of the microBPM was wire-bonded to the PCB (see more in section 5.2), which was hosting a connector. Two types of connectors and cables were used, the DB9 connector and the FCS8-10-01 SAMTEC connector. The first one was connected to the PCB by direct soldering of the wires from a 20 (or 60) cm long flat-cable. A DB9 to LEMO converter was then used to transfer the signal to the control room over coax cables (Fig. 4.3(a)). The second one, allowed to connect the microBPM to the existing micro-coax cables, avoiding the noisy flat-cable (Fig. 4.3(b)).

In order to compare these two different connection methods, two identical microBPMs were produced (N° 4 in Tab. 4.1). The experimental runs showed that

the SAMTEC connector was giving higher and more reliable signal [38]. In the attempt to provide a shielding to the outside noise and clean up the signal, some measurements were performed with the microBPMs wrapped in aluminum foils (Faraday cage effect), as shown in Fig. 4.3(c). Nevertheless, no amplification was recorded.
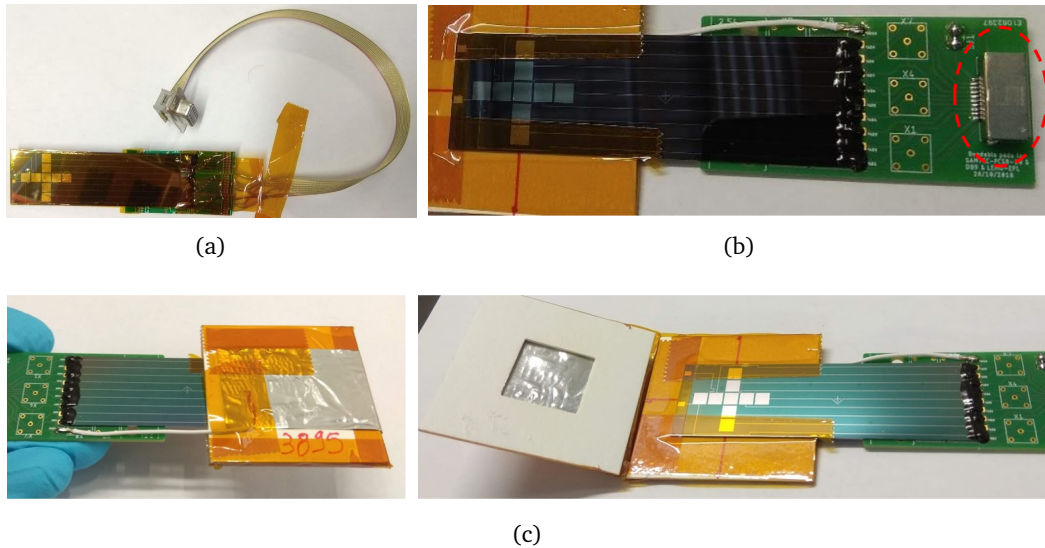

(a)   (b)

(c)

Fig. 4.3.: (a) PCB with DB9 connector and (b) PCB with SAMTEC connector. (c) BPM wrapped in aluminum foils.

4.3.3 Experimental Run in the IRRAD proton facility

In order to test the new BPM devices, several irradiation experiments were performed at the IRRAD Proton Facility during 2018. The devices were mounted on a sample-holder (Fig. 4.4) and connected to the DAQ system. A miniBPM was placed back to back with the new BPMs allowing a direct comparison of the electrical signal measured from each microBPM while being crossed by the same proton spill.

Due to the short available time for testing before the end of the 2018, the last period when proton beams were available at CERN before the Long Shutdown 2, most of the devices were installed in the facility without any prior electrical testing. Moreover, many difficulties were encountered to connect the devices to the DAQ system, as is presented in the NOTE [38]. As a consequence, the results of the experiments were not satisfactory for most of the tested devices. Significant differences in signal level were observed among the different pads, with some channels showing very small signal while, for some, the voltages given by the integrators saturated the ADC even for very low intensity beams. Faulty connections or defects in the fabrication are most likely responsible for these effects. The only fully working prototype was the Si-1x-400 nm.
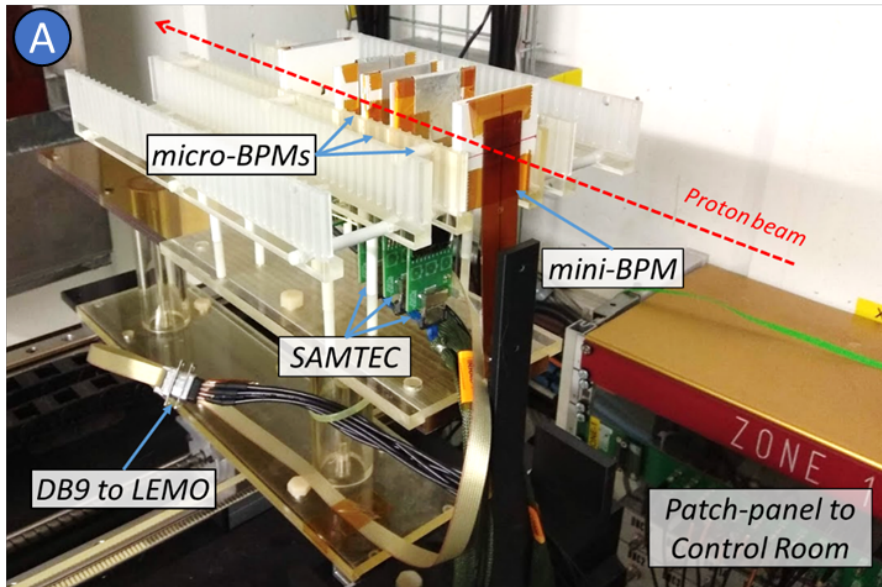
Fig. 4.4.: MicroBPMs with DB9 and SAMTEC connectors, installed on the irradiation table in the IRRAD, together with a reference mini-BPM.

In order to study the response of the device with respect to different particle fluxes, the beam intensity was lowered, in five steps, from 8×10^{11} p/cm^2 to 10^{11} p/cm^2. Fig. 4.5 shows the accumulated transversal and longitudinal profiles during the intensity scan for both devices. Even though the measurements from the two devices are, qualitatively, in good agreement, the profiles measured by the microBPM appear to be slightly broader than the ones measured by the miniBPM. A possible explanation for this effect can be the existence of cross-talk between channels in the microBPM (maybe induced by the underlying and not perfectly insulating substrate), leading to a smearing of the profiles.
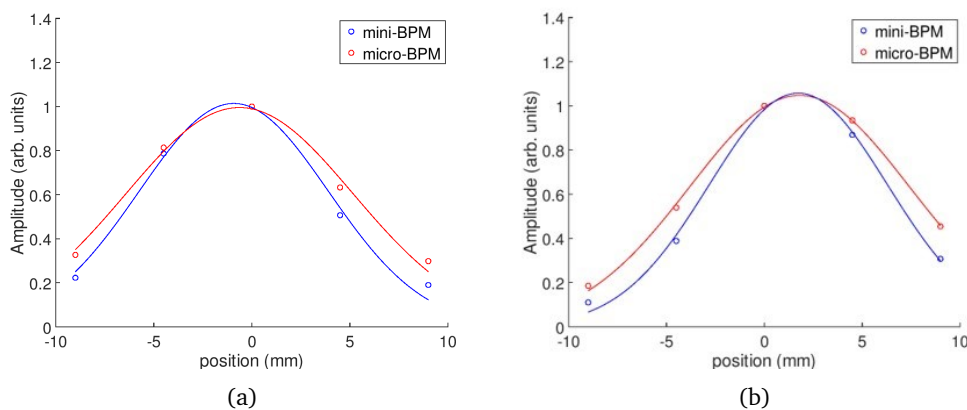

Fig. 4.5.: Accumulated (a) transverse and (b) longitudinal profiles measured by the mini-BPM (blue) and microBPM (red), during the beam intensity scan.

Fig. 4.6 shows the beam profiles acquired with the miniBPM and the microBPM Si-1x-400nm for three consecutive spills. The red lines correspond to the current spill,

while dashed lines correspond to the previous proton spill (orange) and one before (black). The blue, filled area represents the expected profile with standard beam conditions. A very good resemblance is clearly visible for both X and Y directions.
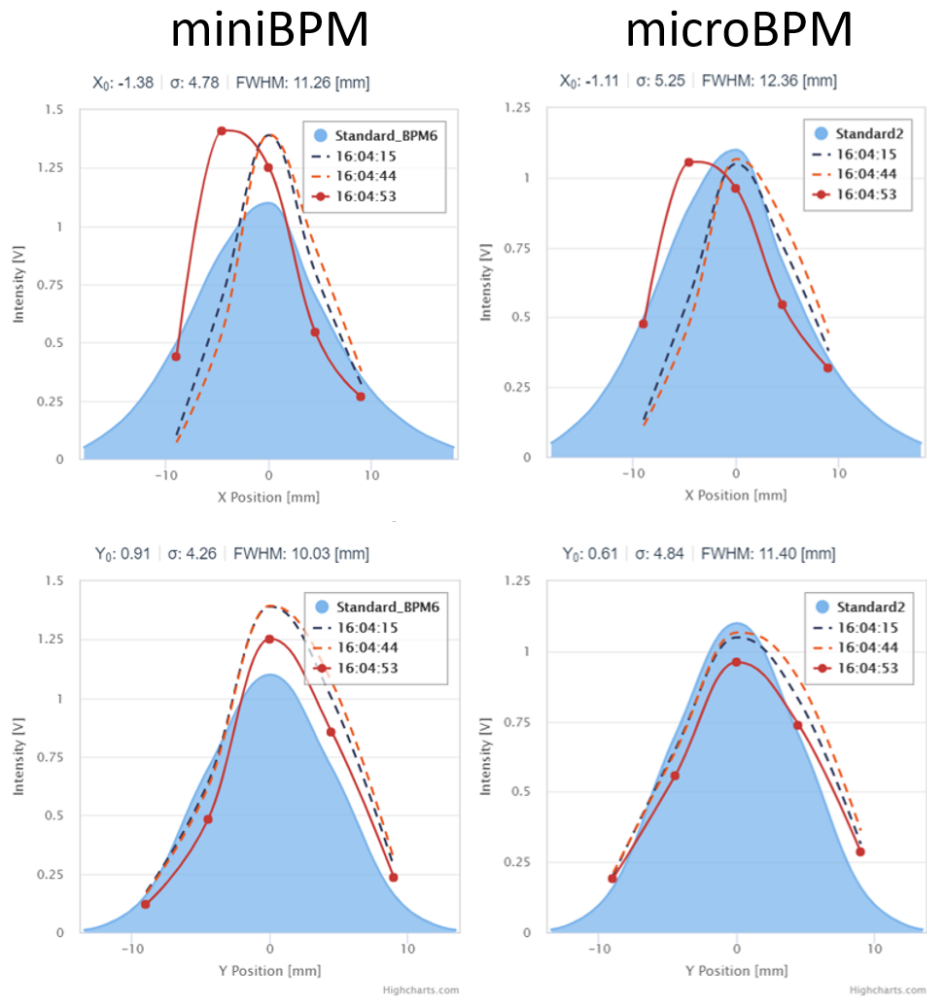

Fig. 4.6.: Comparison between the profiles of three different proton spills measured with a mini-BPM and a microBPM for the Si-1x-400nm. The red lines correspond to the current spill, while dashed lines correspond to the previous proton spill (orange) and one before (black). The blue, filled area represents the expected profile with standard beam conditions.

Fig. 4.7 shows a scatter plot of the voltages measured by the microBPM versus those measured by the miniBPM, for all spills during the intensity scan. The different colors represent the 9 different pads of the cross pattern. The signal level, while slightly lower for the microBPM remains comparable to the miniBPM. All microBPM pads show a similar correlation with their miniBPM counterparts, with some variance which could be attributed to the non perfect alignment of the 2 detectors, and the focusing or defocusing of the beam from one device to the other. The non-linearity between the two devices must be attributed to the microBPM, since the miniBPM response is known to be linear in this range of operation.
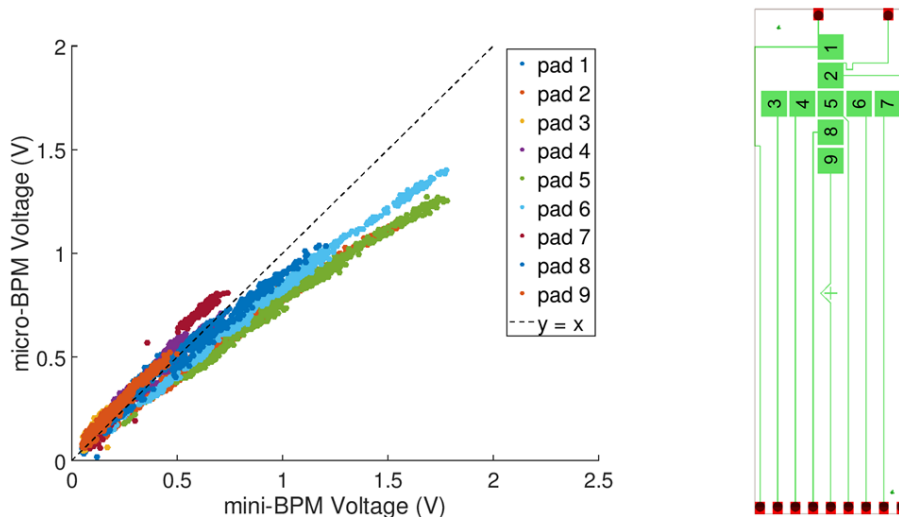
Fig. 4.7.: Scatter plot of the voltage measured by a 400 nm Al on Si microBPM as function of the voltage measured by an old mini-BPM installed back to back, during the beam intensity scan. Different colors represent the different pads of the cross-shaped devices. On the right, numbering of the pads.

4.4 Conclusions

This chapter details the study of the first batch of microfabricated Beam Profile Monitors for the IRRAD facility. Due to the unreliable connectivity between the BPMs and the readout electronics the results from the experimental tests are summarized as following providing an updated version to the Note cited in Ref. [38]:

- The fully functional prototype was the device with the 400 nm Al sputtered on the silicon substrate (Si-1x-400nm) which provided SEY comparable to the old BPM.
- The signal measured by the rest of the prototypes was comparable but at the same time problematic because of defects in the fabrication and/or bad electrical connectivity. A general deduction was that the thickness of the sensing layer does not influence the signal intensity.
- The connectivity issues were resolved by wire bonding the microBPM to an supporting readout PCB and using the SAMTEC connector to readout the signal.

The fully functional device that was demonstrated, provided the following benefits: less material budget, allowing the possibility of installing more BPMs on the same beam-line without further degrading, reduced volumes of interaction with the beam which results in less activation and higher radiation resistance because of the absence of glue in between the layers, thus less maintenance needed.

Experimentation on BPMs fabricated on Si-SiO$_2$ substrate

<div style="text-align: right">5</div>

After the successful fabrication and testing of the new BPMs, the next step of the research was focused mostly on the parameters that influence the secondary electron emission. In this context, new devices based on the previous working prototype, that was discussed in Chapter 4, were fabricated with the same layout and were tested in the CLEAR facility at CERN.

5.1 Motivation

The main goal of this fabrication was to master the same techniques used in the preliminary stage, focusing on single metallic layer devices. The working prototype, 400 nm aluminum on Si-SiO$_2$ substrate was taken as template. The second goal was to understand if an extra oxide layer on top of the metal can influence the secondary electron emission (see Chapter 3) and what will happen by connecting the silicon substrate to the same ground potential as the PCB. The logic behind the latest, was the same with wrapping the device with aluminum in order to make a shielding to the external noise level (see section 4.3.2).

5.2 Fabrication

Four different prototypes were fabricated in the Center of Microtechnoloy (CMi) at EPFL. In all the devices 400 nm Al was sputtered on top of the Si-SiO$_2$ substrate, as was described in section 4.3.1. The additional features for each one are listed below:

- microBPM1 was fabricated with an top coating of 10 nm Al$_2$O$_3$ deposited by atomic layer deposition (ALD). In addition, a hole[1] was opened and filled in with Cr/Au in order to connect the silicon substrate to the same ground as the PCB (Cross section shown in Fig. 5.1(a)). .

- microBPM2 was fabricated with extra oxide layer but without substrate grounding.

- microBPM3 was an accurate reproduction of the Si-1x-400nm device.

---

[1]The process flow for the ground pad can be found in Appendix C.

- microBPM4 was fabricated with substrate grounding pad but without extra oxide layer.

The four new prototypes that were produced with microfabrication and their characteristics are summarized in the following table.

Table 5.1.: List of the second butch of microfabricated devices.

N^o	Test name	Al_2O_3 layer	Substrate grounding
1	microBPM1	10 nm	✓
2	microBPM2	10 nm	-
3	microBPM3	-	-
4	microBPM4	-	✓

Fig. 5.1(a) shows the cross sections of a sensing pad, the traces and the pad made for substrate grounding of microBPM4. MicroBPM1 and microBPM3 fixed on the readout PCB are shown in Fig. 5.1(b).
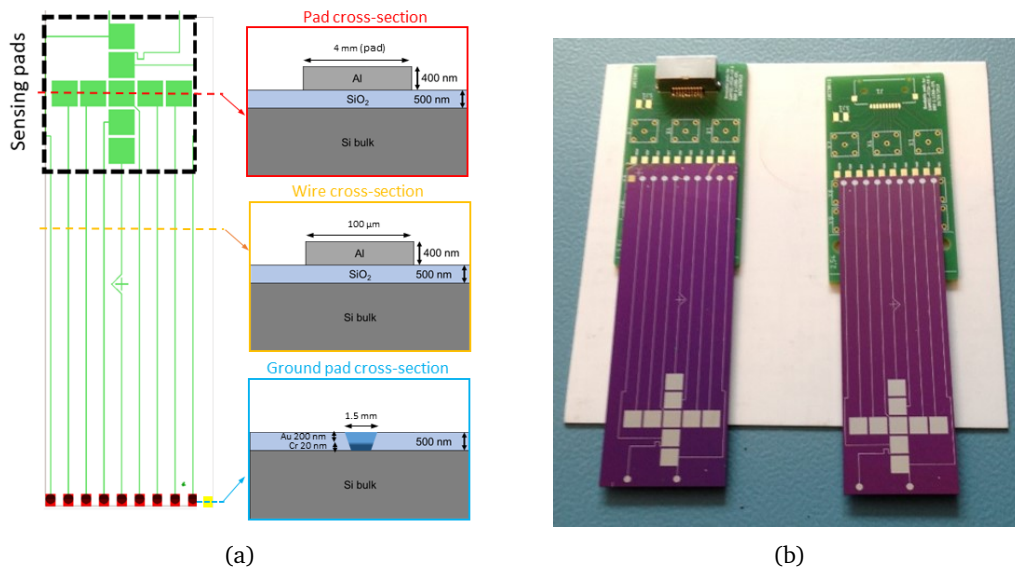

(a)   (b)

Fig. 5.1.: (a) Cross section of a sensing pad along the red line, cross section of a trace taken along the orange line and cross section of the substrate grounding pad along blue line,of the microBPM4. (b) Image of microBPM1 (left) and microBPM3 (right) fixed on the PCB-support.

The electrical connection between the microBPM and the readout PCB was realized by wire-bonding. Fig. 5.2(a) shows the bonding wires, two on each pad to assure the connection. In order to protect the wire-bonding, an insulating layer of epoxy glue[2] was applied on the top of the wires, as shown in Fig. 5.2(b). With the epoxy glue, the attachment of the detectors to the PCB was made, as well. The BPM weas

---

[2]Baked for 30 min in the oven at 120°C

connected to the DAQ electronics with the SAMTEC connectors, as proved to be the best available option (see section 4.3.2).
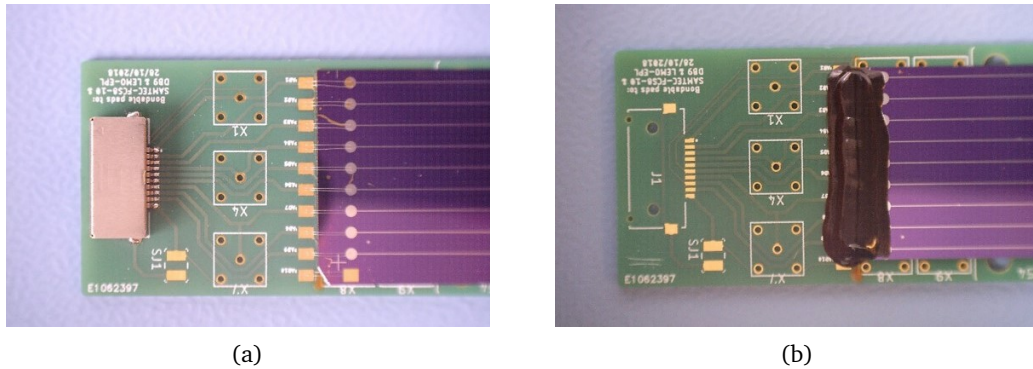

<div style="text-align:center">(a) (b)</div>

Fig. 5.2.: (a) Wire-bonding between the microBPM and the PCB-support.(b) Epoxy glue on the top of the boning wires.

5.3 Characterization of the new BPMs with electron beam in the CLEAR facility

The performance of the microBPMs has been studied in the CLEAR facility at CERN, with 200 MeV electron beam. The spill duration was less than 1 ns with a fixed rate of 1-1.2 spills/sec. Two test-stands were used: the VESPER and the THz. In order to perform the tests, the readout electronics of the IRRAD facility were used. More specifically, the data acquisition was accomplished with the BPM-readout box (see Appendix B) while the trigger signal provided by the CLEAR facility was used to synchronize the DAQ-system with the spills. A pulse generator was used to delay the trigger signal and acquire the next spill. Fig. 5.3 shows the installation setup in the VESPER.
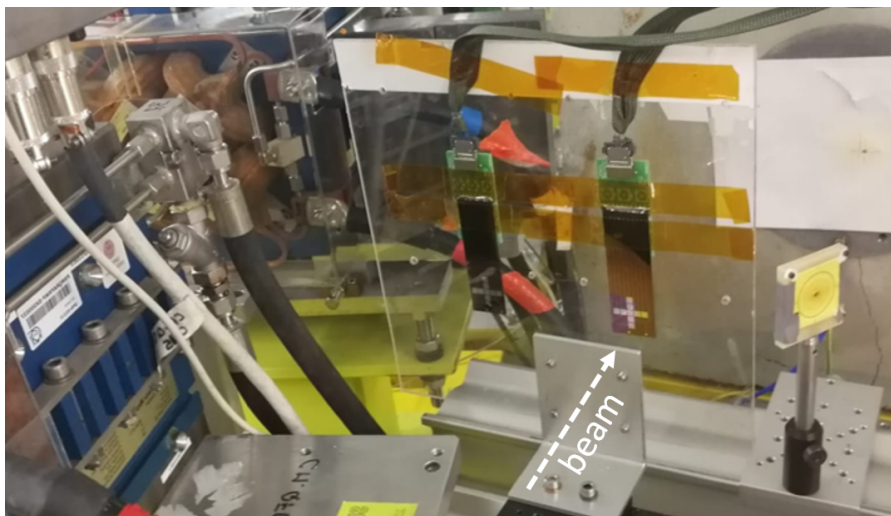

Fig. 5.3.: Installation setup in the VESPER.

Initially, the Si-1x-400nm device was tested in the VESPER, which was the only functional prototype described in Chapter 4. Unfortunately, the output signal recorded by this device was very low revealing a degradation. Possible reasons for the failure of the device is either the oxidation of the Al or a connectivity loss between the sensing and connecting pads since this device was not used for 10 months. Subsequently, a miniBPM was placed in the VESPER beam-line in order to obtain a reference profile. The miniBPM was irradiated with electrons for the first time and the beam profile was clearly observed.
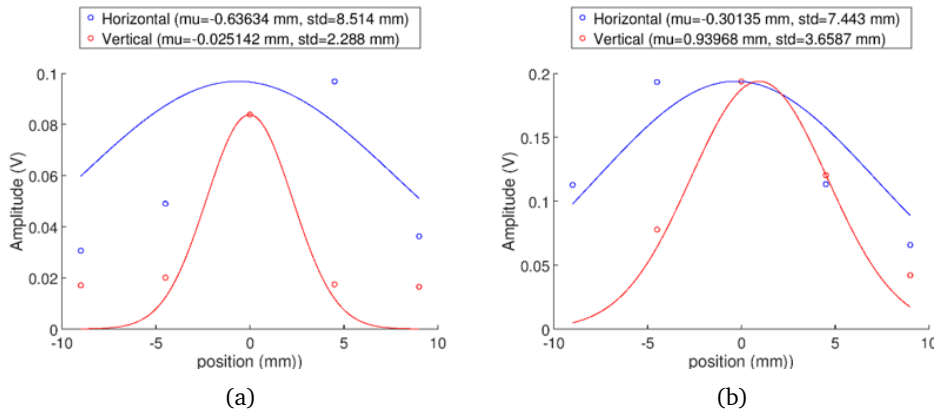

(a)   (b)

Fig. 5.4.: Beam transverse profile measured by (a) miniBPM at Q=3.5 nC and (b) microBPM3 at Q=5.2 nC in VESPER. The solid line is the theoretical profile, obtained from VESPER configuration file and the markers correspond to the measurement.

Among the new prototypes, a transverse profile was acquired only by the microBPM3 which was the accurate reproduction of the Si-1x-400nm device. Data analysis was performed on the functional devices: miniBPM and microBPM3. Fig. 5.4(a) shows the profile obtained by miniBPM with 3.5 nC beam charge while Fig. 5.4(b) presents the profile obtained by microBPM3 with 5.2 nC beam charge. The blue colour represents the horizontal profile while the red represents the vertical. The solid lines are the fitting profiles with respect to the measured values from the nine pads (markers). The profile in the horizontal axis is much broader than in the vertical axis because of the rectangular shape of the beam (see section 1.3).
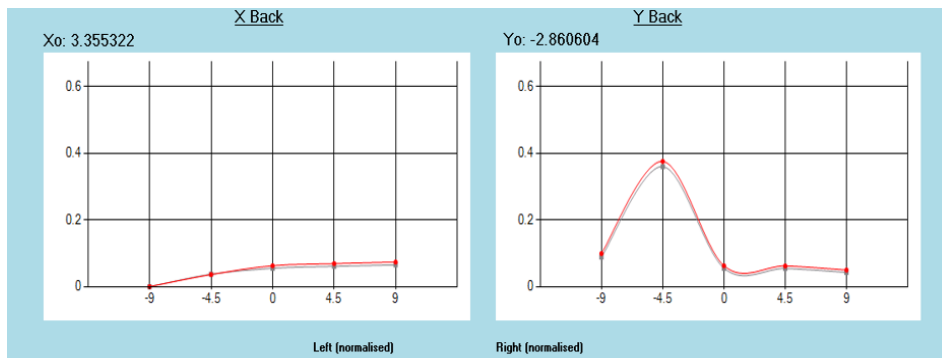

Fig. 5.5.: Signal obtained with MicroBPM2 when the beam of THz was focused on the pad mapped to the coordinate -4.5 on the X axis.

MicroBPM1 had both extra features (substrate grounding and extra oxide) and it didn't measure any signal, probably because of defects in the fabrication and/or poor electrical connectivity. Fig. 5.5 shows the signal measured with the microBPM2 (featuring extra oxide layer), when the beam was focused on the pad mapped to the coordinate -4.5 on the X-Y axis. It is possible to observe that the beam generates a signal, although the oxide layer does not give any amplification. MicroBPM4, the device with the grounded substrate (and without an extra oxide layer) recorded an inverted profile in the beginning, as shown in Fig. 5.6(a). A possible reason is cross-talks between the channels.

(a)

(b)
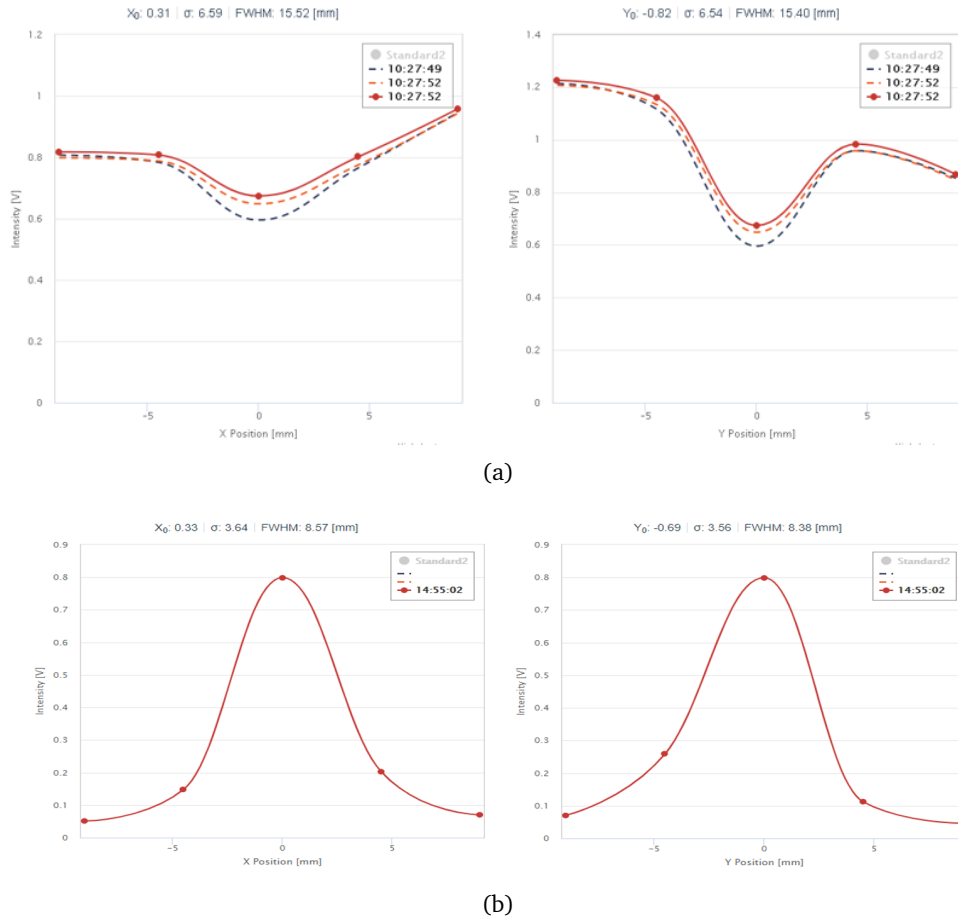
Fig. 5.6.: Beam profile measured at 6 nC beam charge with (a) microBPM4 in the VESPER and (b) microBPM4 when ground connection was removed in the THz.

During the second irradiation run at the THz this time, the substrate grounding of microBPM4 was disconnected and the device was converted into an identical to microBPM3. Fig. 5.6(b) shows the Gaussian profile that was measured. MiniBPM and microBPM3 were irradiated in the THz as well, to cross-check the results obtained in the VESPER. Fig. 5.7 shows a comparison between the transverse beam profile obtained from the miniBPM (blue markers) and the microBPM3 (red markers) in X and Y directions in THz test bench. The charge applied on the miniBPM is 2.2 nC/pulse and on the microBPM is 2.6 nC/pulse for several minutes. The solid

line is the theoretical profile, obtained from VESPER beam configuration file and the dashed line is the Gaussian fitting with respect to the measured values (markers). MicroBMP3 has shown a higher sensitivity to charged particles in comparison to the previous fabrication technology (miniBPM). Nevertheless, the remarkable difference in the signal can be misleading, as the current measured in detectors with SiO_2-Si substrate is found to be higher as compared to insulating substrates [39].
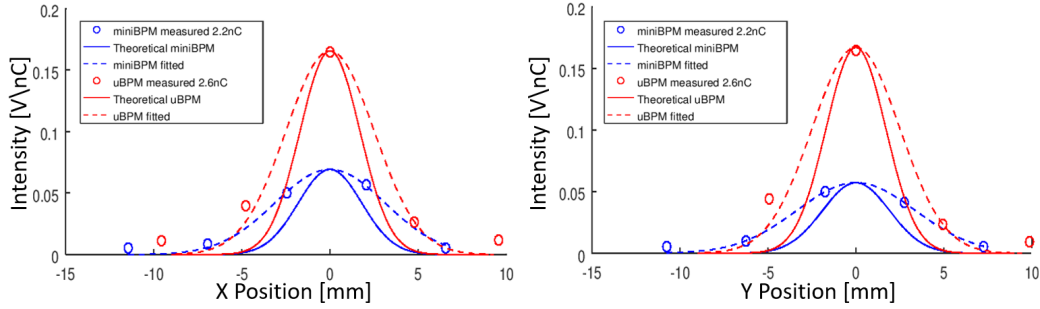

Fig. 5.7.: Measurement of electron beam transverse profile by miniBPM (σ_x=1.8mm, σ_y=1.9mm) and microBPM3 (σ_x=1.7 mm, σ_y=1.7mm) in the THz. The solid line is the theoretical profile, obtained from VESPER configuration file and the markers correspond to the measurement. The dashed line is the Gaussian fitting.

5.4 Conclusions

This chapter details the study of the microfabricated Beam Profile Monitors of the IRRAD facility, featuring extra oxide layer on the top of the sensing metal and grounding of the silicon substrate. After the experimental tests, we deduced to the following findings and guidelines:

- The feasibility of measuring a reliable signal from 400 nm metal layers, was verified.

- Contribution from the silicon substrate to the total measured signal is assumed.

- The devices fabricated with Al_2O_3 coated on top of the Al did not clarify if the oxide was enhancing the SEY.

- The device with the grounded substrate recorded an inverted signal in the beginning but when the grounding was disconnected, profile measurement was obtained. A possible reason is cross-talks between the channels.

Design and fabrication of BPMs
on Kapton® substrate

<div style="text-align: right">6</div>

Although the BPM devices on Si-SiO$_2$ were already more than 200 times thinner (and less invasive) and they had shown a higher sensitivity to charged particles in comparison to the BPM devices based on the PCB technology, there was still space for improvement, as discussed in the previous Chapter. In this Chapter, the R&D was focused on thin insulating substrates (Kapton®) and two different deposition methods. The chosen layout and the fabrication techniques are described. The performance and characterization of these devices was also performed in the CLEAR facility at CERN.

6.1 Introduction

The main goal of this fabrication was to overcome the constraints of the previous devices. First and foremost, the silicon substrate needed to be replaced because it was chosen for convenience reasons due to its availability in the cleanroom. During the last experimental tests, cross-talks between channels were assumed, making it critical to improve the isolation between the sensing layer and the substrate. Lastly, the extracted signal was higher than expected possibly because of the contribution of the silicon to the measurements.
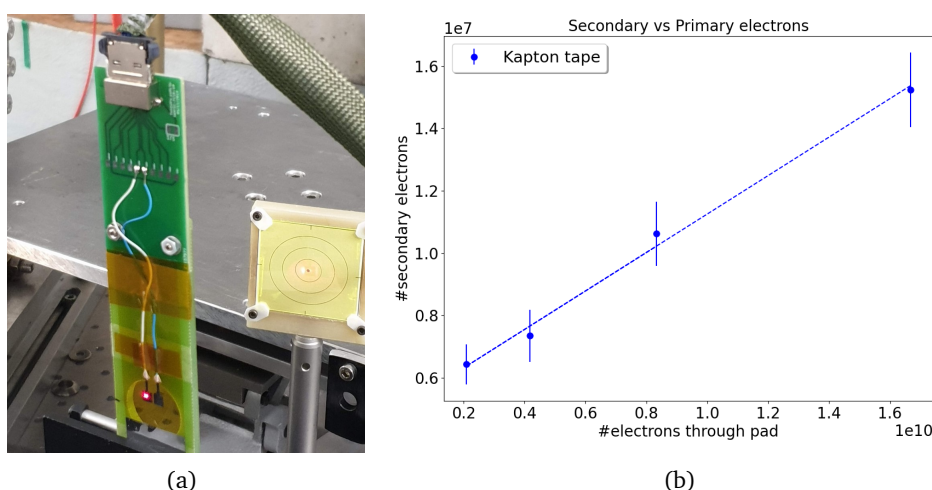

<div style="text-align: center">(a)　　　　　　　　　　　　　　(b)</div>

Fig. 6.1.: a) Pads with dimensions 4×4 mm^2 patterned on commercial Kapton® tape are mounted on the PCB-support for testing at the CLEAR facility. b) Secondary electrons as a function of the primary electrons that pass through the pad.

The deposition of aluminum on polyimide substrates was already tried during the preliminary production of BPM devices as discussed in Chapter 4 but did not result in any working prototype. However, because polyimide is highly resistive to the radiation, another trial was given. A commercial Kapton® tape (25 um) sputtered with 100 nm Al, was patterned in pads with laser and was tested in the CLEAR facility. Fig. 6.1(a) shows the pads mounted on the supporting PCB frame. The beam is pointing on the left pad of the device with the guidance of a YAG[1] screen in the background. The DAQ system recorded a remarkable signal from the metallic pads as shown in Fig. 6.1(b), encouraging the investigation on isolating substrates.

6.2 Kapton® substrate

Thermal and chemical stability, low dielectric constant, high electrical resistivity and relative ease of processing into coatings and films have made Kapton® an ideally suitable polymer for microelectronic applications such as dielectric spacing layers, protective coatings and substrates for thin metal films [40]. In addition, the possibility of getting very thin polyimide films (for e.g. up to 25 um for BPM) compared to other materials and the increased radiation tolerance, made Kapton® the most suitable possible substrate.
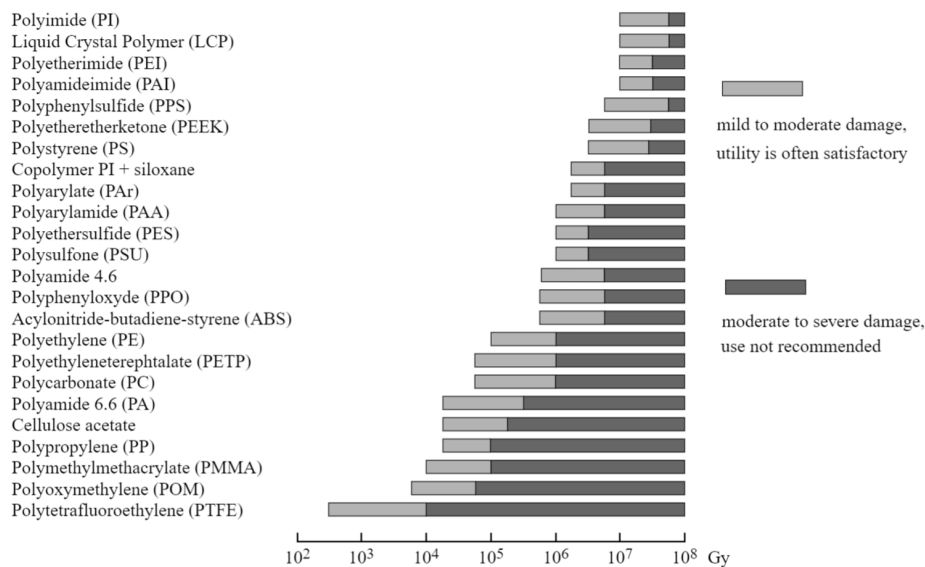
Fig. 6.2.: General classification of rigid thermoplastics with respect to their radiation resistance [41].

Fig. 6.2 presents a general classification diagram of polymers with respect to their radiation resistance, obtain by irradiation tests at CERN [41]. This guideline confirms that polyimide (or Kapton®) is the best candidate substrate. The only constraint about this material in the scope of the BPMs, is the manipulation due to its low thickness, as ungentle stretching can create dents and scratches on its surface.

---

[1]Fluorescent Screen (Cerium activated Yttrium Aluminum Garnet)

6.3 Physical Vapor Deposition (PVD)

Physical vapor deposition (PVD) is a variety of vacuum deposition techniques in which the material goes from a condensed phase to a vapor phase and then back to a thin film condensed phase. Sputtering and evaporation are the two most common PVD methods used in PV manufacturing. Among different categories of these two methods, we are interested in DC-sputtering and e-gun evaporation, which are the techniques studied and used for the BPM microfabrication.

A DC-sputtering system is composed of a chamber under vacuum with two electrodes; the anode which is positively charged and the cathode which is negatively charged. Between the electrodes, a potential difference is applied to obtain a electric field. Then, low pressure gas (Ar) is introduced in an accelerated way into the vacuum chamber which blasts the target, releasing atomic-sized particles to be deposited, which will be projected onto the substrate (Fig. 6.3(a)).
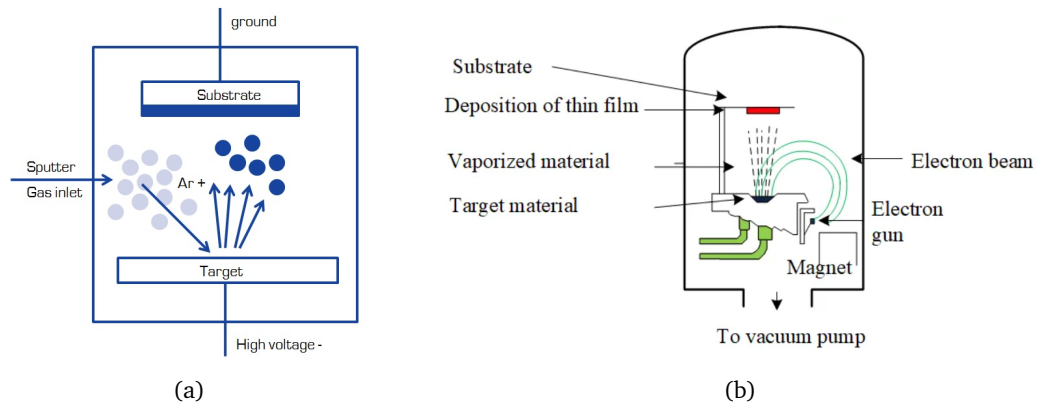

(a)   (b)

Fig. 6.3.: Schematic diagram of (a) sputtering and (b) e-gun evaporation coating methods.

E-gun evaporation process consists in evaporating a material (target) placed in a crucible heated up by a highly energetic electron beam. The evaporation source is usually a tungsten filament. The emitted electrons are accelerated to bombard the target surface. A magnetic field is applied to bend the electron trajectory, allowing the evaporation source to be positioned below the evaporation line (Fig. 6.3(b)). Both processes are good for metals and have low level of impurity.

A clear advantage of e-beam evaporation is that it permits direct transfer of energy to source during heating and is very efficient in depositing pure evaporated material to substrate. Also, deposition rate can be as low as 1 nm/min to as high as few micrometers per minute. The material utilization efficiency is high relative to sputtering and the process offers structural and morphological control of films. Additionally, coating uniformity (with planetary and masks) and precise layer monitoring techniques are also some advantages with this process [42].

6.4 Shadow mask patterning

A shadow mask is a silicon wafer with pattern features etched completely through the silicon. It is used as surface patterning technique that allows shading certain regions on the substrate and thus creating patterns on the rest. This method was developed for the microfabrication of BPM devices, as the most compatible with Kapton® substrate. The masks were fabricated in the CMi cleanroom from silicon test wafers of 100 mm diameter and 520 um thickness, double side polished. The technologies involved in the process include coating, UV exposure, development, dry etching, photoresist stripping and grinding. Fig. 6.4(a) shows the process flow, the specifications of each step and the machines used in the CMi cleanroom.

(a)
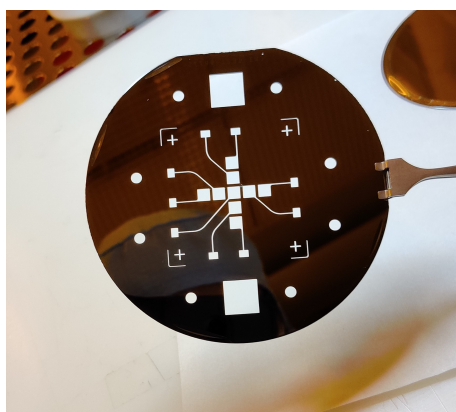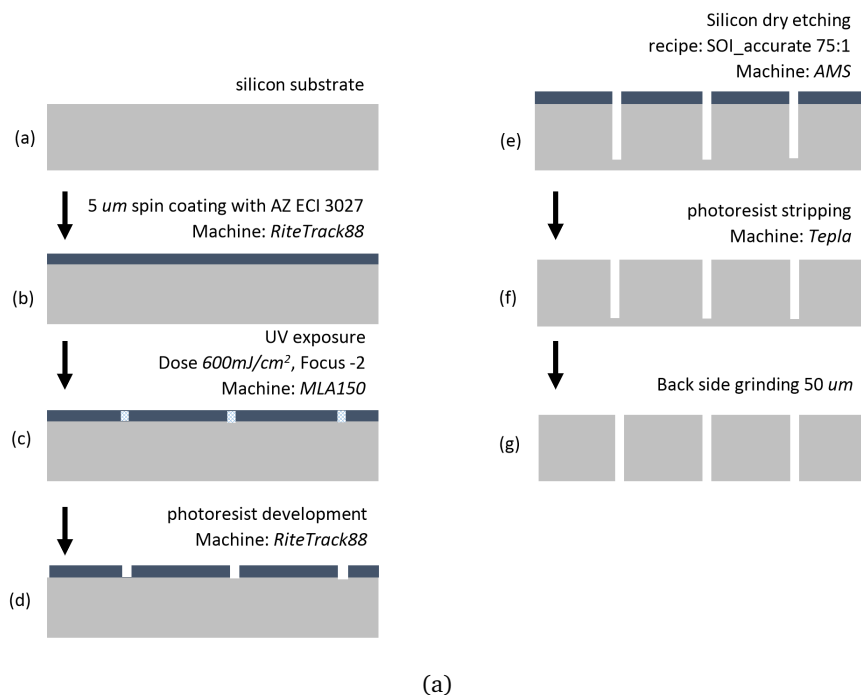
(b)　　　　　　　　　　　　　　　(c)

Fig. 6.4.: (a) Process flow of the shadow mask. Image of produced shadow masks with the layout of (a) the microBPM and (b) the connecting pads of the microBPM (backside of the mask).

Fig. 6.4(b) shows a picture of one of the produced shadow masks while Fig. 6.4(c) illustrates the mask for extra material deposition on the connecting pads of the BPM. During deposition, the Kapton® film is placed on the dummy wafer (Fig. 6.5(a)), then the mask is placed on the top of the Kapton® (Fig. 6.5(b)) and fixed with polyimide tape. Finally, the whole structure is set into a PVD chamber. After the mask is removed, only the metal pattern is left on the top of Kapton® (Fig. 6.5(c)).

(a)	(b)	(c)
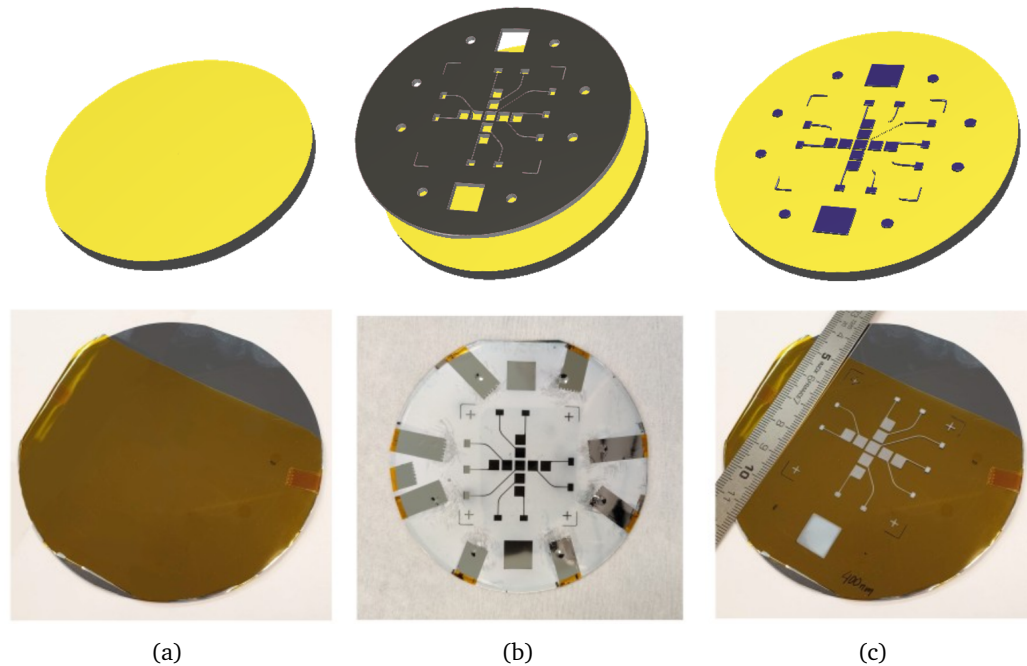
Fig. 6.5.: (a) Kapton® placed on dummy wafer and fixed with polyimide tape. (b) Mask placed on top of the Kapton® and fixed with polyimide tape.(c) Metal patterned on Kapton®. On the top is the illustration of the patterning technique.

An advantage of this technique in terms of patterning the substrate, in comparison to the direct coating which was used for older productions, is the elimination of multiple processing steps (e.g. photolithography, UV exposure, stripping, etching and cleaning), as the metal is deposited directly onto the substrate. In this way, the processing time is reduced and the adhesion of the sensing material is better as the stressing of the device is limited.

Nevertheless, there is resolution restriction like for e.g. in our case 300 um is the minimum dimension of patterned structures. The mask itself is fragile and needs careful manipulation and the alignment to previous layers is not straight forward. There is no any advanced technique to fix the mask on the substrate and the lifespan of a shadow mask is limited, as after repeated uses the holes will begin to close up as layer after layer of material builds up.

6.5 New BPMs on Kapton®

6.5.1 Old layout

The first Kapton-based microfabricated BPMs had the same layout as the preliminary devices. The shadow mask for these prototypes was fabricated from a 380 um double-side polished silicon wafer. The final grinded mask reached the thickness of 180 um because of lack of experience in mask fabrication. This resulted in a very fragile structure which broke after some uses. Fig. 6.6(a) shows the first deposition[1] of aluminum on 25 um Kapton® film with the use of shadow mask. The connecting lines are not precise and there is a distortion in the sensing pads. This can be explained by the thickness of the mask, as it was too light to keep the substrate well pressed on the dummy wafer. The second mask had the thickness of about 240 um and 50 um Kapton® was patterned, as shown in Fig. 6.6(b). The results from this deposition were already better.
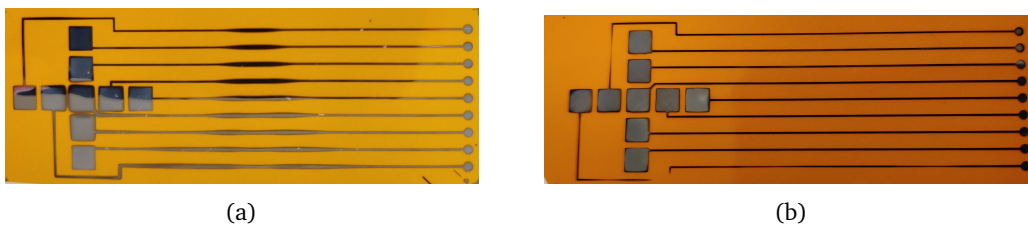

(a)   (b)

Fig. 6.6.: Deposition of 400 nm Al on (a) 25 um Kapton® (Si mask 180 um thick) and (b) on 50 um Kapton® (Si mask 240 um thick) with the old layout.

6.5.2 New layout

Brand new masks were fabricated with new layout, more compatible with the requirements of the final device. The features of the new layout include shorter but thicker routing lines (300 um instead of 200 um) for more reliable deposition. Another improvement is the enlargement of the connecting pads to simplify the electrical connection. Table 6.1 summarizes the first devices produced[1] with the new layout.

Table 6.1.: List of the first prototypes on Kapton® substrate, with the new layout.

	Kapton thickness	Pattern thickness	Pads thickness	Comments
a)	25 um	300 nm	-	Inhomogeneity
b)	25 um	100 nm	400 nm	Good
c)	25 um	-	300 nm	Burning
d)	50 um	400 nm	-	Inhomogeneity

As shown in Fig. 6.7, there were issues with the new masks, as well. First of all, there are some routing lines were the metal is either not deposited at all or its

---

[1]Deposition made by sputtering machine SPIDER600.

thickness is not the same across the lines. This is attributed to the short time of sputtering (~15 seconds) very thin layers (~100 nm). In addition, burning on the tiny structures and especially in the corners of the pads was noticed.
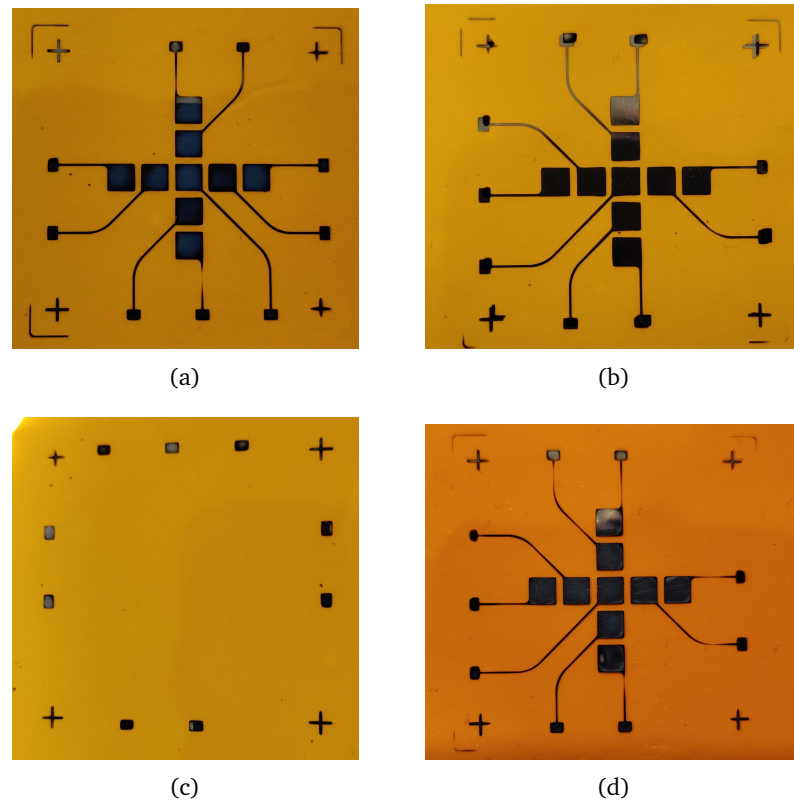
Fig. 6.7.: New microBPM layout. (a) 300 nm Al on 25 um Kapton®. (b) 100 nm Al + 400 nm Al on connecting pads. (c) 300 nm Al pads (d) 400 nm Al on 50 um Kapton®.

Fig. 6.7(b) shows a device with 400 nm Al deposited with the main BPM mask and an additional layer of 400 nm added only on the connecting pads with a second mask. Other than the misalignment between the pads, the color of the pads indicates burning. This defect is attributed to be due to the high deposition power (2000 W).

6.6 Characterization of the new BPMs

This section describes the tests performed to access the Secondary Electron Yield of different thicknesses of metal with or without oxide in vacuum, the adhesion of the metallic layers to the Kapton® substrate treated with different techniques, the homogeneity of the metal deposition, the electrical connections and the coating machines. The knowledge acquired from these tests, combined with the performance tests of the BPM devices in the CLEAR facility revealed the improvements that were implemented in the final version of the devices.

6.6.1 Secondary Emission Yield measurements in vacuum

The Secondary Electron Yield (SEY) for different primary electron energies was measured[1] on different samples with dimensions 10×10 mm^2. The maximum applied dose to measure one spectrum was about 1.5×10^{-7}C. The purpose of these measurements was to understand which thickness of metallic layer with or without oxide gives the best SEY.
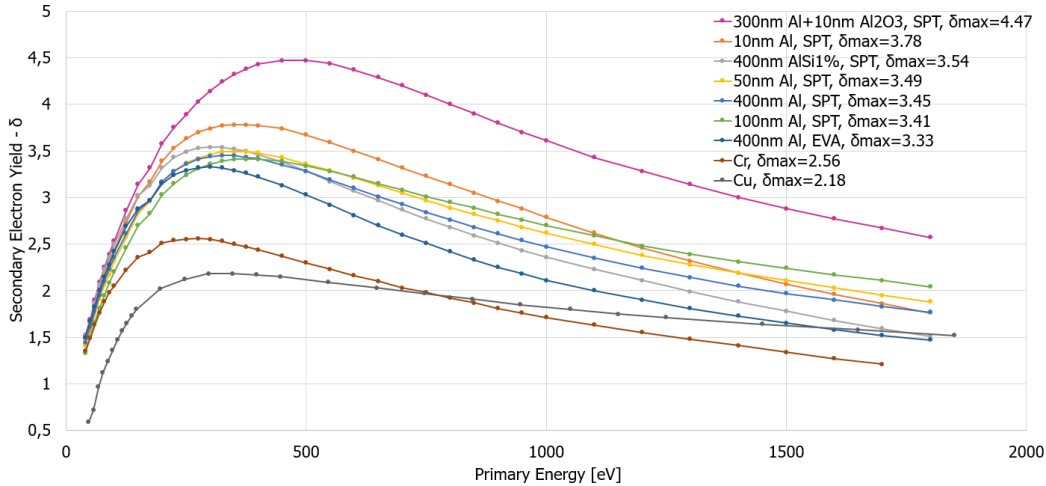

Fig. 6.8.: Experimental SEY spectra of different thicknesses of aluminum (on Kapton® substrate), chromium and copper.

Fig. 6.8 shows the measured SEY spectra in vacuum from the different samples. The Aluminum was either deposited on 25 um Kapton® by sputtering (SPT) or by evaporation (EVA) while the Chromium sample was laminated on a 50 um Kapton® with the standard PCB technology. The SEY spectrum of Copper was retrieved from the database. As it can be seen, the Copper used as sensing material in the old BPM devices had the lowest yield as was expected also from the theory [31]. Chromium was chosen to be studied because of its high irradiation resistance and its availability in the CERN workshops. The yield $\delta_{max(Cr)}$=2.6 is higher than copper but still not as high as needed. Aluminum proved to be the most sensitive material with maximum yield $\delta_{max(Al)}$=3.78. Although, that sample was the thinnest, only 10 nm, so most possibly there was a contribution from the Kapton® substrate to the total signal. The rest of the aluminum samples, sputtered either evaporated, showed a more reasonably high yield and with agreement to the theoretical values [43]. SEY of Aluminum in vacuum is independent of the thickness of the metal, especially at increasing primary particle energy.

Aluminum doped with 1% of silicon was tested as a SE emitter, in order to examine if on such structure the electrical connection can be accomplished using wire-bonding techniques (as with pure aluminum it is not possible). The results shown that the

---

[1]Measurements conducted by the CERN Surface Analysis department (TE-VSC-SCC)[31].

yield is independent from the silicon doping and comparable to pure Aluminum. In the attempt to increase the SEY, one of the samples was covered with an extra Al_2O_3 layer. This sample showed a 23% enhancement in the yield. It is important to state that the tests were performed in a vacuum chamber and bombardment by low energy electrons.

6.6.2 Cross-hatch adhesion test

Parameters that influence the adhesion between two materials are stresses that have been applied on the substrate, contamination, chemical bonding between the molecules, the physical properties and the roughness of the substrate. In order to make a reliable deposition, it is essential to remove organic contaminants, dust and fingerprints from the substrate and prepare it properly by adhesion treatment. The adhesion is characterized by mechanical tests[40].

Oxygen plasma treatment is widely used for adhesion improvement. More specifically, it reduces the native oxide percentage in the case of a metal, cleans the surface from organic contaminants and modifies the surface topography to promote the cross-bonding of the molecules of the coating layer. Deposition of titanium or chromium as sticking layer is another, widely applied technique. Both Ti and Cr share the property of adhering well onto polymeric substrates, they do not alter the properties of the device that is about to be fabricated and they help to promote the nucleation of the next deposited material which might not otherwise stick.

In the current study, different deposition recipes have been tested with the sputtering machines SPIDER600 [44] and DP650 [45], and the evaporating tool EVA760 [46], all available in the CMi cleanroom. The recipes are described in the following:

SPIDER600 - DC sputtering system

- EO_2-Ti-Al: some seconds of oxygen plasma treatment and then deposition of 10 nm titanium layer (13 sec) under the power of 2000 W.
- Ti-Al: same as above but without the oxygen plasma treatment.
- EO_2-Al: same with the first recipe but without titanium layer.
- Ti(1)_Al200W_EO_{2-1}: same as the first recipe but under the power of 200 W.

DP650 - DC sputtering system

- Ti-Al: some seconds of titanium sputtering before the deposition of aluminum under 200 W.

- Cr-Al: same as above with chromium instead of titanium as adhesion layer.

EVA760 e-beam evaporator

- 450[O_2]Al_50: oxygen plasma treatment followed by aluminum deposition in the substrate holder No 450.

All the trials were performed in the same loading of the sample in the machine in order to avoid the contamination of the samples. Kapton® substrate was provided by the CMi in the thickness of 25 um, 50 um and 180 um [47].

In order to determine the adhesion quality of the above deposition recipes, a cross-hatch tape test was conducted using pressure-sensitive tape. A pattern was created on the metallic surface using a crosshatch cutter with preset blades, helping to ensure that incisions are parallel to each other and properly spaced. After the tape had been applied and peeled off, the area was examined and rated. In Fig. 6.10, on the left is the image of the aluminum after making the pattern with the crosshatch cutter while on the right is the back side of the peeled tape.
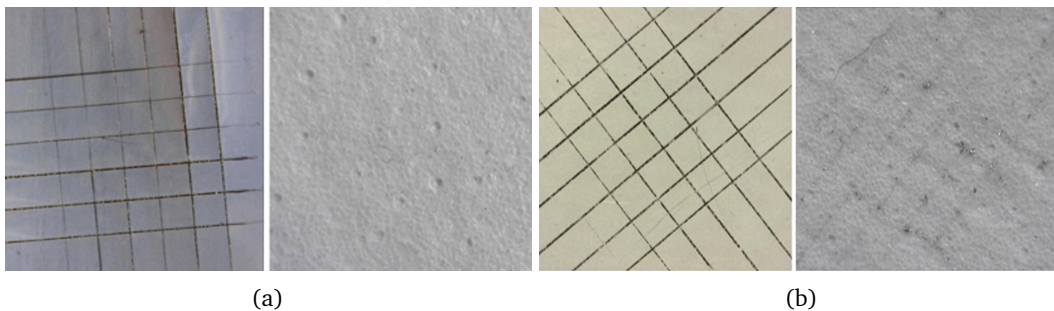

(a)   (b)

Fig. 6.9.: Deposition of Al on (a) 25 um Kapton® with the plasma-Ti-Al recipe and (b) 180 um Kapton® treated with the Ti-Al recipe. The images on the left correspond to patterning made with the cross-hatch cutter and on the right is the back side of the peeled tape.

An example of a good adhesion with 5B rating (classification table in Appendix D), is shown in Fig. 6.9(a), as there are no traces of aluminum on the peeled tape. A bad adhesion (3B) is shown in Fig. 6.9(b), with part of the aluminum left on the tape after the peeling.

Table 6.2 summarizes the results after the rating of all the samples coated with aluminum in the different systems; SPIDER600, DP650 and EVA760. The best adhesion was obtained with the thinnest Kapton® substrate and SPIDER600 machine while both evaporated samples (150 nm and 100 nm aluminum on 25 um Kapton®) showed excellent adhesion. Detailed results from the cross-hatch test can be found in Appendix D.4.

Table 6.2.: Evaluation of metal adhesion to Kapton with cross-hatch test.

SPIDER:

Recipe	Kapton	Classif.
EO_2-Ti-Al	180 um	4B
	50 um	5B
	25 um	5B
Ti-Al	180 um	3B
	50 um	5B
	25 um	5B
EO_2-Al	180 um	3B
	50 um	4B
	25 um	5B

DP650:

Recipe	Kapton	Classif.
Ti-Al	180 um	3B
	50 um	4B
	25 um	4B
Cr-Al	180 um	3B
	50 um	3B
	25 um	5B

EVA760:

Recipe	Aluminum	Classif.
$450[O_2]Al_50$	150 nm	5B
	100 nm	5B

6.6.3 SEM-FIB analysis

In order to cross-check the metal thickness of the samples fabricated at CMi and evaluate them for surface fractures, flaws, contaminants, corrosion and inhomogeneity, high-resolution imaging by FIB-SEM[1] was performed [48]. The FIB (Ga+) interacts with the specimen surface producing various signals that can be used to obtain information about the surface topography and composition (Fig. 6.10(a)). The SEM scans the surface to collect the secondary electrons that are produced and create the topography (Fig. 6.10(b)).
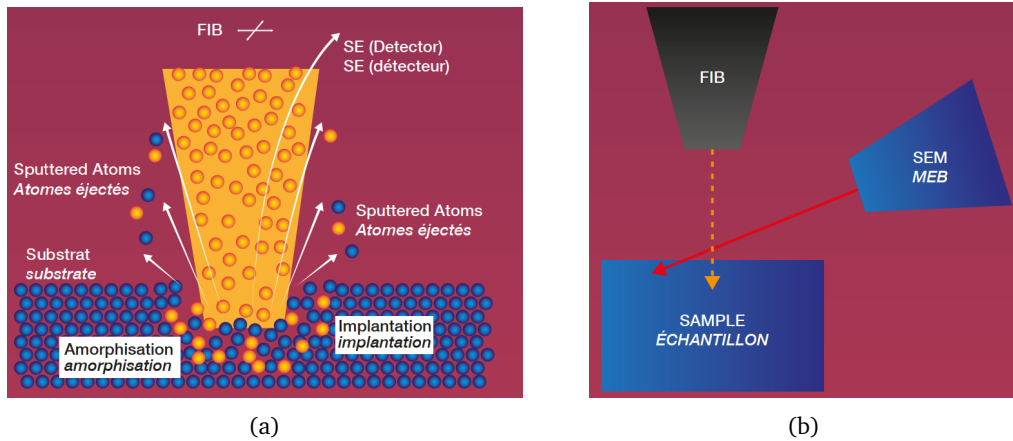

(a)	(b)

Fig. 6.10.: (a) FIB interaction with the specimen surface to produce secondary electrons. (b) SEM scans the surface and creates an image by collecting the SE.

Fig. 6.11(a) shows an image taken during SEM analysis on 400 nm sputtered sample. For this specific sample, there is an error of about 5% in the deposition. Platinum gas is deposited on the specimen before the ion-beam milling in order to ensure a better measuring without destroying the sample under test. On the other hand, Fig. 6.11(b) illustrates the imaged obtained with SEM of the 400 nm evaporated

---

[1]FIB stands for Focused Ion Beam and SEM derives from Scanning Electron Microscope

sample. The surface is more homogeneous and the deviation between the measured and the expected thickness is only 0.5%.
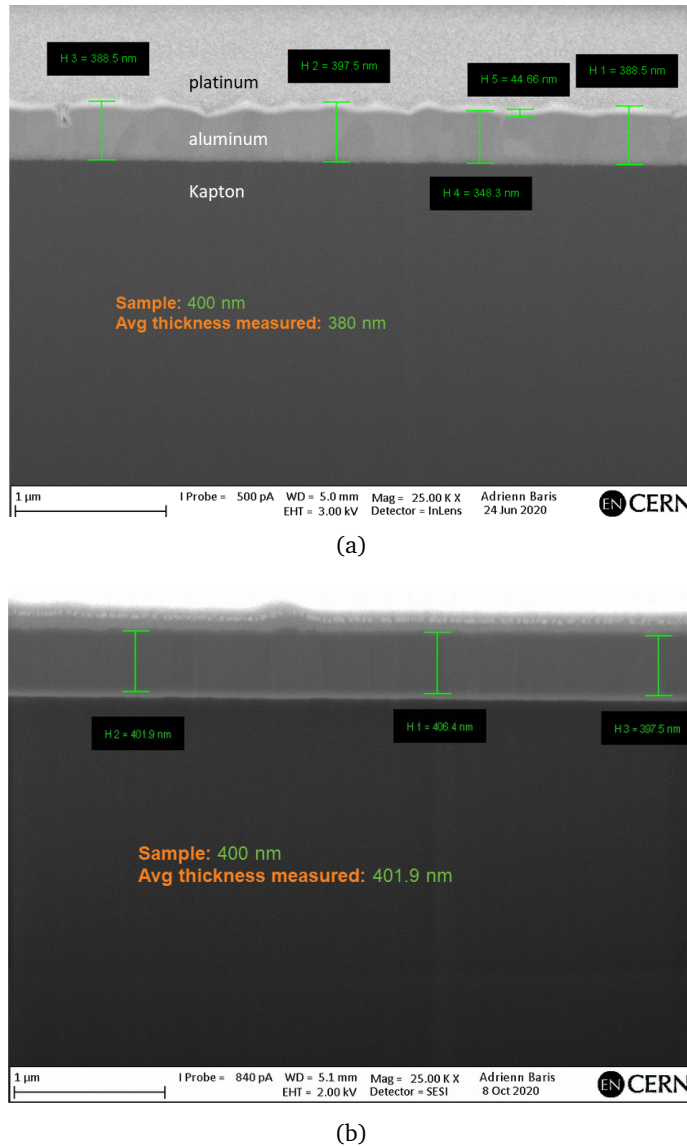

(a)

(b)

Fig. 6.11.: Measurement done with the help of SEM ; (a) 400 nm sample deposited by sputtering and (b) 400 nm sample deposited by evaporation.

Table 6.3 and Table 6.4 summarize the results[2] of the analysis and the indicated (nominal) metal thicknesses obtained with the available coating machines are compared with the FIB-SEM measurements. The obtained values showed that the sputtering tool is not suitable for very thin layers (down to 10 nm) because of high deposition error ∼390% (see last column of Table 6.3). The average error for sputtering was ∼20%. E-gun evaporation was proven to be more precise technique with about 3% deposition error.

---

[2]Measurements conducted by the CERN Engineering department (EN-MME) [48].
[2]Deposited by Atomic Layer Deposition tool named BENEQ TFS200 (ALD 2) in CMi cleanroom.

Table 6.3.: Comparison between the nominal Al thickness sputtered by SPIDER600 and the measured thickness by FIB-SEM method.

Nominal Al thickness + Al$_2$O$_3$[2] [nm]	Deposition power [W]	Measured thickness [nm]	Al deposition time [sec]	Error [%]
400	200	380	706	5
300 + 10	200	166 + 17	529	40
100	200	122	177	22
100	2000	80	13	20
100 (commercial tape)	-	88	-	12
50	200	52	89	4
10	200	49	18	390

Table 6.4.: Comparison between the nominal Al thickness evaporated by EVA760 and the measured thickness by FIB-SEM method.

Nominal Al thickness [nm]	Measured thickness [nm]	Error [%]
400	401.9	0.47
300	282.9	5.7
150	145.9	2.7
100	104.2	4.2

6.6.4 Electrical connection

The first microfabricated BPM device that was fully functional was connected to the readout PCB by wire bonding and to the DAQ system with the SAMTEC connectors (see Chapter 4). Wire-bonding is a solid phase welding process, where the two metallic materials (wire and pad surface) are brought into intimate contact. The same technique was examined for the new Kapton-based devices.

Aluminum doped with 1% of silicon was sputtered in 400 nm and 800 nm on 25 um Kapton® in order to test wire-bonding on more rigid surfaces. After the tests, none of the samples had a successful electrical connection, as the wire was detaching from the side of the metallised Kapton®. Fig. 6.12(a) shows a connection made by breaking the wire on the side of the Kapton® and attaching it to metallised Kapton® with conductive glue. This process is time consuming and expensive, so the final devices were assembled by using copper wire tinned (TCW 35 1230989), with 10 mm length for each pad. The connection was done using silver conductive paint (SPI#05002-GA) on the Kapton® side and standard Sn on the PCB side. Fig. 6.12(b)) shows the readout PCB that was designed to host the intermediate electrical connections between the new flexible sensor and the DAQ system. Fig. 6.12(c) shows a BPM detector electrical connected to the readout PCB. In the view of a larger scale production, the composition of the connecting pads needs to be improved for direct wire-bonding.
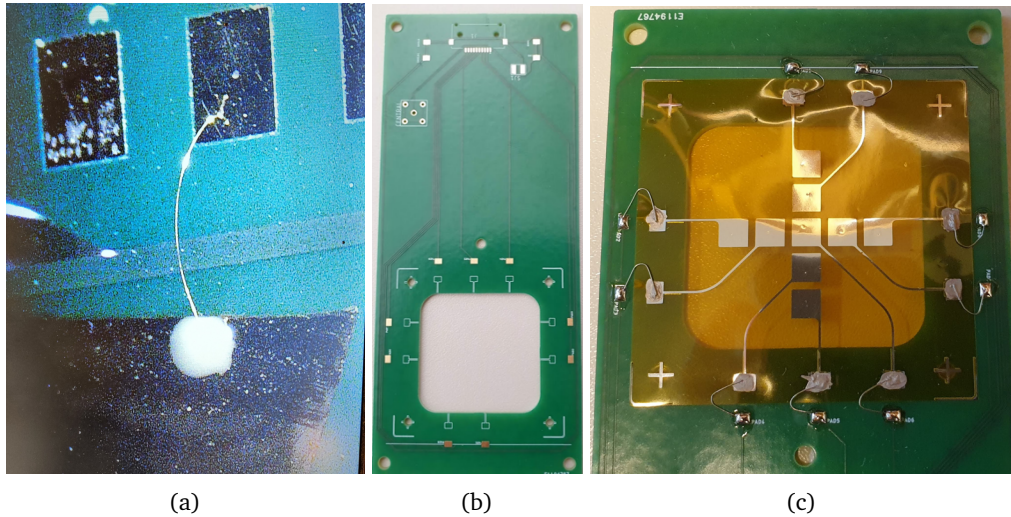
(a)　　　　　　　　(b)　　　　　　　　(c)

Fig. 6.12.: (a) After successful bonding on the side of the PCB the wire is attached to the conductive glue which is applied on metallised Kapton®. (b) PCB frame designed to support the new flexible BPM devices and host the electrical connection. (c) Copper wires connecting electrically the pads of the BPM with the readout PCB.

6.6.5 Reproducibility

To launch a massive production for the BPM detectors, the most suitable coating system should have been selected. As already mentioned, three aluminum deposition tools were used during this R&D, each one with different benefits and constraints. A comparison among these tools is presented in Table 6.5.

Table 6.5.: Deposition tools tested for the massive BPM production.

	SPIDER600[44]	DP650[45]	EVA760[46]
Machine type	cluster system	single chamber multi-target	e-gun evaporator
Deposition technique	DC Sputtering	DC Sputtering	Evaporation
Wafer capacity	25 per loading (processed in parallel)	one-by-one loading	8 per loading (all processed in the same time)
Deposition rate [nm/sec]	1.77	5.3	0.5
Avg uniformity	5%	8.1%	2.8%
Resistivity	$7.06*10^{-2}$ Ω/square	$\sim$4.88 [$\mu\Omega$.cm]	$\sim$3.74 [$\mu\Omega$.cm]

SPIDER600 is a DC-sputtering cluster system and can process 20 samples per loading (one-by-one). The deposition chamber of this system is under vacuum and the pumping time is around 10 min. In this way, pumping time for 19 wafers is saved.

DP650 is a DC-sputtering single chamber multi-target and it proceeds the wafers one-by-one which means that a pumping time precedes and follows each deposition. The difference in the deposition rate between these two machines is due to the size of the targets. EVA760 is an e-gun evaporator and needs approximately 1 hour of pumping. Nevertheless,eight wafers can be loaded in the same run. To take full advantage of the evaporator, eight shadow masks are needed for parallel productions. In comparison with the other machines, EVA750 has the lowest deposition rate and resistivity, although the best uniformity.
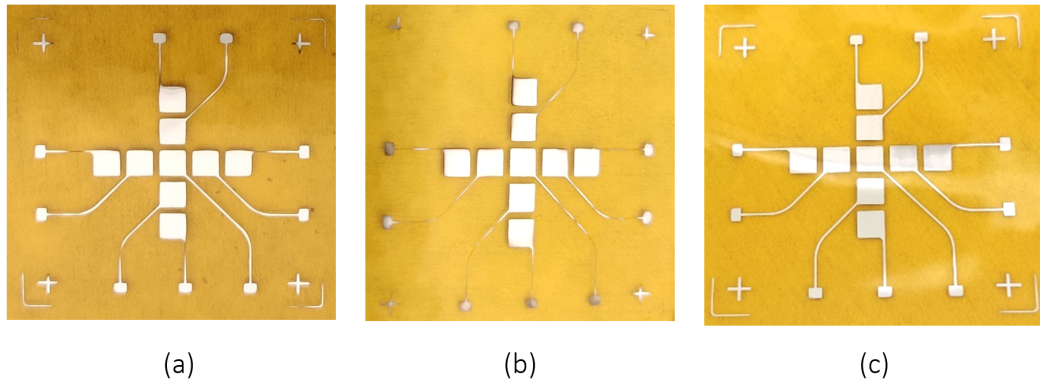

(a)   (b)   (c)

Fig. 6.13.: 100 nm Al deposited by the three different machines: (a) SPIDER600, (b) DP650, (c) EVA760.

Fig. 6.13 shows BPMs produced in the different tools. SPIDER600 performed a good deposition in the beginning (Fig. 6.13(a)) but when the production rate was increased most of the devices had burning signs and inhomogeneity. In the attempt to overcome this obstacle, DP650 was tested providing devices with similar issues (Fig. 6.13(b)). Finally, the EVA760 evaporator provided the best coating results, as shown in Fig. 6.13(c). Apart from this, another benefit of the EVA760 system is the low deposition error according to the FIB-SEM analysis (see section 6.6.3).

6.7 Irradiation tests in the CLEAR facility

The performance of the Kapton-based BPMs was evaluated with 200 MeV electron beam in the CLEAR facility at CERN. All the devices were irradiated gradually with beam charges 0.4 nC, 0.8 nC, 1.3 nC, 3 nC and 6 nC at 0.8 Hz and $\sigma_{beam} = 0.6\ mm$, in order to verify the linearity of the response and determine the SEY.

6.7.1 First sputtered device, Kapton® tape and Cr device

The first experimental run was held in THz focused beam test-stand with three devices mounted for testing:

- 100 nm Al on 25 um Kapton® (uBPM4-PI: Commercial tape)

- 400 nm Al SPT[1] on 25 um Kapton® (uBPM1-PI: EPFL CMi)

- 10 nm Cr, 5 um Cu on 50 um Kapton® (uBPM2-PI-Cr: CERN MPT Workshop)

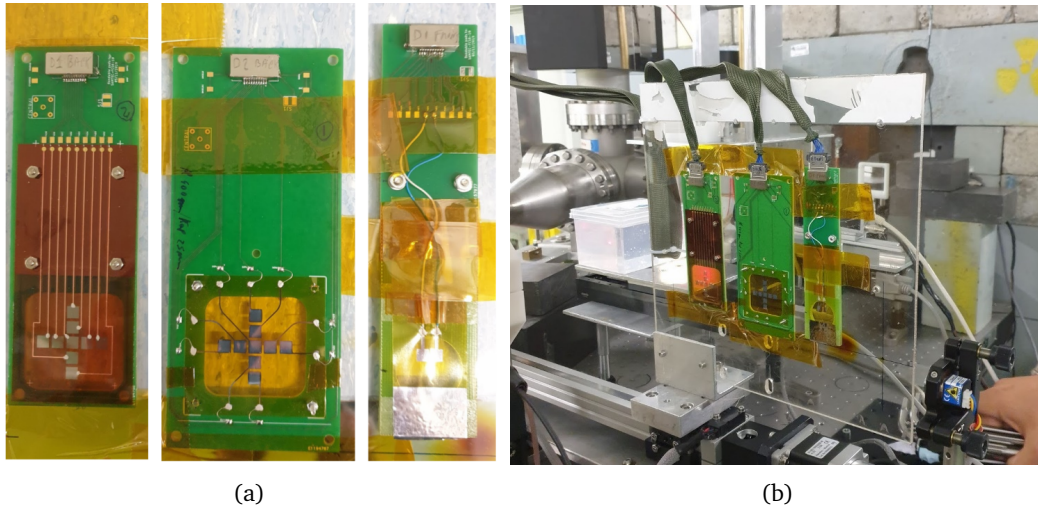(a)   (b)

Fig. 6.14.: Devices mounted on PCBs: (a) uBPM2-PI-Cr (left), uBPM1-PI (middle) and commercial uBPM4-PI(right). (b) Installation setup in the THz.

Fig. 6.14(a) shows the devices connected to the PCBs. The uBPM4-PI is a commercial tape. This device is used as reference to the new BPMs. The uBPM2-PI-Cr was fabricated in the CERN MPT Workshop, where the old BPMs based on PCB-technology were being fabricated. Fig. 6.14(b) shows the installation setup in the THz.
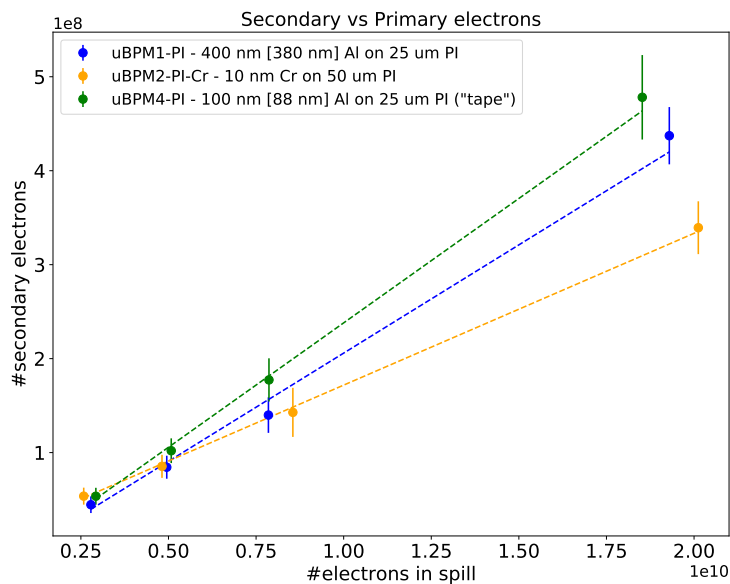

Fig. 6.15.: Number of secondary electrons as a function of the electrons in spills for the test performed for uBPM4-PI, uBPM1-PI and uBPM2-PI-Cr.

---

[1]SPT stands for sputtering.
[2]The same device described in section 6.1.

The beam had defocusing and diverging issues (Appendix E.1). The experimental run showed that there is no linearity towards higher electron impinging energies and the SEY was much higher than expected. Fig. 6.15 shows the Secondary Electrons as a function of the electrons in spill without taking into account the highest irradiating charge. The device with Cr is well below the Al devices and the thinner Al device (100 nm) has the highest yield. Thus, chromium was excluded from the list of sensing material candidates.

6.7.2 Sputtered devices with and without Al_2O_3

During the second experimental run, three devices produced with sputtering, were tested:

- 400 nm Al + 10 nm Al_2O_3 SPT on 25um Kapton[®] (uBPM5-PI)

- 300 nm Al + 10 nm Al_2O_3 SPT on 25um Kapton[®] (uBPM6-PI)

- 300 nm Al SPT on 25 um Kapton[®] (uBPM7-PI)

Fig. 6.20 shows the devices installed in the THz. The BPMs are mounted on the dedicated PCBs and attached to a Plexiglas support. The support, in turn, is mounted to a motorized stage which allows positioning the devices under the beam spot. The beam had defocusing and diverging issues, as on the first test (Appendix E.2). Thus, there was no linearity towards higher electron impinging energies and the SEY was, again, was higher than expected.
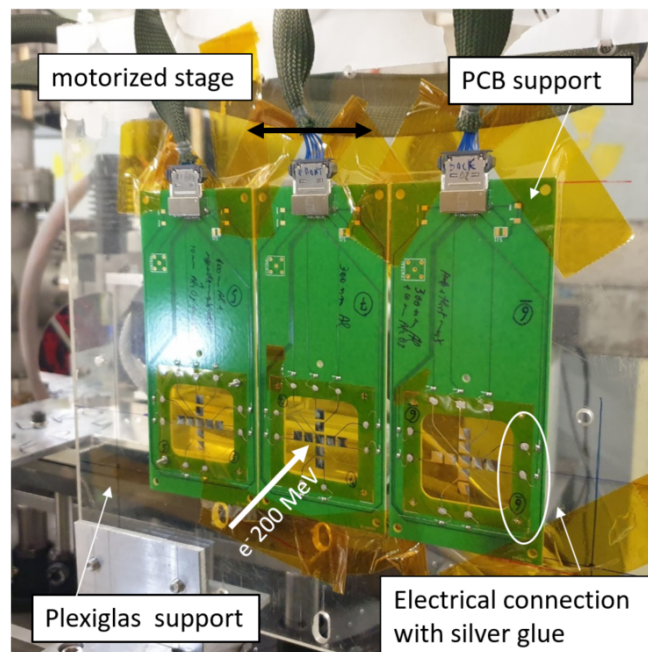

Fig. 6.16.: BPMs mounted in the beam line for the irradiation test: uBPM5-PI (left), uBPM7-PI (middle) and uBPM6-PI (right).

Fig. 6.17 shows the secondary electrons as a function of the electrons in spills for all the devices from the first two irradiation runs. The highest charge is not taken into account. The device with the Cr is well below all the Al devices and among the Al devices with or without Al_2O_3 the difference of the SEY is below 1%, so there is no substantial difference among them.
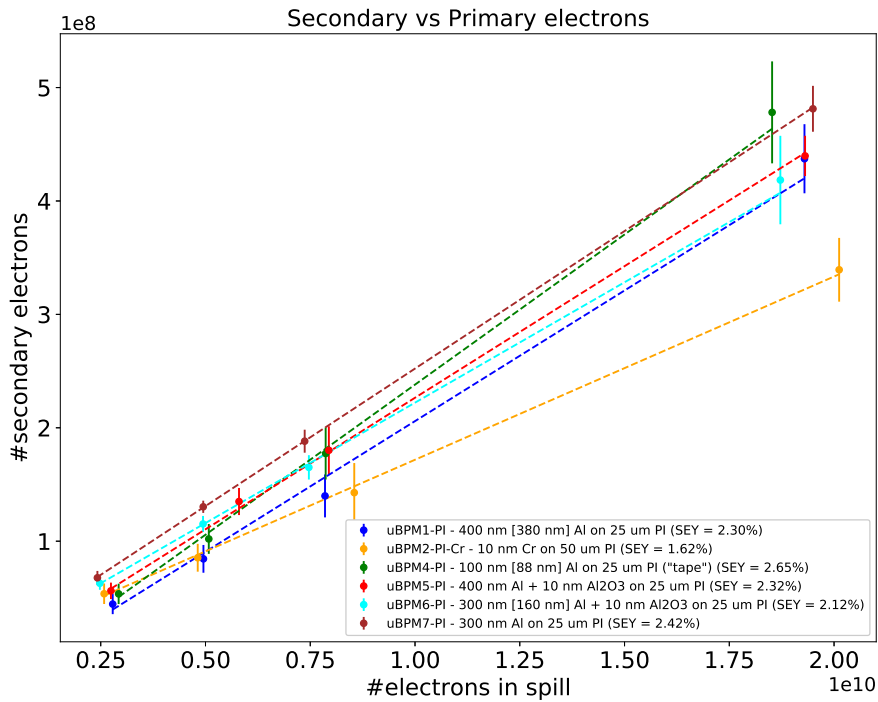

Fig. 6.17.: Number of secondary electrons as a function of the electrons in spills for all devices from the first two tests.

6.7.3 $11{\times}11$ mm^2 pads

During the third irradiation test, six $11{\times}11$ mm^2 pads were tested in order to compensate for the problems of the beam defocusing and diverging as was the case on the previous two tests. The samples are listed below:

- 100 nm Al SPT on 25um Kapton$^®$ (uBPM8-PI-ref4)

- 100 nm Al + 10 nm Al_2O_3 SPT on 25um Kapton$^®$ (uBPM8-PI)

- 300 nm Al SPT on 25um Kapton$^®$ (uBPM9-PI-ref7)

- 300 nm Al + 10 nm Al_2O_3 SPT on 25um Kapton$^®$ (uBPM9-PI-ref6)

- 400nm Al SPT on 25um Kapton$^®$ (uBPM10-PI)

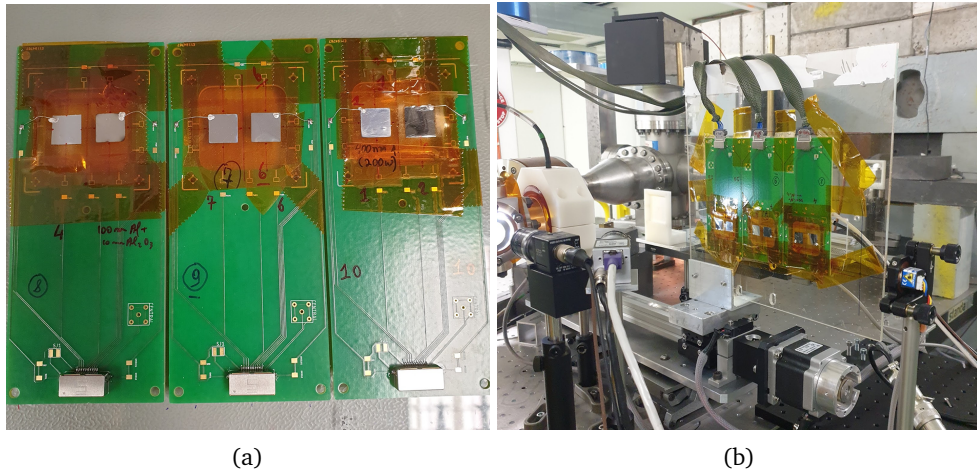- 10nm Cr + 5 um Cu on 50um Kapton$^®$ (uBPM10-PI-ref2)

Fig. 6.18.: (a) Testing pads mounted on the readout PCB. (b) Installation setup in the THz.

Fig. 6.18(a) shows the pads connected to the PCBs while Fig. 6.18(b) depicts the irradiation setup in the THz. The beam conditions were better with respect to the previous tests (Appendix E.3). For the samples uBPM9-ref4, uBPM10 and uBPM10-ref2 the beam was defocusing and diverging during the scans, but the displacement of the beam origin as well as the sigma of the beam in x-y direction are below 1 mm thus the beam stayed within the 11×11 mm^2 pads. For the other samples there were a few glitches during some scans. The data acquired from the pads during these conditions are discarded or taken into account when the glitches are below a certain threshold that does not exceed the dimensions of the pads.
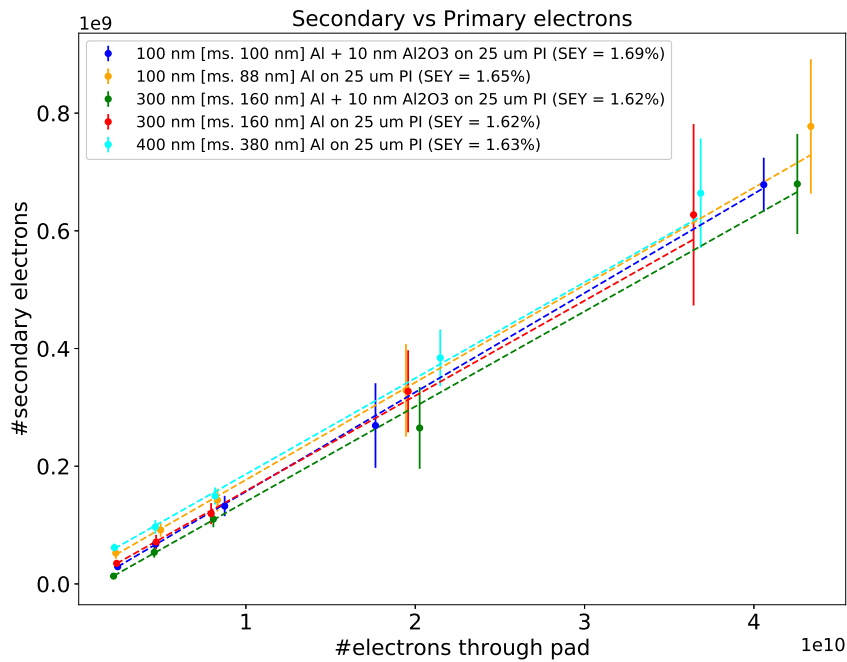

Fig. 6.19.: Number of SE as a function of the electrons passing though the pads. On the caption the metal thickness as extracted from the FIB-SEM analysis are indicated.

Fig. 6.19 shows the number of SE as a function of the primary electrons passing though the pads. At higher impinging electron beam the error bars are higher due to the non stable beam current (Appendix E.3. The difference of the SEY values among all tested devices are much less than 1%, thus the devices with the Al_2O_3 do not perform better than those without this coating.

6.7.4 First evaporated devices

During the forth irradiation test, the first batch of evaporated devices was tested. The devices are listed below:

- 100 nm Al EVA[1] on 25um Kapton® (uBPM11-PI)
- 300 nm Al EVA on 25um Kapton® (uBPM12-PI)
- 400 nm Al EVA on 25um Kapton® (uBPM13-PI)
- 6 Cu layers staggered (old miniBPM)

A miniBPM was also mounted on the back side of the uBPM11-PI for comparison. Two different type of tests were performed: one broad beam scan (at ∼0.4, 0.8, 1.3, 3 and 6 nC) for all the devices in order to evaluate the profile of the devices fabricated with the new technique (evaporation), as well as a focused beam scan but only for the pair uBPM11-PI and miniBPM at primary electron charges ∼0.4, 0.8, 1.3, 3, 6, 8 and 10 nC. Fig. 6.20 shows the setup for the broad beam scan downstream of the beam line close to the wall.
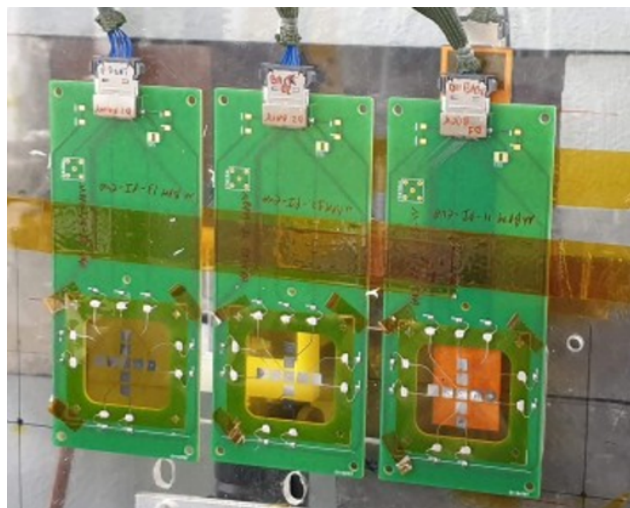

Fig. 6.20.: Setup for the broad beam scan in the VESPER (downsteam of the beam line close to the wall).

A comparison of the secondary electrons as a function of the primary for the broad beam scan is shown in Fig. 6.21. Among the evaporated devices the 100 nm one has much lower signal in comparison with the 300 nm and the 400 nm devices.

---

[1] EVA stands for Evaporation.
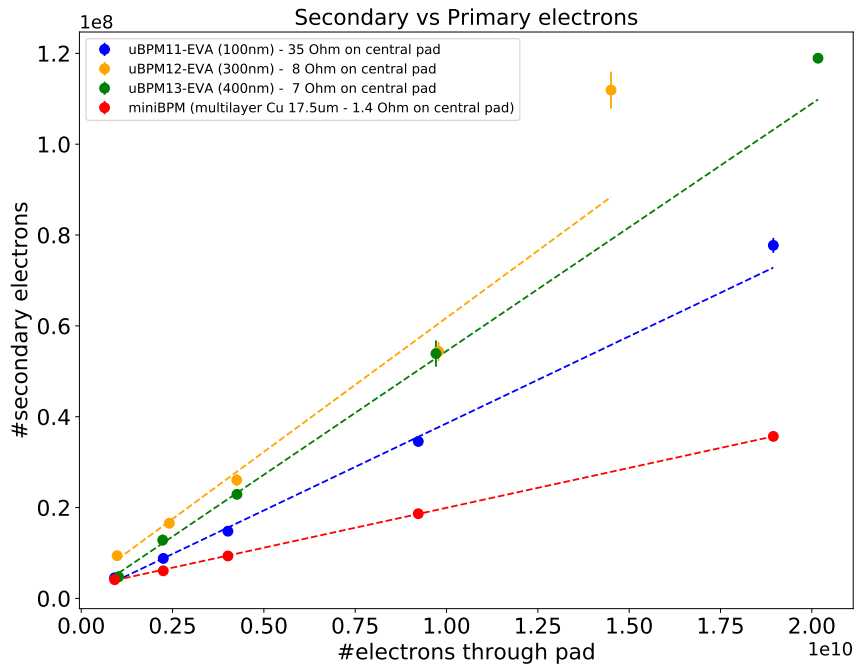
Fig. 6.21.: Secondary electrons as a function of the primary electrons for the broad scan for all the devices. The resistance of the central pads for all the devices is also indicated in the caption.

Fig. 6.22 shows an image of the beam recorded by a YAG-screen, when it was focused on the central pad of miniBPM and uBPM13, during the test.

(a)   (b)

Fig. 6.22.: (a) Electron beam focused on the central pad of (a) the miniBPM and (b) the uBPM13 in THz.

Fig. 6.23 shows the profiles reconstructed from the beam parameters and the voltages per pad for all the tested devices. As it can be seen the signal of the miniBPM is lower than the new evaporated BPMs.
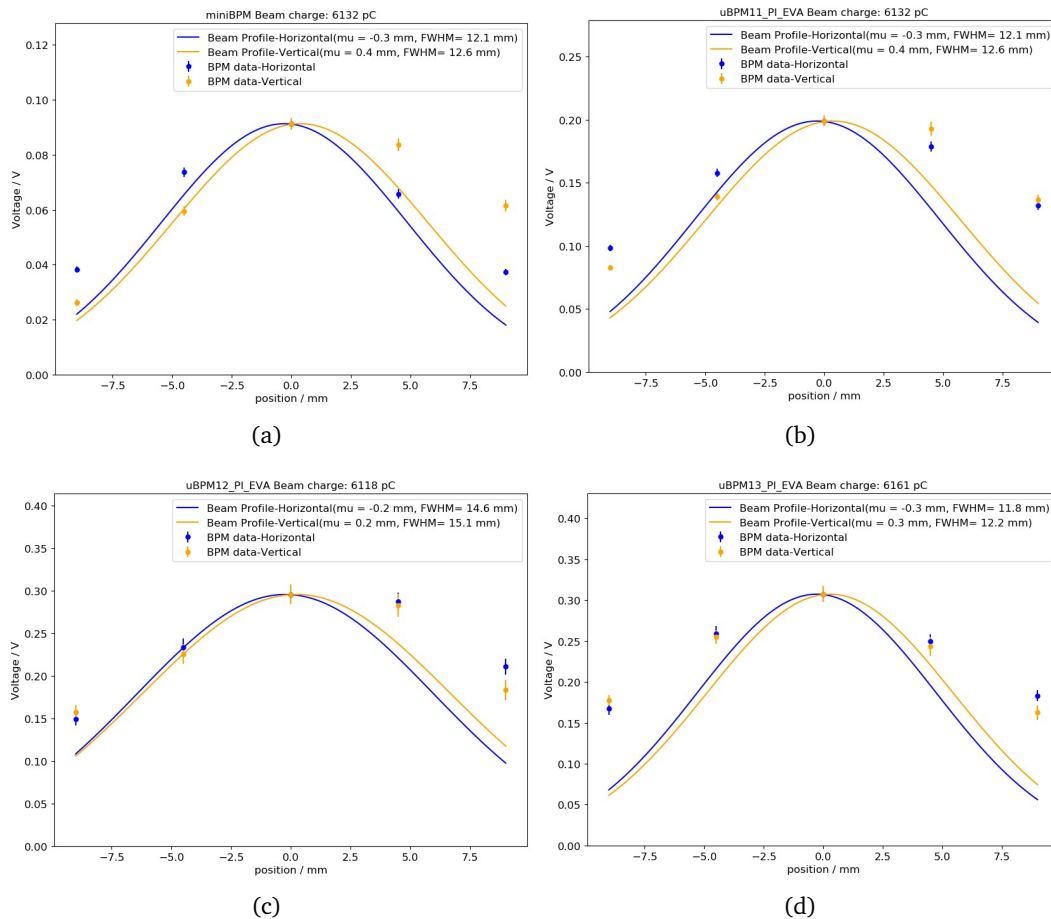
Fig. 6.23.: Comparison between the profiles obtain at 6 nC in VESPER broad beam with (a) miniBPM, (b) uBPM11, (c) uBPM12 and (d) uBPM13.

6.7.5 Summary of the irradiation tests
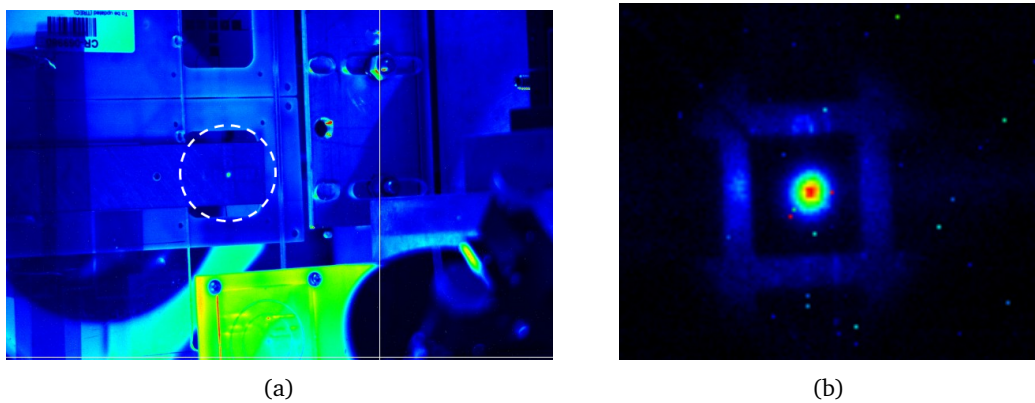
Fig. 6.24 shows the measured secondary electrons as function of the primary energy of the impinging particles for BPM devices with different characteristics. The sputtered monitors, independently from the aluminum thickness in the range of 100 nm to 400 nm (thinner layers were studied in the laboratory but showed unexpected SEY and metal non-uniformity, so were not irradiated) nor the additional Al_2O_3 layer, measured a yield of ~1.63%.

The evaporated microBPMs recorded a slightly increased SEY around 1.88% while the old miniBPM had the worst performance about 1.54%. The obtained yield is in very good agreement with the values in SEY evaluation plot (for comparison see Fig. 6.8) when extrapolating them to hundreds of MeV primary particle energy.

Fig. 6.24.: Experimental SEY from sputtered and evaporated microBPMs and miniBPM. The substrate is 25 um Kapton®. On the caption the dimensions of the samples as extracted from the FIB-SEM analysi sare indicated.
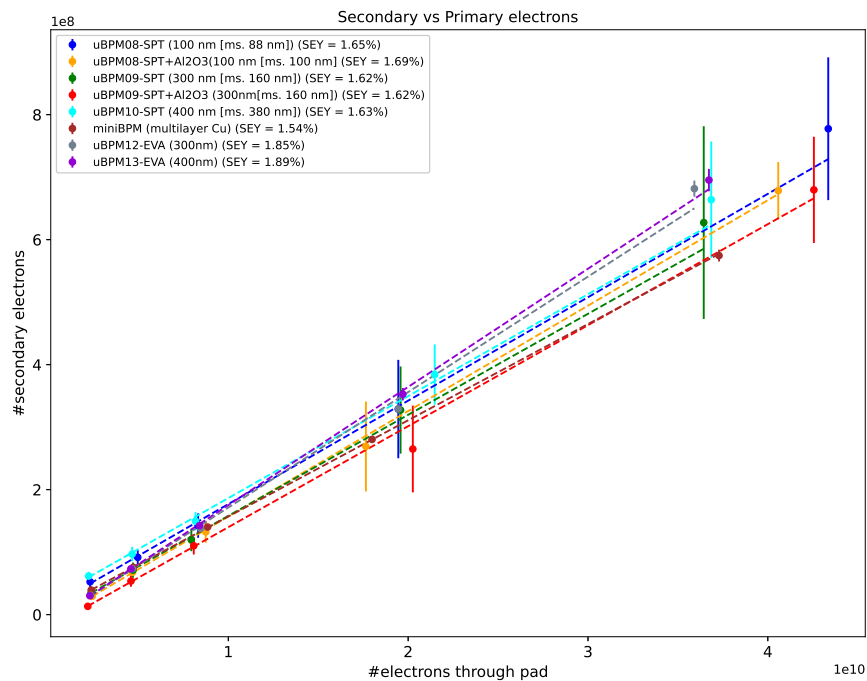
6.8 Conclusions

New BPM devices were microfabricated at CMi in EPFL with different deposition methods, characterized and evaluated for their performance. The conclusion from these studies are summarized below:

- Kapton® was chosen as a substrate because of its thermal and chemical stability, its low dielectric constant and high electrical resistivity, its transparency to the impinging beams and the increased radiation tolerance and the fact that gives the possibility to manufacture BPM devices on very thin substrates (much thinner than the standard PCB substrates).

- Aluminum was chosen as sensing material because of its availability, low cost and higher SEY compared to copper.

- SEY of Aluminum in vacuum is independent of the thickness of the metal. Same measurements performed in air with 200 MeV electrons have shown the same behaviour but with lower SEY at 1.6%.

- BPM devices coated with 10 nm Al_2O_3 have shown a 23% increase of the SEY in vacuum with respect to the devices from pure Al. However, this was not

the case when the same devices were tested in air. As the BPM devices will be operated in air in the IRRAD facility, coating with oxide was not chosen for the final production of the devices.

- From the deposition methods with the use of a mask, the evaporation was chosen for the mass production of the BPMs as it gave the best results in terms of homogeneity and defects (like for e.g. burning).

- Replacing the silicon substrate with a less dense material have also the additional benefit of extending the range of application of the new BPMs to lower energy beams.

The devices fabricated to be used in IRRAD are 300 nm Al deposited with evaporation on 25 um Kapton®. Compared with the old BPM devices produced with the standard PCB technology, the new ones are much thinner, ∼300 times less metal and ∼20 times less substrate, and more sensitive (higher SEY) to the beam.

Conclusions and Perspectives

<div style="text-align: right">7</div>

In this thesis, the R&D on the upgrade of the Beam Profile Monitors for IRRAD facility, was presented. After reproducing the microfabricated BPM on Si-SiO$_2$ substrate and proving their concept of working, a study was carried out on the suitability of this substrate and the improvement of their performance. Kapton substrated was selected for the final version and the new devices were evaluated in the laboratory and in the electron beam of the CLEAR facility. Moreover, different thicknesses of sensing material and substrate, deposition methods (with different machines), adhesion techniques, SEY enhancement methods and electrical connection alternatives were evaluated. This chapter presents the evolution of the BPM in recent years and suggests ideas for further improvement.

Performance summary

The evolution of the BPM devices in the last three years is shown in Figure 7.1:

a) The BPM devices used in the IRRAD facility until 2018 with 6 layers of 17 um Cu coated on 120 um Kapton substrate, based on the standard PCB technology;

b) the BPM devices based on the microfabrication technology were few hundreds nm of Al deposited on Si-SiO$_2$ substrate and

c) the last version of the micro-fabricated BPM devices with few hundreds nm of Al deposited on 25 um Kapton substrate.

The first trials to microfabricate BPM devices were already performed in 2018, proving the possibility to use this kind of technology in order to fabricate much thinner BPMs and less invasive, as discussed in Chapter 4. In the context of this thesis and under the EU-funded ATTRACT project, in 2019 the R&D was focused, at first, on single metallic layer deposition on Si-SiO$_2$ substrate[1] in order to master the technique and to look for alternative sensing materials that would enhance the SEY as for example oxides[2]. However, after testing these devices with a 200 MeV electron beam there was a suspicion that Si substrate contributes to the total output signal and from the devices fabricated with Al$_2$O$_3$ coated on top of the Al we could not disentangle if the oxide was enhancing the SEY. For this reason, the R&D was focused

---

[1] It was already evident from the 2018 production that multi-layer devices had the same output signal as single layer devices.

[2] It is known that in vacuum conditions an oxide enhances the secondary electron yield because it "decreases" the work function potential and the e$^-$ can escape easier from the metal
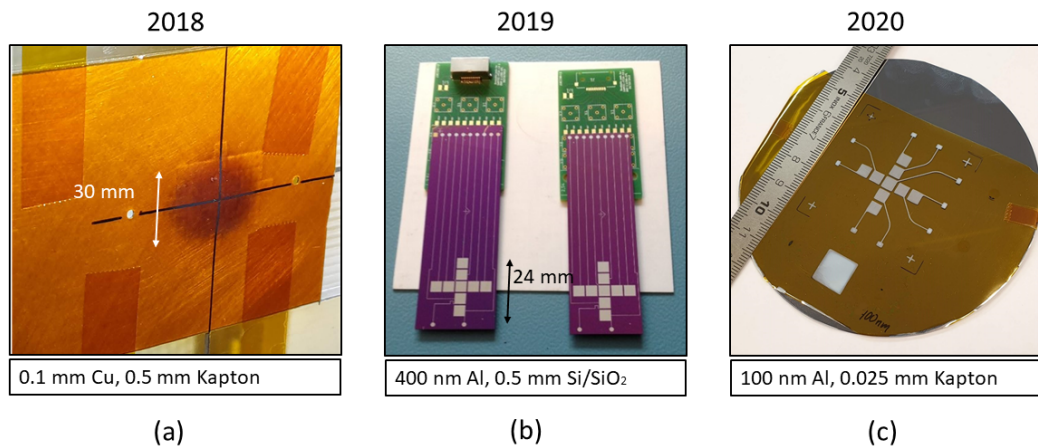
2018	2019	2020
30 mm	24 mm	
0.1 mm Cu, 0.5 mm Kapton	400 nm Al, 0.5 mm Si/SiO₂	100 nm Al, 0.025 mm Kapton
(a)	(b)	(c)

Fig. 7.1.: The evolution of the BPM devices in the last three years: (a) multi-layer BPM ($[15$ um Cu coating on 120 um Kapton$]\times 6$) based on standard PCB technology, (b) single metallic layers of a few hundred nm deposited on Si-SiO$_2$ substrate and (c) single metallic layers of a few hundred nm deposited on Kapton substrate.

later on thin insulating Kapton substrates. Kapton was chosen because of its thermal and chemical stability, its low dielectric constant and high electrical resistivity, its higher radiation tolerance, low thickness and availability. For the fabrication of these devices shadow masks were produced in order to deposit the sensing material with the desired pattern.

Several BPMs were fabricated on Kapton substrates and tested in order to:

- find the best sensing material for SEE in air;
- find the best technique that gives homogeneous deposition across the full patterned surface and at the same time very good adhesion of the metallic layer to the Kapton;
- ensure reliable electrical connection between the BPM and the readout PCB.

After all the tests were performed, aluminum was chosen as sensing material because of its availability, low cost and high SEY. The substrate was treated with oxygen plasma and titanium under vacuum pressure before the metal deposition, in order to improve the adhesion properties between the two materials. E-gun evaporation was chosen as the best coating technique for aluminum deposition on Kapton substrate and the electrical connection was accomplished with conductive glue.

Fig. 7.2 shows the secondary electrons emitted in air as function of primary electrons passing though the central pad for one evaporated and one sputtered sample in comparison with the old multi-layer miniBPM. The evaporated BPM device measure 10% more signal than the devices fabricated with the old technology and no radiation-induced degradation was observed. Table 7.3 summarizes the BPM improvements over the past three years with the key points their transparency ($\sim$27 times less material budget) and sensitivity (higher SEY).
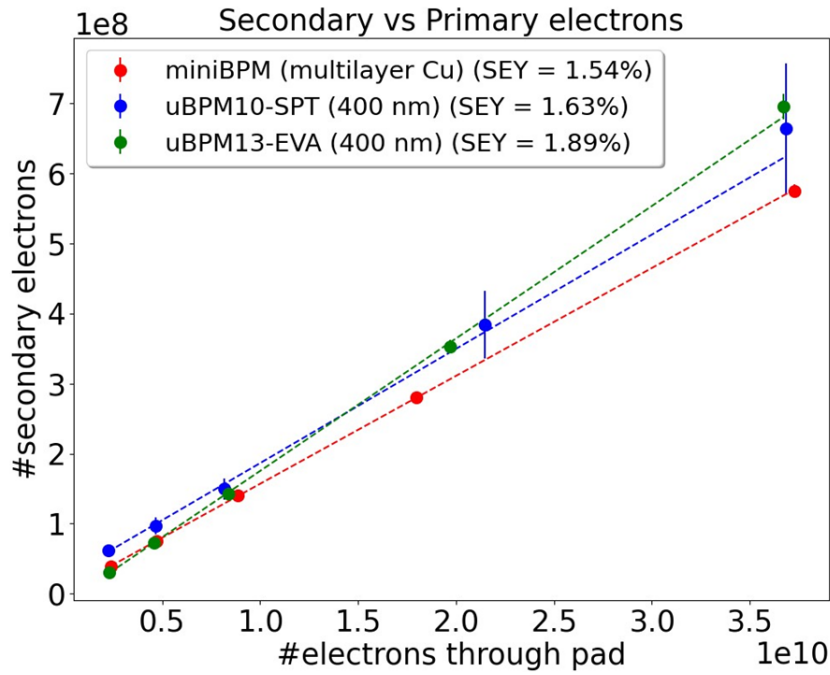
Fig. 7.2.: Primary electrons passing though the central pad as a function of the secondary electrons emitted in air for devices fabricated with sputtering (SPT) and evaporation (EVA), in comparison with the old miniBPM.

These monitors is the final version that will replace the old BPMs in the IRRAD on 2022. Even thinner devices (100 nm) was responding properly to the beam but the thickness of 300 nm was chosen for the massive production, as more reliable.

Parameters	2018	2019	2020
Active material	Cu	sputtered Al	evaporated Al
Active material thickness	100 um	0.4 um	0.3 um
Substrate	FR4	Si/SiO$_2$ wafers	Kapton
Substrate thickness	600 um	525 um	25 um
No of sensing layers	6	2	1
Total material budget in IRRAD	16 mm	15 mm	0.5 mm
δ_{max} by surface analysis	2.18 %	3.45 %	3.53 %
δ_{max} by 200 MeV e$^-$ irradiation	1.54 %	1.63 %	1.89 %
Ratio MeV-on-air/few-hundred-eV-in-vacuum	44 %	46.5 %	54 %
Fraction of radiation length	~26 %	~25 %	< 1 %
Radiation-induced degradation	observed	not observed with electrons	not observed with electrons

Fig. 7.3.: comparison between different generations of BPMs.

This thesis has been completed in the framework of a Technical Studentship at CERN from August 2019 until September 2020 and the work presented is attributed to both personal and collaborative activities. Part of the work performed here, was presented by the author as a poster contribution at the 9th International Beam

Instrumentation Conference (IBIC 2020) and as a public deliverable for the ATTRACT Final Conference:

V. Meskova, O. Sidiropoulou, G. Pezzullo, I. Mateu, F. Ravotti, B. Gkotse, W. Farabolini, A. Gilardi, A. Mapelli. "**A Beam Profile Monitor for high energy proton beams using microfabrication techniques**", IBIC 2020, vol. TUPP37, pp. 86-89. http://accelconf.web.cern.ch/ibic2020/papers/proceed.pdf.

V. Meskova, O. Sidiropoulou, G. Pezzullo, I. Mateu, F. Ravotti, D. Bouvet, J.M. Sallese, B. Gkotse, W. Farabolini, A. Gilardi, A. Mapelli, M. Ritala. "**Ultra high-level radiation monitoring with thin metal nano-layers**". https://attract-eu.com /showroom/project/ultra-high-level-radiation-monitoring-with-thin-me tal-nano-layersnanoradmet/.

Future project vision

The new devices have overall shown to work reliably and feature improved parameters related to their thickness and sensitivity. Nevertheless, there are still space for future development:

- Integration of the sensor to an optimized DAQ system that can be portable (compact/remotely controllable/etc.) and user-friendly, as the existing one is only compatible with the CERN IRRAD infrastructure.

- Validation of radiation hardness of the device in a proton beam. Moreover, validation with lower intensity beams is foreseen since the thickness achieved with the current prototypes promises a large range of working intensities and applications.

- Fabrication of larger scale devices. Today, the overall size of the BPMs is restricted to the 100-mm-diameter wafers.

- Development of a more reliable electrical connection between BPM and readout PCB (e.g. 3D printed electrical connection , wireless connectivity).

- Try other device layouts (e.g. grid of wire, double-side metallised device etc.).

- Try to enhance the sensitivity of the new BPM with an external bias.

The R&D performed in the context of this thesis serves as a starting point for further improvement of BPM devices beyond the usage in IRRAD. Using for example much thinner substrates, the BPM can be used with much lower energy beams (e.g. industry, medicine), as shown in Fig. 7.4.
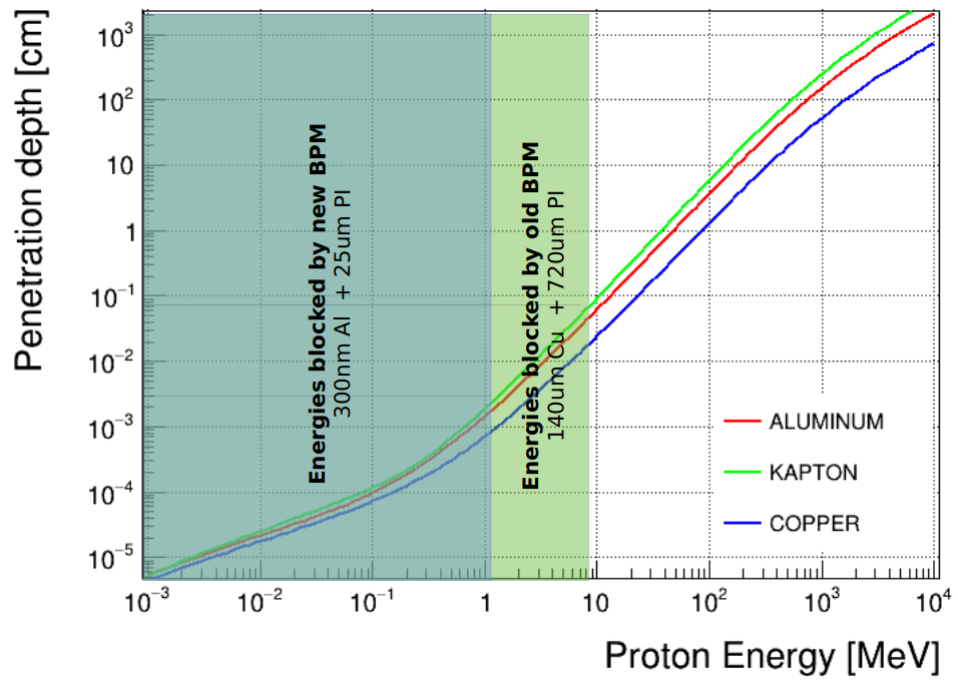
Fig. 7.4.: Extending usage of BPM device beyond IRRAD.

Instruments for beam diagnosis A

The main physics processes that govern the operation of beam diagnostic tools that measure beam intensity and profile can be distinguished in three main categories; particles (secondary photons, electrons or ions emitted from bombarded surfaces) detection, gas ionization and electrodynamics. In this section, the operation of some of the commonly used instruments based on these principles, are discussed. The relevant theory is mostly taken from Ref.[10, 12].

SEM-grid is a detector that perform beam-profile measurements and is based on particle emission. Secondary electrons are liberated from the grid's solid surface under the impact of the incident-beam particles. Thus, a flow of current is produced. The device consists of an array of thin ribbons and measures the transverse density distribution (Fig. A.1(a)). Sequential display of the signals from the ribbons gives the beam profile. When the intercepting material is a foil, the device is called Secondary Emission Chamber and it measures intensities, as was discussed in section 2.2.
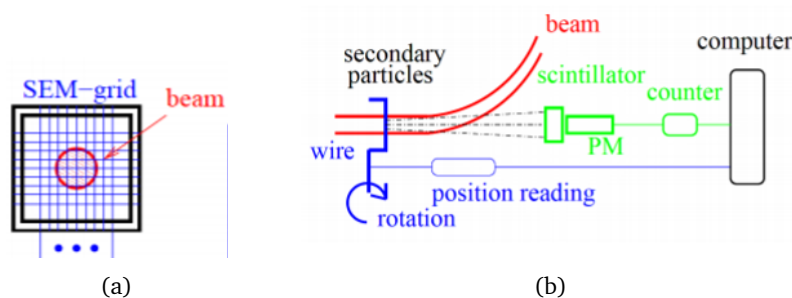

(a)   (b)

Fig. A.1.: Schematics of (a) Secondary Emission Monitors (SEM) grid and (b) wire scanner.

Wire scanner (WS) operates under the same concept like a SEM-grid. A wire is stepped in small increments through the beam. When the incident particles hit the wire, secondary electron emission occurs. For the display of the profile, the position of the wire determined by the position encoder, is plotted on the horizontal axis. The beam signal for the vertical axis is obtained over many pulses by measuring the current given by the emitted secondary electrons. Figure A.1(b) shows the schematics of a WS. This kind of detector is usually applied in proton synchrotrons due to the small amount of intercepting matter.

Scintillation screens are based on the photoelectric effect. The detection starts when the screen is moved into the path of the beam. The screen is inclined at $45°$ to the beam, carries a graticule and is illuminated through a small window in the tank. Through another window, at $90°$ to the beam direction, a CCD camera will see a

2-dimensional image of the beam cross-section. The scintillator generates photons in response to incident radiation. The quantity of photons is proportional to the energy deposited by the ionizing particle (photoelectric effect). Figure A.2(a) shows the schematics of a scintillator screen.
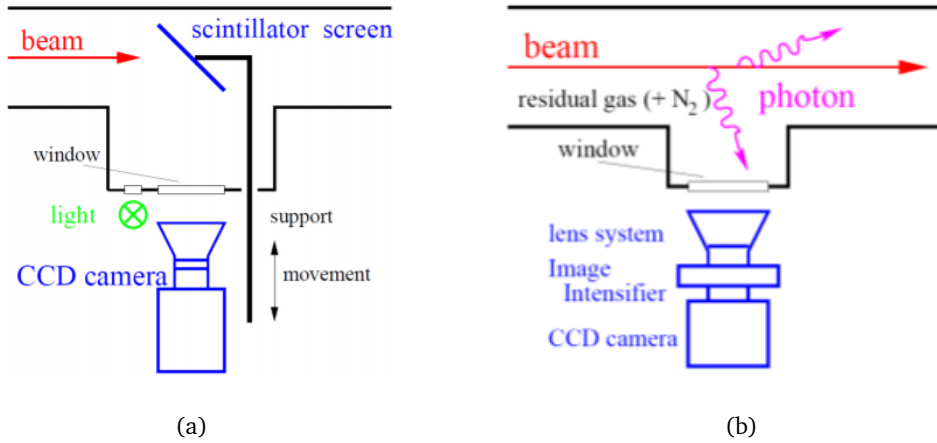

<div align="center">(a)   (b)</div>

Fig. A.2.: Schematics of (a) Scintillator screen and (b) residual fluorescence monitors.

The residual fluorescence monitor is a gaseous detector. The profile of an incident beam can be determined by monitoring the fluorescence emitted by the residual gas molecules using a sensitive image intensifier coupled to a CCD camera. In the setup, the lens system capture the photons and the image intensifier converts the light to electrons. The accumulated charges of the pixels are directly digital-converted at the camera head. Figure A.2(b) shows the schematics of a residual fluorescence monitor.
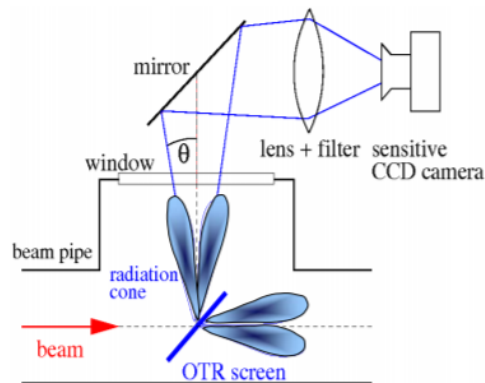

Fig. A.3.: Schematics of optical transition radiation detector.

Another main concept of beam-profile determination tools is based on direct observation of electrodynamics processes inside the monitor. Such detectors are Optical Transition Radiation (OTR) screens and Synchrotron Radiation monitors. OTR is emitted when a fast particle crosses the boundary between two media of different dielectric constant. Figure A.3 shows the schematics of an OTR monitor, where

the emission occurs from the entrance side of a foil. The radiation is distributed into a hollow cone of opening-angle 2θ around the "specular angle", at which the light reflected from the surface of a mirror. An image of the foil is recorded with appropriate optics and a CCD camera.

Synchrotron radiation is emitted when the relativistically moving incident particles are forced to deviate from a predetermined orbit. This is usually done by applying magnet fields with bending magnets. The phenomenon occurs because the rearrangement of the electric filed around the charge causes a perturbation to the radiation outwards. The optical part of the emitted spectrum is observed in most cases by using optical band pass filters and high quality CCD cameras. The schematics of a synchrotron radiation monitor is shown in Figure A.4.
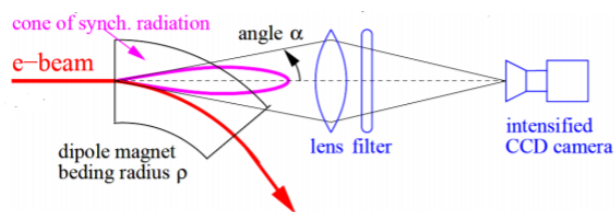
Fig. A.4.: Schematics of synchrotron radiation monitor.

The reliability of the beam diagnosis performed by the monitors describes above can be improved by inserting more than one kind of beam monitor in the passage of the beam. In this way the results of each tool can be cross-checked. To combine the appropriate tools it's important to take into account if their typical operation is related to a transfer line or a circular accelerator.

Readout electronics for BPM B

The signal collected by the sensing pads of the BPM devices is acquired and treated by BPM data acquisition (DAQ) system. This system consists of the readout unit (left in Fig. B.1(a)) which hosts an ADS1115 analog-to-digital converter with precision of 16-bit and an ACF2101 switched integrator from Texas Instruments [49] to amplify the signal. A commercially available Arduino Yún microcontroller board based on the ATmega32u4 handles the whole DAQ process, including the timing synchronization and the background noise measurement. The readout unit is inside the BPM readout box (Fig. B.1(b) bottom).
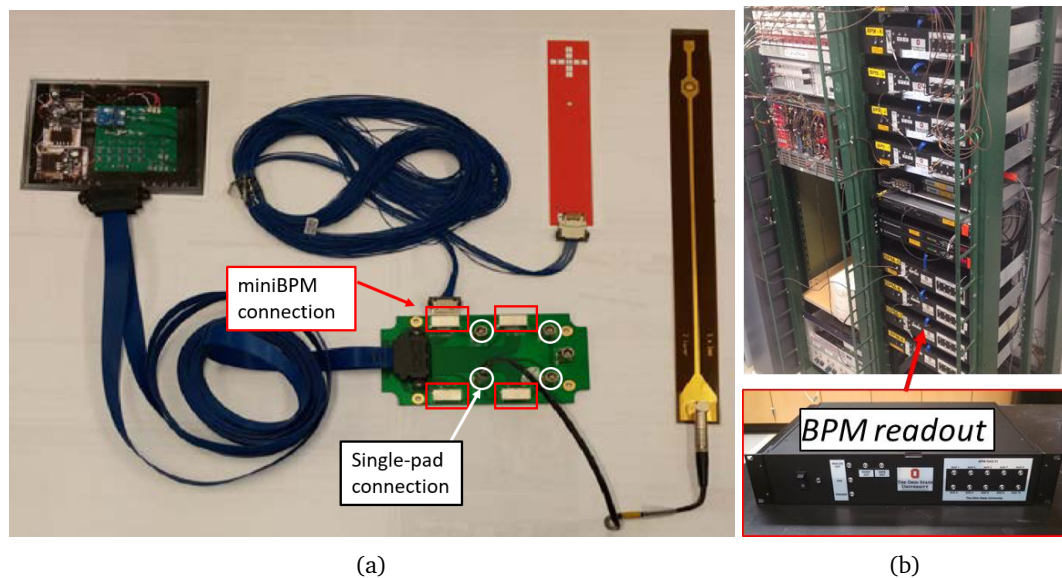

<center>(a)   (b)</center>

Fig. B.1.: (a) Mini and single-pad BPM readout system. Four miniBPMs and four single-pad devices can be connected to one readout unit via a channel-concentrator PCB (bottom of the picture). (b) Rack of BPM data acquisition box located in the IRRAD control room connected to the inside of the IRRAD bunker through shielded 25 m micro-coaxial cables.

There are three types of BPM devices. The fixed-BPMs are directly connected to the readout unit by a shielded, high-speed 40-channel, 50 Ω, 40AVG micro-coaxial cable from Samtec. These cables are 20 m to 35 m long and are located outside the irradiation area. For the connection of miniBPMs and single-pad devices there is a intermediate channel-connector PCB (bottom of Fig. B.1(a)). This 50-channel-connector merge the signals from four miniBPM detectors (each miniPM device uses 9 channels) and four single-pad devices into the unique 40-channel cable [13]. The cables used for this connection are the same as for the fixed-BPMs.

The final data are stored on an online Oracle database ready for visualization [50]. Figure B.1(b) shows a rack of BPM electronics readout located in the IRRAD control room. The connectivity for the microBPM devices is similar to the one used for the miniBPM.

BPM readout electronics performance

Electrical test was performed on BPM readout electronics in order to estimate the minimum output signal that the DAQ system can detect. An Agilent pulse generator[1] and a Keithley power-supply were used during the test.

The resistance used for the test was R=1GΩ. Fig. B.2(a) shows graphically the results of the test. Red dots represent the mean output values with respect to the input voltage values (~30 min each) applied to the system by the pulse generator. The blue dots corresponds to an older test conducted on the same electronics. The output is higher because a voltage divider of a factor of 0.269 was applied on the circuit. Fig. B.2(b) shows a zoom-in into the lower voltage values of Fig. B.2(a) which indicates the lower threshold of the feasible measured output voltage V_{min}=130 mV. The corresponding minimum value in secondary electrons, according to Ref.[21] is:

$$\delta_{min} = \frac{I(output)}{I(input)} = \frac{V(output)/R}{V(input)/R} = \frac{10\ mV}{130\ mV} = 0.076$$

(a)   (b)
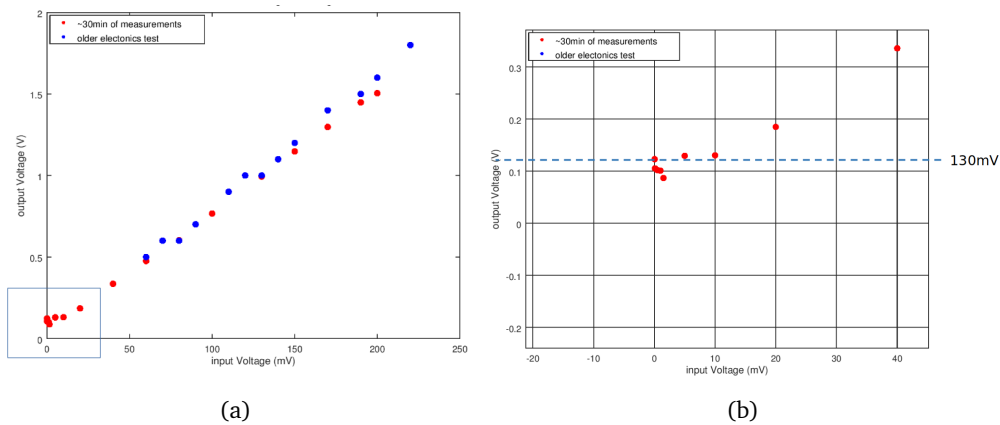
Fig. B.2.: (a) Graphical representation of the BPM-readout electronics test. The output of the older electronics test is higher because there is a voltage divider applied on the circuit. (b) Zoom-in on the lower voltage values.

---

[1]Settings: Period: 10 s, High Level: 2.5 V and Low Level: 0 V, Pulse width: 10 ms, Edge time: 5 ns

Step-by-step process flow outline

The fabrication process of the preliminary microBPMs on Si-SiO$_2$ substrate consists of nine steps, as shown in Fig. C.1. CMi silicon wafers of 100 mm diameter covered with 500 nm SiO$_2$ were used as substrate. The technologies involved in the fabrication are metal sputtering, photolithography, UV exposure and development, metal etching, photoresist stripping and dicing.
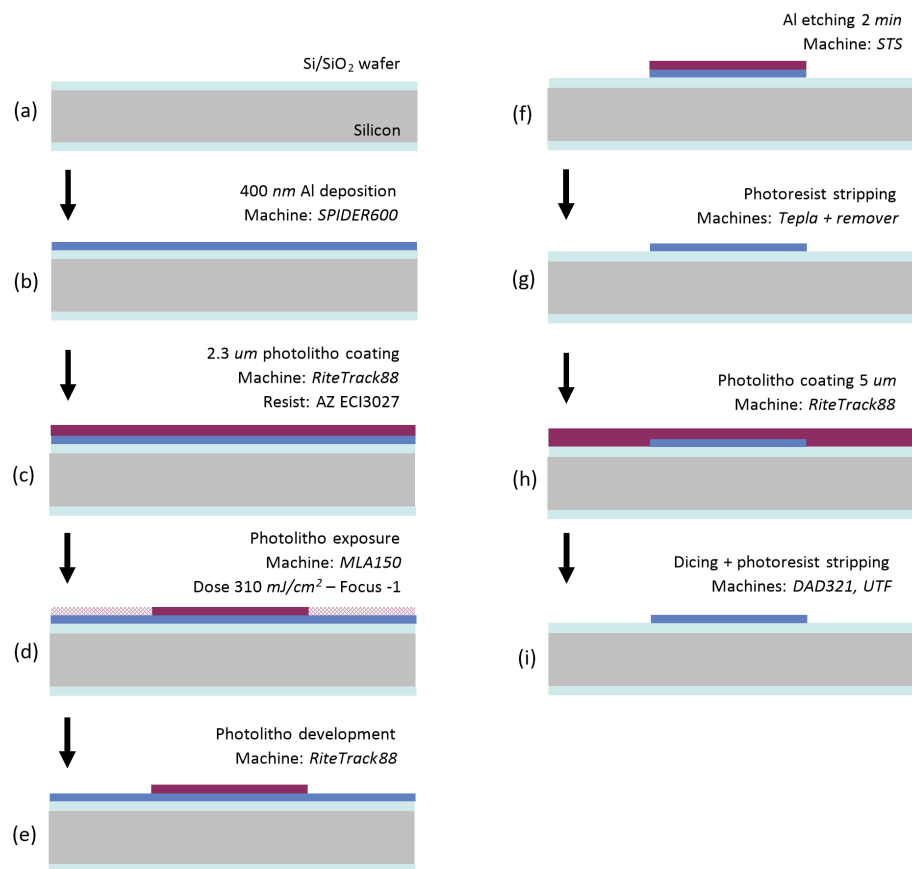

Fig. C.1.: Process flow of the first functional microfabricated BPMs on Si-SiO$_2$ substrate. The tools used for each step in the CMi cleanroom are indicated.

The second production of microBPMs was launched in the attempt to investigate features that influence the BPM signal. The devices were featuring extra oxide layer on top and substrate grounding though a substrate-penetrating pad. Same Si-SiO$_2$ wafers were used and several extra steps were involved to the production, compared to the process flow of the preliminary stage devices, as shown in Fig. C.2.
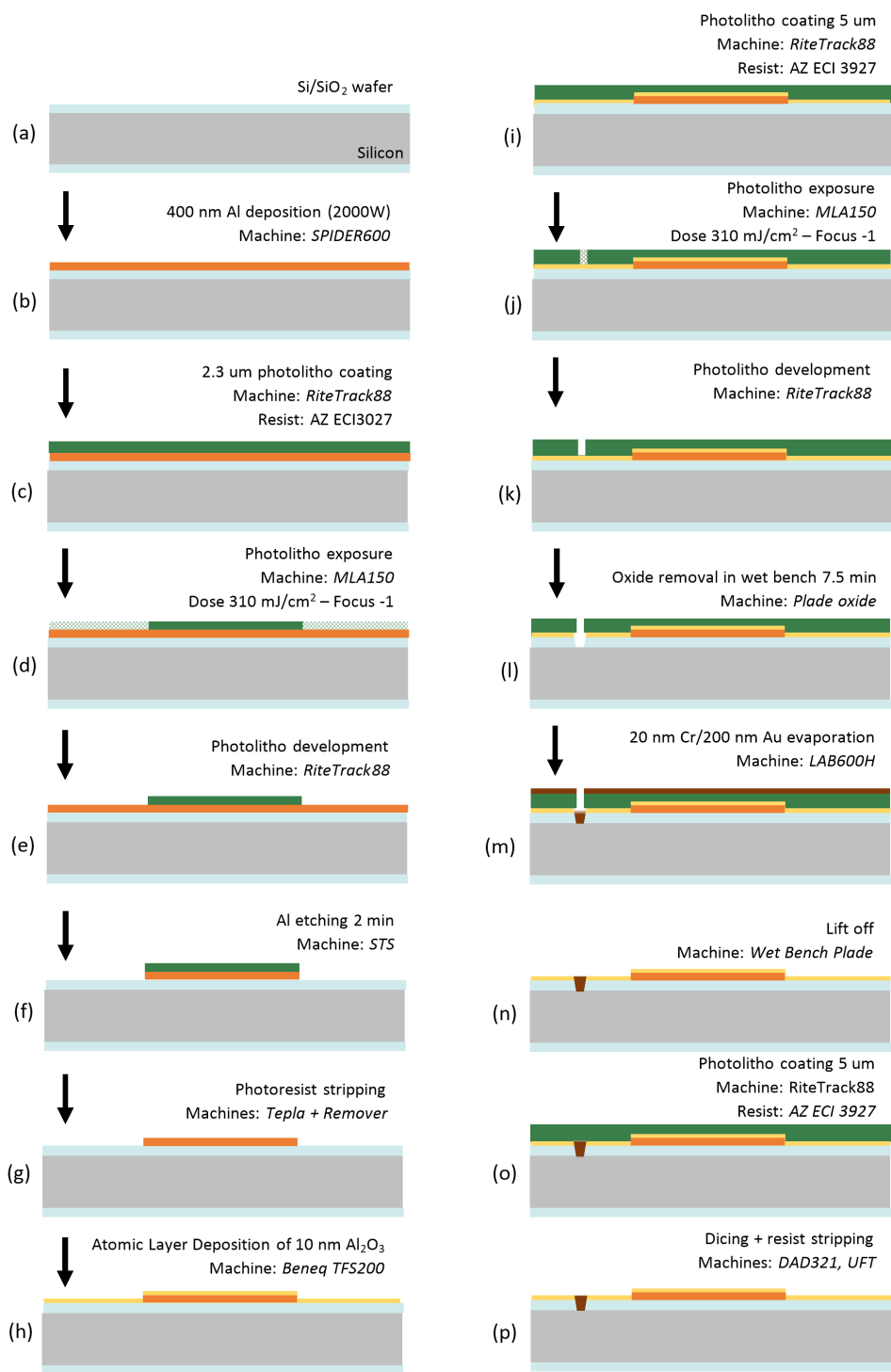
(a) Si/SiO$_2$ wafer — Silicon

(b) 400 nm Al deposition (2000W)
Machine: *SPIDER600*

(c) 2.3 um photolitho coating
Machine: *RiteTrack88*
Resist: AZ ECI3027

(d) Photolitho exposure
Machine: *MLA150*
Dose 310 mJ/cm^2 – Focus -1

(e) Photolitho development
Machine: *RiteTrack88*

(f) Al etching 2 min
Machine: *STS*

(g) Photoresist stripping
Machines: *Tepla + Remover*

(h) Atomic Layer Deposition of 10 nm Al$_2$O$_3$
Machine: *Beneq TFS200*

(i) Photolitho coating 5 um
Machine: *RiteTrack88*
Resist: AZ ECI 3927

(j) Photolitho exposure
Machine: *MLA150*
Dose 310 mJ/cm^2 – Focus -1

(k) Photolitho development
Machine: *RiteTrack88*

(l) Oxide removal in wet bench 7.5 min
Machine: *Plade oxide*

(m) 20 nm Cr/200 nm Au evaporation
Machine: *LAB600H*

(n) Lift off
Machine: *Wet Bench Plade*

(o) Photolitho coating 5 um
Machine: RiteTrack88
Resist: *AZ ECI 3927*

(p) Dicing + resist stripping
Machines: *DAD321, UFT*

Fig. C.2.: Process flow of the second batch of microfabricated BPMs with substrate grounding and extra Al$_2$O$_3$ layer on top. The tools used for each step in the CMi cleanroom are indicated.
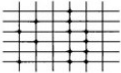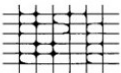
Cross-hatch adhesion test results   D

During the characterization of the new BPMs, cross-hatch adhesion test was performed to determine if aluminum coating can adhere properly to thin Kapton® films. This method uses a grid pattern perpendicular to the surface of the coating to determine the degree of separation from the base material after cutting. Fig. D.1(a) illustrates the steps of the method; (1) Cut lines are made on aluminum as grid with a cross-hatch cutter, (2) adhesive tape is attached to cut lines and (3) the tape is peeled off and both back-side of the tape and cross-cut area are observed. Afterwards, the sample is rated from the highest 5B to the lowest 0B class, according to the classification table shown in Fig. D.1(b).

①Cross-Hatched Cut

②Stick Tape

③Peel Off Tape
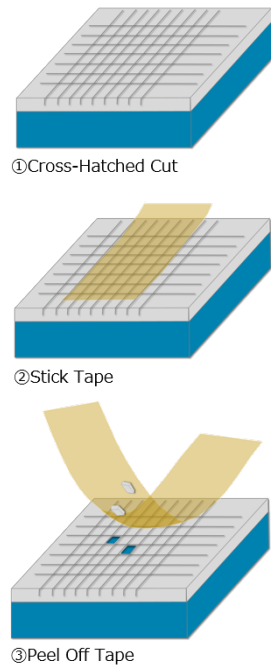
(a)

Classification	Surface of cross-cut areas from which listing has occurred. (Example for six parallel cuts.)	Rate of adhesion
5B	None	The edges of the cuts are completely smooth; none of the squares or the lattice are detached.
4B		Small flakes of coating are detached at intersections; less than 5% of the area is affected.
3B		Small flakes of coating are detached along edges and at intersections of cuts. The area affected is 5 to 15% of the lattice.
2B		The coating has flaked along the edges and at parts of the squares. The affected area is 15 to 35% of the lattice.
1B		The coating has flaked along the edges of cuts in large ribbons and entire squares have detached. The area affected is 35 to 65% of the lattice.
0B	Flaking and detachment in excess of 65%.	

(b)

Fig. D.1.: (a) Steps of the cross-hatch adhesion test and (b) adhesion evaluation table.

The results from the adhesion test performed on 180 um and 50 um Kapton sputtered with aluminum by five different deposition recipes are shown in Fig. D.2. Fig. D.3 shows the results from the 25 um sputtered Kapton while Fig. D.4 shows an 25 um Kapton coated by evaporation. The best adhesion is observed for the thinnest substrate independently of the coating method.
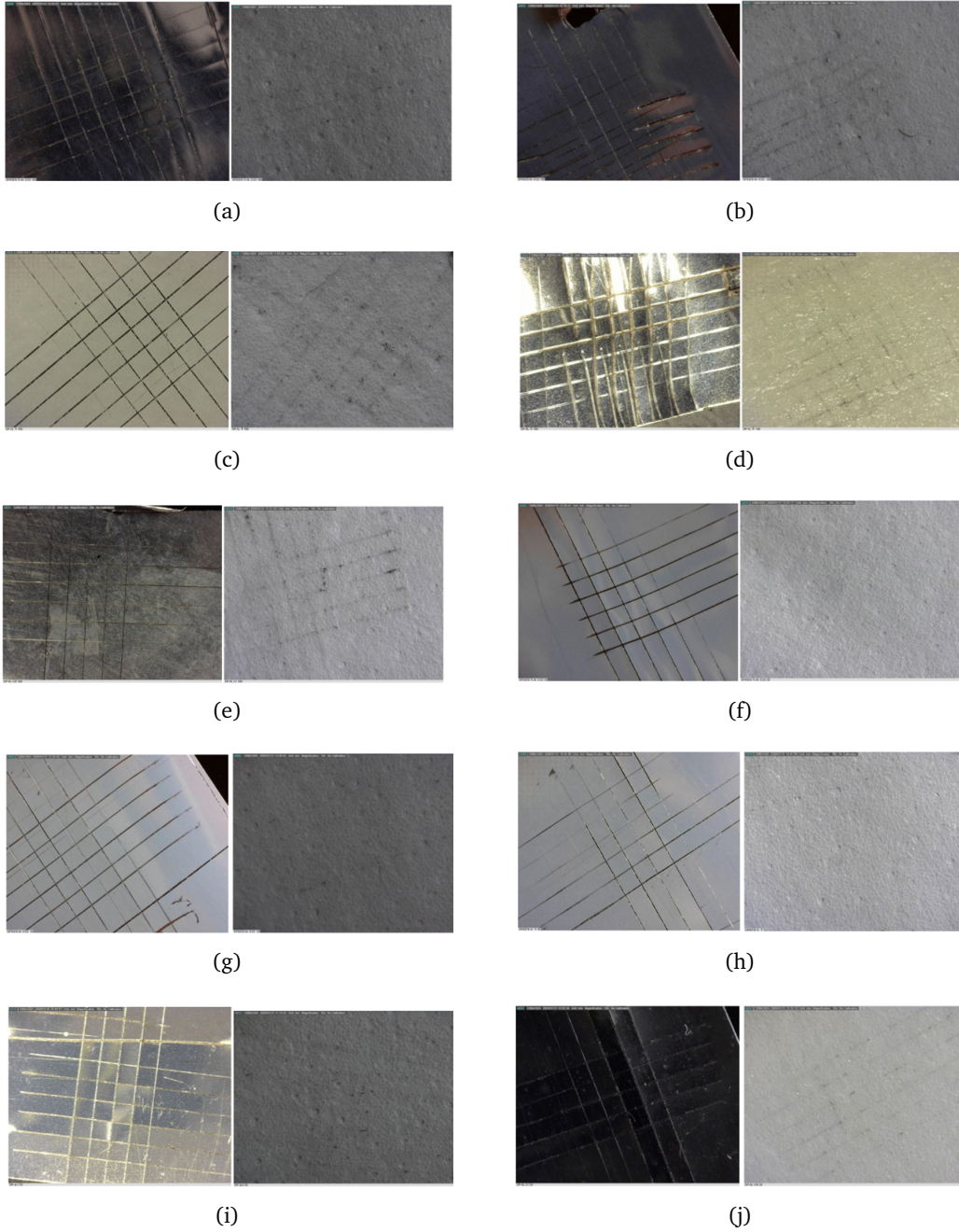
Fig. D.2.: Deposition on 180 um Kapton substrate with recipes: (a) Ti/EO$_2$/Al (SPIDER600), (b) EO$_2$/Al (SPIDER600), (c) Ti/Al (SPIDER600), (d) Ti/Al (DB650), (e) Cr/Al (DB650).
Deposition on 50 um Kapton substrate with recipes: (f) Ti/EO$_2$/Al (SPIDER600), (g) EO$_2$/Al with SPIDER600 (h) Ti/Al with SPIDER600, (i) Ti/Al with DB650, (j) Cr/Al with DB650.

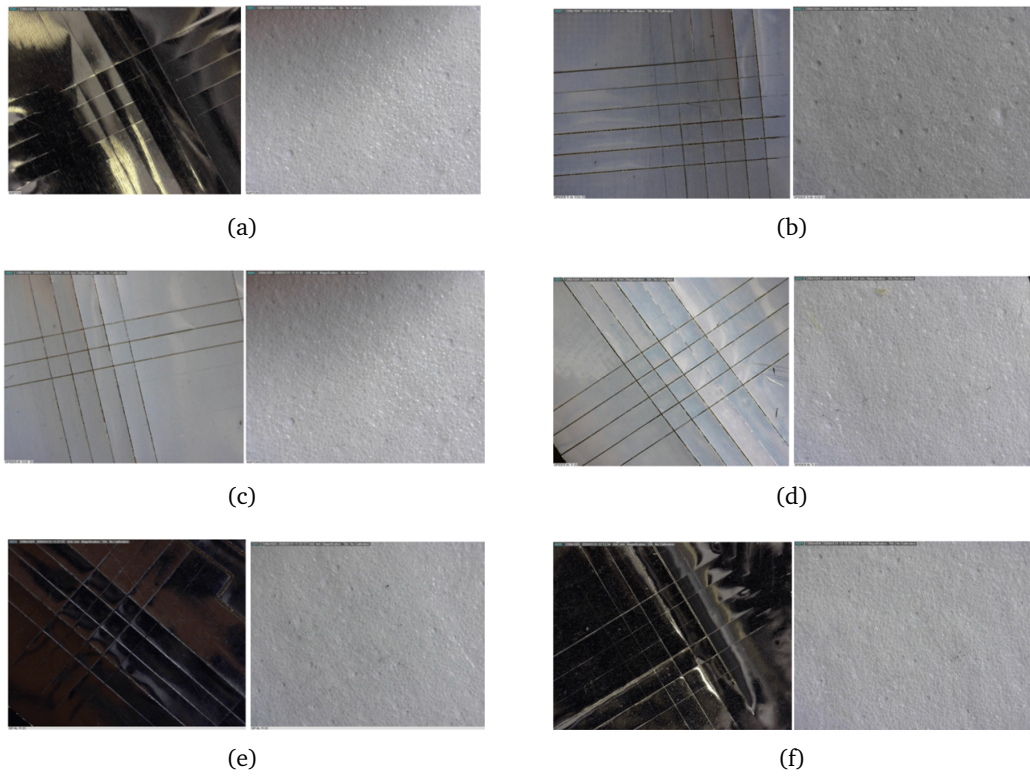**Fig. D.3.:** (a) Commercial Kapton 25.4 um and Al 100 nm. Deposition on 25 um Kapton substrate with recipes: (b) Ti/EO$_2$/Al with SPIDER6000, (c) EO$_2$/Al with SPIDER600, (d) Ti/Al with SPIDER600, (e) Ti/Al with DB650, (f) Cr/Al with DB650

Fig. D.4.: 300 nm Al evaporated on 25 um Kapton. (a) After making the pattern with the crosshatch cutter and (b) back side of the peeled tape.

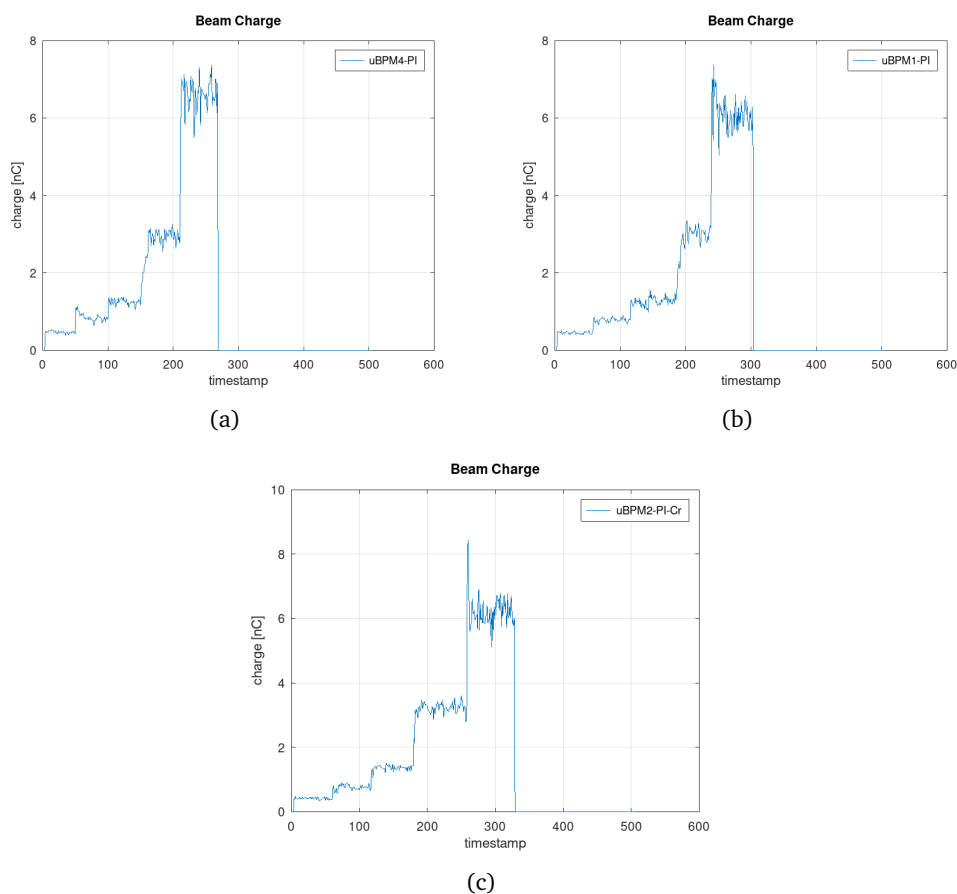# Beam conditions during the experimental runs in the CLEAR

Fig. E.1.: Beam conditions: charge (nC) as a function of timestamp for the test in THz (a) uBPM4-PI (100 nm Al on 25um Kapton® - Commercial tape), (b) uBPM1-PI (400nm Al SPT on 25um Kapton® - EPFL CMi) and (c)uBPM2-PI-Cr (10nm Cr on 50um Kapton® - CERN MPT Workshop)

Fig. E.2.: Beam conditions: charge (nC) as a function of timestamp for the test in THz (a) uBPM5-PI (400 nm Al + 10 nm Al_2O_3 on 25um Kapton®), (b) uBPM6-PI (300 nm Al + 10 nm Al_2O_3 on 25um Kapton®) and (c) uBPM7-PI (300 nm Al on 25um Kapton®)

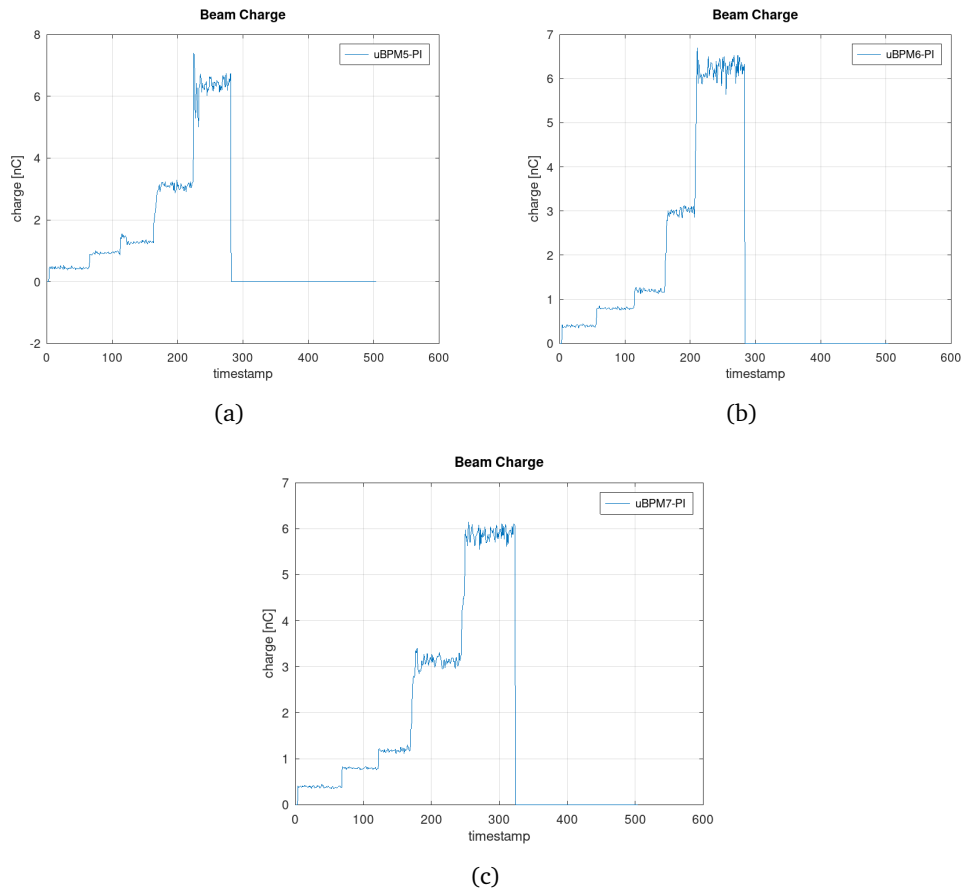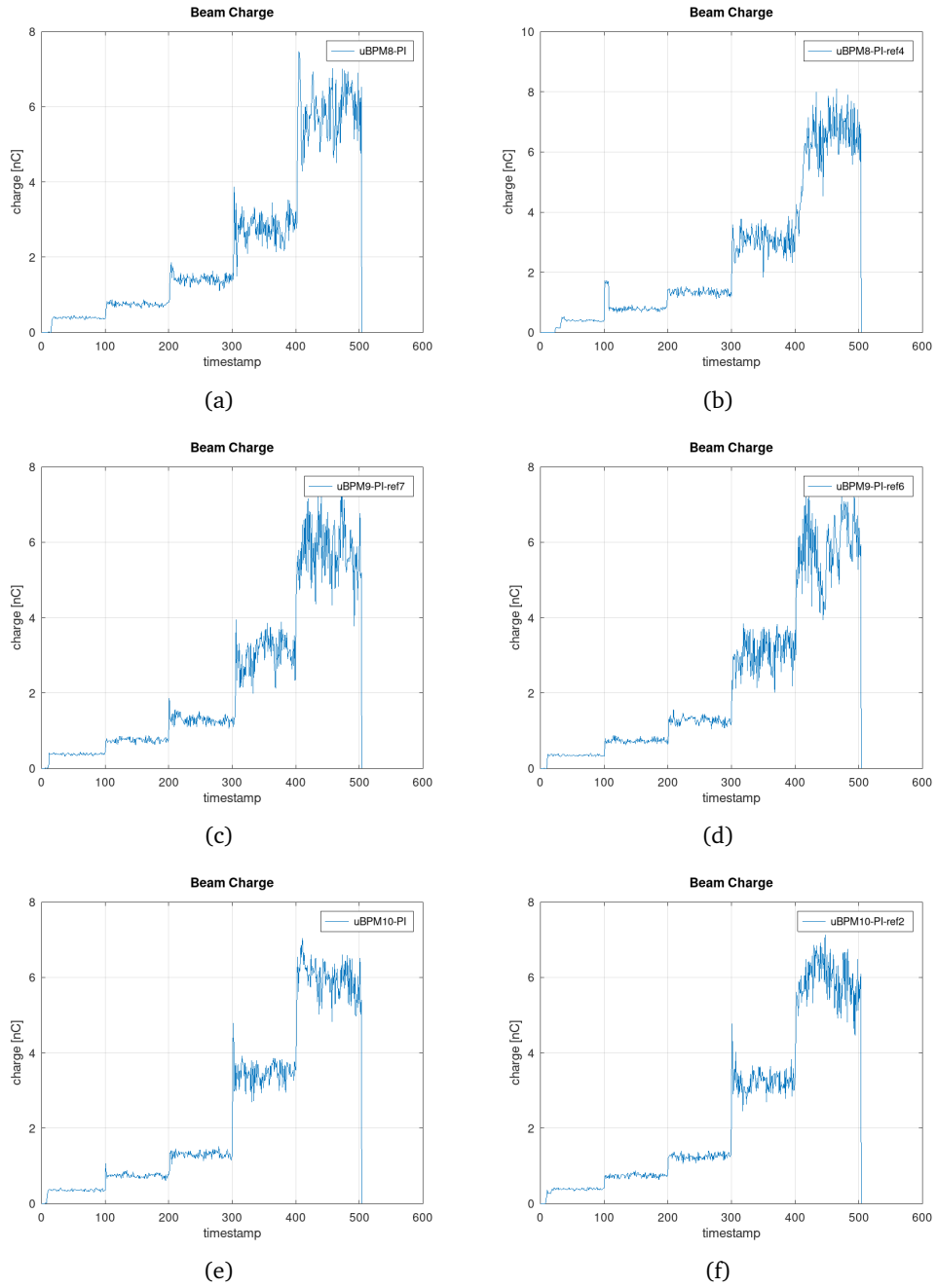**Fig. E.3.:** Beam conditions: charge (nC) as a function of timestamp for the test in THz (a) uBPM8-PI (100 nm Al on 25um Kapton®), (b) uBPM8-PI-ref4 (100 nm Al + 10 nm Al_2O_3 on 25um Kapton®), (c) uBPM9-PI-ref7 (300 nm Al on 25um Kapton®) (d) uBPM8-PI-ref6 (300 nm Al + 10 nm Al_2O_3 on 25um Kapton®), (e) uBPM10-PI (400 nm Al on 25um Kapton®) (f) uBPM10-PI-ref2 (10 nm CR + 5 um Cu on 50um Kapton®)

Abbreviations

AIDA	Advanced European Infrastructures for Detectors and Accelerators
ALD	Atomic Layer Deposition
ALICE	A Large Ion Collider Experiment
ATLAS	A Toroidal LHC Apparatus Detector
BPM	Beam Profile Monitor
BSE	Back Scattered Electrons
CCC	CERN Control Center
CCD	Charge-Coupled Device
CERN	The European Organization for Nuclear Research
CHARM	Mixed-field Irradiation Facility in CERN
CLEAR	CERN Linear Electron Accelerator for Research
CMi	Center of Micronanotechnology at EPFL
CMS	Compact Muon Solenoid
DAQ	Data Acquisition System
DUTH	Democritus University of Thrace
EN	Engineering Department
EPFL	École Polytechnique Fédérale De Lausanne
EVA	Evaporation
FIB	Focused Ion Beam
FR4	Flame Retardant (4 indicates woven glass reinforced epoxy resin)
HEP	High Energy Physics
IRRAD	Proton Irradiation Facility at CERN
LEIR	Low Energy Ion Rin
LHC	Large Hadron Collide
LHCb	Large Hadron Collider beauty experiment
MWPC	Multi-Wire Proportional Chamber
OTR	Optical Transition Radiation
PCB	Printed Circuit Board
PI	Polyimide
POT	Protons On Target
PS	Proton Synchrotron
PSB	Proton Synchrotron Booster
PVD	Physical Vapor Deposition
SE	Secondary Electron

SEE	Secondary Electron Emission
SEC	Secondary Emission Chamber
SEM	Scanning Electron Microscope
SEY	Secondary Emission Yield
SPS	Super Proton Synchrotron
SPT	Sputtering
THz	Tera Hertz source
uBPM	micro Beam Profile Monitor
UV	Ultra Violent
VESPER	Very energetic Electron facility for Space Planetary Exploration missions in harsh Radiative environments
WS	Wire Scanner
XION	Ionization Chamber
YAG	Yttrium Aluminum Garnet

Bibliography

[1] L. Evans and P. Bryant, "LHC machine," *Journal of Instrumentation*, vol. 3, no. 08, p. S08001, 2008. [Online]. Available: http://dx.doi.org/10.1088/1748-02 21/3/08/S08001

[2] ALICE Collaboration, "The ALICE experiment at the CERN LHC," *Journal of Instrumentation, vol. 3, no. 08, p. S08002,* 2008. [Online]. Available: http://dx.doi.org/10.1088/1748-0221/3/08/S08002

[3] ATLAS Collaboration, "The ATLAS Experiment at the CERN LHC," *Journal of Instrumentation, vol. 3, no. 08, p. S08003*, 2008. [Online]. Available: http://dx.doi.org/10.1088/1748-0221/3/08/S08003

[4] CMS Collaboration, "The CMS experiment at the CERN LHC," *Journal of Instrumentation,vol. 3, no. 08, p. S08004*, 2008. [Online]. Available: http://dx.doi.org/10.1088/1748-0221/3/08/S08004

[5] LHCb Collaboration, "The LHCb Detector at the LHC," *Journal of Instrumentation,vol. 3, no. 08, p. S08005*, 2008. [Online]. Available: http://dx.doi.org/10.1088/1748-0221/3/08/S08005

[6] "Cern complex." [Online]. Available: https://home.cern/science/accelerators /accelerator-complex

[7] B. Gkotse, M. Glaser, M. Moll, F. Ravotti, "IRRAD: The new 24GeV/c proton irradiation facility at CERN," *12th International Topical Meeting on Nuclear Applications of Accelerators, Washington, DC, USA, pp.182-187*, 2015.

[8] "CERN Linear Electron Accelerator for Research." [Online]. Available: https://clear.cern/clear

[9] A. Curcio et al, "Beam-based sub-THz source at the CERN linac electron accelerator for research facility," *Physical Review Accelerators and Beams 22, 020402*, 2019. [Online]. Available: https://journals.aps.org/prab/pdf/10.110 3/PhysRevAccelBeams.22.020402

[10] P. Fork, "Lecture Notes on Beam Instrumentation and Diagnostics, Joint University Accelerator School," 2011. [Online]. Available: https://indico.cern.ch/event/569714/contributions/2303731/attachments/1415057/2166101/juas_script.pdf

[11] V. Agoritsas, "Secondary Emission Chambers for monitoring the CPS ejected beams," *Daresbury Symposium on Beam Intensity Measurement*, 1968.

[12] P. Strehl, "Beam Instrumentation and Diagnostics," 2006. [Online]. Available: https://www.springer.com

[13] F. Ravotti, B. Gkotse, M. Glaser, E. Matli, G. Pezzullo, "The Beam Profile Monitoring System for the CERN IRRAD Proton Facility," *Proceedings of IBIC2016, Barcelona, Spain*, 2016. [Online]. Available: http://accelconf.web.cern.ch/ibic2016/papers/wepg75.pdf

[14] P. Forck, A. Bank, "Residual Gas Fluorescence for Profile Measurements at the GSI UNILAC ," *EPAC 2002, Paris, France* . [Online]. Available: https://accelconf.web.cern.ch/e02/PAPERS/THPRI056.pdf

[15] K. Renuka, "Scintillation Screen Materials for Beam Profile Measurements of High Energy Ion Beams." [Online]. Available: http://tuprints.ulb.tu-darmstadt.de/5504/1/Dissertation.pdf

[16] E. B. Holzer, "Beam instrumentation and diagnostics." [Online]. Available: https://indico.cern.ch/event/532397/contributions/2170753/attachments/1349278/2061096/CAS_2016_Instrumentation.pdf

[17] "CERN High energy AcceleRator Mixed field facility." [Online]. Available: https://kt.cern/technologies/charm

[18] O. Sidiropoulou, "Characterization of the ATLAS-type Micromegas Detectors," *CERN-THESIS-2018-140*. [Online]. Available: https://cds.cern.ch/record/2636918

[19] H. Koziol, "Beam diagnostics for accelerators." [Online]. Available: https://www.isa.au.dk/accfys/E08/Download/Koziol_BeamDiagnostics.pdf

[20] "Cern Control Center (CCC)." [Online]. Available: https://visit.cern/ccc

[21] Raquel Maria Amaro Vaz, "Studies of the secondary electron from diamond films (2008)." [Online]. Available: http://www.chm.bris.ac.uk/pt/diamond/raquelthesis/Raquel-Vaz-PhD-thesis.pdf

[22] A. Navarro Fernandez, " Characterization and optimization of CERN Secondary Emission Monitors (SEM) used for beam diagnostics." [Online]. Available: https://upcommons.upc.edu/handle/2117/105996

[23] Shu Xia Tao, Chan HW, H. Graaf, " Secondary Electron Emission Materials for Transmission Dynodes in Novel Photomultipliers: A Review," *Materials 9(12)*, 2016. [Online]. Available: https://doi.org/10.3390/ma9121017

[24] M. J. Berger et al., "ESTAR, PSTAR, and ASTAR: Computer Programs for Calculating Stopping-Power and Range Tables for Electrons, Protons, and Helium Ions (version 1.2.3)." [Online]. Available: http://physics.nist.gov/Star

[25] L. Austin, H. Stark, "Annalen der Physik 314.10, 271-292," 1092.

[26] H. Seiler, "Secondary electron emission in the scanning electron microscope," *Journal of Applied Physics 54, R1*, 1983. [Online]. Available: https://doi.org/10.1063/1.332840

[27] A. Perrot, "A luminosity monitor for LHC," *47th IEEE Nuclear Science Symposium and Medical Imaging Conference, Lyon, France, pp.5/115-18 (v.1)*, 2000. [Online]. Available: 10.1109/NSSMIC.2000.949096

[28] R. C. Alig, S. Bloom, "Electron-Hole-Pair Creation Energies in Semiconductors," *Physical Review Letter, 35, 1522*, 1975. [Online]. Available: https://doi.org/10.1103/PhysRevLett.35.1522

[29] Y. Lin, D. Joy, "A new examination of secondary electron yield data," *Surf. Interface Anal.2005;37: 895 – 900*. [Online]. Available: https://doi.org/10.1002/sia.2107

[30] G. L. Robert, A. J. Dekker, "Theory of Secondary Emission," *Phys. Rev. 107, 977*, 1957. [Online]. Available: https://doi.org/10.1103/PhysRev.107.977

[31] N. Hilleret, M. Taborelli, "The secondary electron yield of technical materials and its variation with surface treatments," *Proceedings of 7th EPAC 2000, Vienna, Vol. 1-3, pp. 217-221*, 2000.

[32] M. I. Patino, "Angular, temperature, and impurity effects on secondary electron emission from Ni(110)," *J. Appl. Phys. 124, 093301*, 2018. [Online]. Available: https://doi.org/10.1063/1.5025344

[33] Blankenburg, "Secondary Emission from thin metal foils bombarded with 70 MeV electrons," 1965.

[34] L. Jiangtao, "Identification of multilayer structures using secondary electron yield curves: effect of native oxide films on EUV-patterned mask inspection," *Proceedings Vol. 9778, Metrology, Inspection, and Process Control for Microlithography XXX; 977817*, 2016. [Online]. Available: https://doi.org/10.1117/12.2218944

[35] L. Malter, "Thin Film Field Emission," *Phys. Rev. 50, 48*, 1936. [Online]. Available: https://doi.org/10.1103/PhysRev.50.48

[36] H. Bruining, "The depth at which secondary electrons are liberated," *Physica, Vol. 3, Issue 9, pg. 1046-1052*, 1936. [Online]. Available: https://doi.org/10.1016/S0031-8914(36)80330-9

[37] "AIDA 2020." [Online]. Available: http://aida2020.web.cern.ch/

[38] J. Bronuzzi et al, "Beam profile monitor devices using microfabricated metal thin-films." [Online]. Available: https://cds.cern.ch/record/2655341/files/AIDA-2020-NOTE-2019-003.pdf

[39] A. K. Singh et al, "The influence of insulating substrate on the electrical measurements of focused ion beam fabricated electrodes with nano-gap spacing," *Nuclear Instruments and Methods in Physics Research Section B: Beam Interactions with Materials and Atoms, Vol. 268, Issue 19, pg. 3282-3286*, 2010. [Online]. Available: https://doi.org/10.1016/j.nimb.2010.06.016

[40] M. Ramos et al, "Aluminium/Polyimide adhesion," *Acta Metallurgica et Materialia, Vol. 41, Issue 7, pg. 2105-2111*, 1993.

[41] M. Tavlet, A. Fontaine, H. Schönbacher, "Compilation of radiation damage test data." [Online]. Available: https://cds.cern.ch/record/357576

[42] A. Baptista et al, "On the Physical Vapour Deposition (PVD): Evolution of Magnetron Sputtering Processes for Industrial Applications," *Procedia Manufacturing 17 pg. 746–757*, 2018.

[43] L. Jiangtao, "Secondary electron emission influenced by oxidation on the aluminum surface: the roles of the chemisorbed oxygen and the oxide layer," *Plasma Sources Science and Technology, 27, 044002*, 2018.

[44] "SPIDER600 system." [Online]. Available: https://www.epfl.ch/research/facilities/cmi/equipment/thin-films/pfeiffer-spider-600/

[45] "DP650 system." [Online]. Available: https://www.epfl.ch/research/facilities/cmi/equipment/thin-films/alliance-concept-dp-650/

[46] "EVA760 system." [Online]. Available: https://www.epfl.ch/research/facilities/cmi/equipment/thin-films/alliance-concept-eva-760/

[47] "Dupont Kapton HN." [Online]. Available: https://docs.rs-online.com/c6e2/0900766b80659d8c.pdf

[48] A. Korsunsky, "Residual stress evaluation at the micrometer scale: Analysis of the thin coating by FIB milling and digital image correlation," *Surface Coatings Technology, 205, 2393-2403*, 2010.

[49] "ACF2101 Low Noise, Dual SWITCHED INTEGRATOR [Online]." [Online]. Available: http://www.ti.com/lit/ds/symlink/acf2101.pdf

[50] B. Gkotse, M. Glaser, E. Matli, F. Ravotti, "System architecture and data processing capabilities of the Beam Profile Monitor for the CERN IRRAD Facility," *IEEE Nucl. Sci. Symp. Conf., pp. 1–4, 2016*.